Non-equilibrium assembly and phase behavior of colloidal particles in active liquids

विद्या वाचस्पति की
उपाधि की अपेक्षाओं की आंशिक पूर्ति में प्रस्तुत शोध प्रबंध

A thesis submitted in partial fulfillment of the requirements for the
degree of Doctor of Philosophy

द्वारा /by:

प्रज्ञा कुशवाहा /**Pragya Kushwaha**

पंजीकरण सं. /Registration ID: 20183623

शोध प्रबंध पर्यवेक्षक /Thesis Supervisor:
Dr. Vijayakumar Chikkadi

भारतीय विज्ञान शिक्षा एवं अनुसंधान संस्थान पुणे

INDIAN INSTITUTE OF SCIENCE EDUCATION AND RESEARCH PUNE

2024

This thesis is dedicated to my parents, for their unwavering support and endless encouragement, and to my husband, for his love, patience, and understanding throughout this journey.

Certificate

I certify that the work incorporated in the thesis entitled **“Non-equilibrium assembly and phase behavior of colloidal particles in active liquids”** submitted by **Pragya kushwaha** was carried out by the candidate, under my supervision. The work presented here or any part of it has not been included in any other thesis submitted previously for the award of any degree or diploma from any other University or institution.

(Supervisor)
Dr. Vijayakumar Chikkadi
Date : November 14, 2024

Declaration by Student

Name of Student: Pragya kushwaha

Reg. No.: 20183623

Thesis Supervisor(s): Dr. Vijayakumar Chikkadi

Department: Physics

Date of joining program: 01/08/2018

Date of Pre-Synopsis Seminar : 12/06/2024

Title of Thesis : Non-equilibrium assembly and phase behavior of colloidal particles in active liquids

I declare that this written submission represents my idea in my own words and where others' ideas have been included; I have adequately cited and referenced the original sources. I declare that I have acknowledged collaborative work and discussions wherever such work has been included. I also declare that I have adhered to all principles of academic honesty and integrity and have not misrepresented or fabricated or falsified any idea/data/fact/source in my submission. I understand that violation of the above will be cause for disciplinary action by the Institute and can also evoke penal action from the sources which have thus not been properly cited or from whom proper permission has not been taken when needed.

The work reported in this thesis is the original work done by me under the guidance of Dr. Vijayakumar Chikkadi.

Signature of the student

Pragya kushwaha

Date : November 14, 2024

Acknowledgments

I am deeply grateful to my advisor, Dr. Vijayakumar Chikkadi, for his incessant guidance and the facilities that allowed me to explore various experimental possibilities. His collaborative approach fostered meaningful discussions and deeper understanding, particularly through interactions with field experts.

I extend my sincere thanks to my previous Research Advisory Committee (RAC) member, Prof. Rajarshi Chakrabarti (IIT Bombay), and my current RAC members, Prof. Shivprasad Patil (IISER Pune) and Dr. Raghunath Chelakkot (IIT Bombay), for their constructive feedback and insightful suggestions, which significantly enriched my research.

I was fortunate to collaborate with Dr. Shraddha Mishra, Dr. Raghunath Chelakkot, Prof. Dibyendu Das, and Prof. Sanjay Puri. Their contributions were invaluable. I am also grateful to Prof. Deepak Dhar, Prof. Madan Rao, Dr. Rajesh Singh, Prof. Ganesh Subramanian, Prof. Mustansir Barma, and Dr. Kabeer Ramola for engaging discussions that helped me better understand our system.

I would like to thank Prof. Suneesh Radhakrishnan for teaching me the basics of bacterial culturing, handling, and allowing me to use their cold storage. I also appreciate Prof. Chaitanya Athale for his suggestions, Prof. Thomas Pucadyil for facilitating my learning of the PEG coating process through his lab members and Dr. Tapomay Bhattacharya for providing GFP-tagged bacteria and managing them. I am thankful to Prof. Umakant Rapol and his students for giving me hands-on experience with optical tweezers in the early days of my Ph.D. I am also grateful to the chair of the Bio department for granting me access to the UG bio lab for my bacteria-related experiments and to the technical assistants - Nilesh, Kartik, Sudheer, Anil, and Shabnam - for their help in resolving various technical issues. I am also thankful to Prabhakar and Dhanashree for their academic support, and to Ramji and Daji for their housekeeping services.

I would like to acknowledge the financial support from UGC-CSIR and SERB (JRF), which made this research possible.

A special note of thanks to my best friend and lab mate, Rati, for her kindness and friendship throughout this journey. I also appreciate the assistance and valuable discussion with Sayan, and to Rahul for helping with the tracking of dens baterial system, and to Manish with whom I enjoyed going for evening tea break. I would like to extend my appreciation to other former lab member including Anjaly, Shantanu, Gourav, Sagar, Rhudwik, Kartika, Ashish, Atharva, Abhishek, Abhinav, Anushree and others.

I am grateful to my friends at IISER - Abhishek Anand, Keerti, Netra, Anrab, Pranab, Shivsagar and Harinee - whose presence during my stay means lot to me. The home-cooked meals shared with Rati and Anjali were a source of comfort and sustenance, helping me endure those challenging days. I will always cherish the delicious Odia food and the many other meals we prepared and enjoyed together.

My spiritual growth over the years has been guided by Satgura Mata Sudiksha ji Maharaj and Rajpita Ramit Chandana ji, to whom I am deeply grateful. The congregation of like-minded saints at Santang Bhavan in Kalewadi, where I sought peace and strength every Sunday, has been a source of immense motivation, reminding me to trust in the process and believe that everything happens for the best.

Finally, my heartfelt appreciation goes to my family. To my parents, thank you for your unconditional love, support, and faith in me. To my siblings, Prabha, Shradhha, and Akash, your encouragement and humor have been a constant source of strength. To my nephew Prabhas, thank you for being such a sweet and lovable presence in my life. I also deeply appreciate my in-laws for their care, support and love.

Lastly, I owe everything to my husband, Somesh Chandra. His love, patience, and endless encouragement have been my anchors during the most challenging times. This thesis is as much his as it is mine.

Date: November 14, 2024 (Pragya kushwaha)

”Somewhere, something incredible is waiting to be known.”

– Carl Sagan

”Do not go where the path may lead, go instead where there is no path and leave a trail.”

– Ralph Waldo Emerson

”The more I read, the more I acquire, the more certain I am that I know nothing.”

– Voltaire

Abstract

The thesis explores the complex interactions and phase behavior of colloidal particles in active liquids, focusing particularly on systems where large, non-Brownian colloids are dispersed in suspensions of Escherichia coli. The non-equilibrium assembly of colloids has recently gained significant attention due to its potential to create novel structures with properties unattainable in equilibrium systems.

Our research combines both experimental and numerical approaches to explore the dynamic clustering phenomena that arise from the interplay between the activity of the system and the effective attractive potential among colloids. The strength of this effective potential can be tuned by varying the size ratio of passive to active particles. A larger size ratio results in stronger effective interactions, which in turn leads to the formation of larger clusters of passive particles. Simulations also show that at sufficiently large size ratios, macroscopic phase separation can occur.

Further investigation into the phase separation of colloids reveals novel coarsening features. Similar to a binary mixture in equilibrium systems undergoing phase separation via spinodal decomposition, our system exhibits a spinodal-like route to phase separation. A homogeneous mixture of colloids and swimmers is unstable, leading the colloidal particles to form clusters that grow in size over time. The spatial correlations of a suitable scalar order parameter exhibit dynamic scaling, similar to equilibrium systems. However, the length scale of the clusters grows as $L(t) \sim t^{1/4}$ over the experimental time scales, suggesting slower growth than predicted by the Lifshitz-Slyozov law. The nature of the interfaces and the effect of activity on these interfaces is explored by closely examining the correlation functions.

An interesting aspect of our systems is the chirality of microswimmers. E. coli cells break their chiral symmetry when swimming close to solid boundaries. The interaction between these chiral swimmers and colloidal particles gives rise to chiral colloidal rotors. Furthermore, their assembly due to effective interactions results in dynamic clusters with persistent rotations, which markedly differ from those formed in equilibrium systems. At sufficiently high densities, our system exhibits several hallmark features of a percolation transition. A closer examination of the critical exponents associated with cluster size distribution, the average cluster size, and the correlation length near the critical density reveals deviations from the predictions of the standard continuum percolation model. Consequently, our experiments reveal a richer phase behavior of colloidal assemblies in active liquids.

In addition to studying collective behaviors, this thesis also examines the dynamics of individual colloidal particles in active media. Unlike Brownian particles, which display a Gaussian distribution in displacement, the colloids in active media show deviations from this form. These deviations depend on the size of the colloidal particles. We have characterized these deviations and interpreted the results using the concept of superstatistics. Finally, the dynamic clustering of colloids in the steady state was analyzed using aggregation and fragmentation models, by constructing a transition matrix and applying a monomer approximation.

List of publications

1. *Phase separation of passive particles in active liquids*; **Pragya Kushwaha**, Vivek Semwal, Sayan Maity, Shradha Mishra, and Vijayakumar Chikkadi, Physical Review E 108, 034603 (2023). The chapter 3 is based on this publication.

2. *Percolation of nonequilibrium assemblies of colloidal particles in active chiral liquids*; **Pragya Kushwaha**, Sayan Maity, Anjaly Menon, Raghunath Chelakkot, and Vijayakumar Chikkadi, Soft Matter, 20, 4699-4706 (2024). The chapter 5 is based on this publication.

3. *Kinetics of ordering of colloids in active liquids*; **Pragya Kushwaha**, Sayan Maity, Dibyendu Das, Sanjay Puri, and Vijayakumar Chikkadi, *in preparation*.

4. *Single particle and cluster statistics of colloids in active liquids*; **Pragya Kushwaha**, Sayan Maity, Raghunath Chelakkot, and Vijayakumar Chikkadi, *in preparation*.

Contents

Chapter 1

Introduction

1.1 Equilibrium phases of colloids

In 1827, while examining pollen grains suspended in water under a microscope, Robert Brown (1773-1858) observed a peculiar phenomenon: tiny particles emitted from the grains exhibited constant, jittery movement [1]. Although Brown did not propose a formal theoretical explanation, this motion was later named Brownian motion after him. In 1905, Albert Einstein (1879-1955) published three seminal groundbreaking papers. In one of them, he provided a quantitative framework for Brownian motion. Einstein's framework for Brownian motion demonstrated that micron-sized particles, now widely known as colloids, suspended in a liquid undergo random motion due to continuous collisions with the atoms and molecules of the suspension medium [2]. There were two key findings from Einstein's work: First was the bath molecules are in thermal equilibrium with the suspended particles, allowing the notion of kinetic theory to be extended to suspended particles, expressed by the equation of state $\Pi = nk_BT$. And the second was the atomistic nature of matter could be understood by estimating Avogadro's number N_A. By using the diffusion constant D, extracted from the mean square displacement, N_A was estimated to be: $N_A = \frac{RT}{D}\left(\frac{1}{6\pi\eta r}\right)$ [3]. These ideas were validated in experiments by Jean-Baptiste Perrin (1870-1942) in 1908, and had been awarded the Nobel Prize in Physics in 1926 for his contribution.

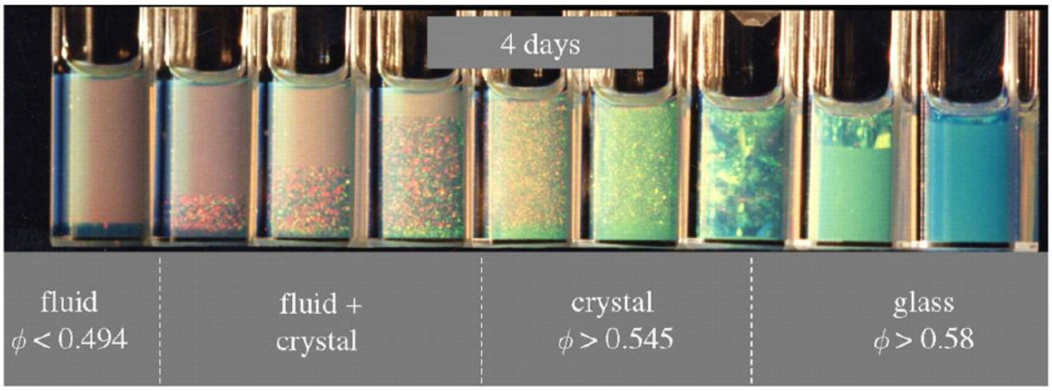

Figure 1.1: Various phases of colloids as the packing fraction of colloids ϕ increases, taken from the work of Pusey *et al.* [4].

All these studies have significantly contributed to the idea that colloids can be considered ”big atoms.” This concept attracted substantial attention and led to the emergence of a new area in colloidal physics. Researchers began to study the phase behavior of colloids to see if different phases, similar to those in atomistic systems, could be obtained. The first experiments on the various phases of colloids were conducted by Pusey et al, [4] who demonstrated the existence of liquid-like phases, crystalline phases, and non-equilibrium glassy and amorphous phases (Fig. 1.1). In these studies, the key factor is not temperature but the packing fraction of the colloids, which determines the various phases. Colloids typically range in size from a few nanometers to micrometers and are suspended in a continuous medium. Common examples of colloids include fog, smoke, milk, emulsions, paste, and paint. Because colloids are similar in size to the wavelength of visible light, they can be observed through the light microscopy. Additionally, the characteristic timescales of colloidal dynamics are of the order of seconds, allowing real-time measurement. Colloids have been used to study phenomena such as the glass transition [4–7], gelation [8, 9], and other complex behaviors that are challenging to observe in atomic systems [10–12]. The ability to visualize and measure the slow dynamics of colloids in real-time has enabled the study of these complex phenomena. One of the advantages of working with colloids is the tunability of their interactions. This can be achieved by adding salt [13], polymers [14], or altering surface chemistry [15]. Additionally, colloids can be engineered into different shapes, allowing for further control over interactions to achieve the desired phase behavior in the system [16].

Until now, our focus has been on systems where colloids are suspended in equilibrium media, maintaining thermal equilibrium and adhering to time reversal symmetry and the principle of detailed balance. However, it is intriguing to investigate the single particle dynamics and phase behavior of colloids when suspended in the nonequilibrium media, where neither time reversal symmetry nor detailed balance is maintained. Active matter systems exemplify such scenarios, where these two fundamental conditions do not hold. Even though the collective behavior of swimmers or active particles has been investigated extensively using theoretical and experimental models, the behavior of passive colloids in active media is relatively unexplored and poorly understood. The aim of this thesis is to highlight the novel aspects of this problem. We will examine the dynamics of single colloidal particles in active liquids and also the nature of order that emerges as a consequence of their collective behavior.

1.2 Active matter

Active matter refers to a class of material composed of individual agents that harness energy from their environment to execute mechanical work, often through self-propulsion. At the individual level, these systems breaks time reversal symmetry due to their directed motion, facilitated by continuous energy extraction, typically in the form of nutrition or chemical reactions, thus deviating from detailed balance [19, 23–27]. Examples of active matter range from natural phenomena such as bird flocks, animal herds, fish schools and bacterial colonies to synthetic systems like vibrating rods, Janus particles, and microtubule bundles with kinesin motors. Spanning from birds to bacteria, from cells to molecular motors, the biological realm teems with active entities. Initially, the study of active matter was predominantly motivated by its biophysical applications (Fig. 1.2(a)-(c)). However, in recent years, a plethora of synthetic active systems have been meticulously crafted in the laboratory, thereby opening avenues for the development of engineered artificial active materials (Fig. 1.2(d)-(f)). These systems, being continuously fueled by energy, operate far from equilibrium and

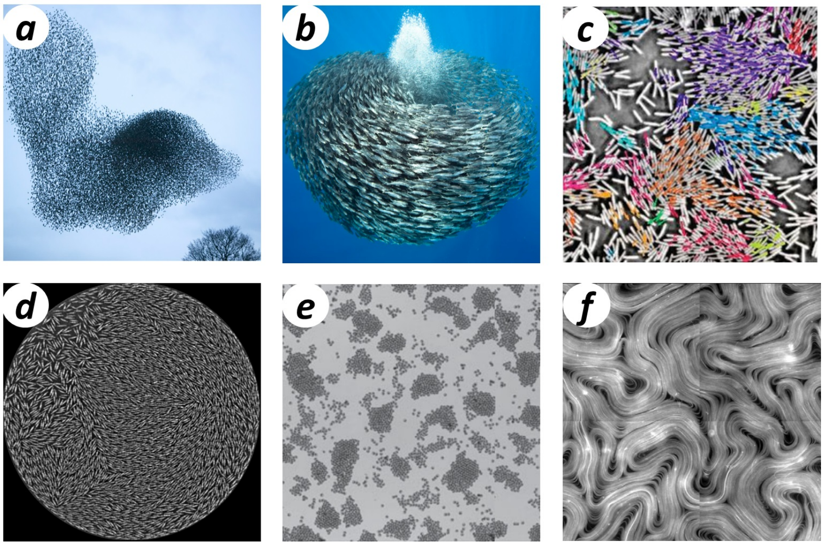

Figure 1.2: (a) Flock of birds. Image source: [17] (b) School of fishes. Image source: [18] (c) Swimming Bacillus subtilis bacteria, with arrows of the same color indicating the same dynamic cluster. Image taken from [19] (d) A snapshot showing nematic order in sinusoidally vibrated rods perpendicular to the image plane . Image adapted from [20]. (e) A system of self-propelled Janus colloids via induced-charge electrophoresis. Image taken from [21]. (f) Active nematic suspension composed of microtubule bundles and kinesin at a water-oil interface. Image adapted from [22].

display intriguing collective behaviors not observed in equilibrium conditions.

The collection of motile bacteria suspended in minimal motility media represents a system that is far from equilibrium, extensively studied for its diverse phenomena such as bioturbulence [28], bacterial vortices [29] and superfluidity [30]. In dense environments, bacteria exhibit collective behaviors driven by hydrodynamic and steric interactions, which differ significantly from the behavior of individual cells. To gain a better understanding, let's first examine the physics of individual bacteria.

1.3 Physics of individual bacterial motion

A well-studied and ubiquitous bacterium, Escherichia coli (E. coli) serves as a paradigmatic example of living active matter. It propels itself through the consumption of chemical energy derived from its environment. With a size in the micrometer range, E. coli operates in a regime characterized by low Reynolds numbers ($Re \sim 10^{-4}$), where viscous forces dominate over inertial forces [31] and flows are generated by the incompressible Stokes equations. At low Re, drag force on rigid body scale lineally with their instantaneous velocity. Consequently, the bacterium relies on continuous motion of its appendages, known as flagella, for sustained swimming. E. coli has flagella distributed across its body which are connected by rotary motors, facilitating movement in bulk through a coordinated interplay of run and tumble events. During a run, all flagella rotate in a counterclockwise direction, forming a bundle that propels the cell forward. While a tumble occurs when one or more flagella momentarily rotate clockwise, causing flagellar separation and prompting the cell to stop and change the direction. A run-to-tumble-to-run transition for swimming E. coli as a model for the reorientation mechanism is shown in Fig. 1.3. These tumbles typically last for 0.1 sec, whereas the runs last approximately 1 sec [32]. The dynamics of swimming, including run and tumble events, are influenced by external factors such as temperature [33], pH [34], and nutrient availability [35, 36].

1.3.1 E. coli in bulk

In bulk, E. coli swims under force-free and torque-free conditions. The force-free condition implies that the net force acting on the cell, which is the sum of all external forces (e.g., from the surrounding fluid) and internal forces (e.g., from the flagella pushing against the fluid), must balance out to zero as it swims. Mathematically, this can be expressed as:

$$\sum \vec{F}_{\text{ext}} + \sum \vec{F}_{\text{int}} = 0$$

The propulsion generated by the rotation of its flagella balances the drag forces acting on the cell body and the flagella, resulting in no net force. The torque-free condition means that the net rotational torque, both from external forces and internal forces, generated by the bacterium's flagella, acting on the bacterium is zero. Mathematically:

$$\sum \vec{\tau}_{\text{ext}} + \sum \vec{\tau}_{\text{int}} = 0$$

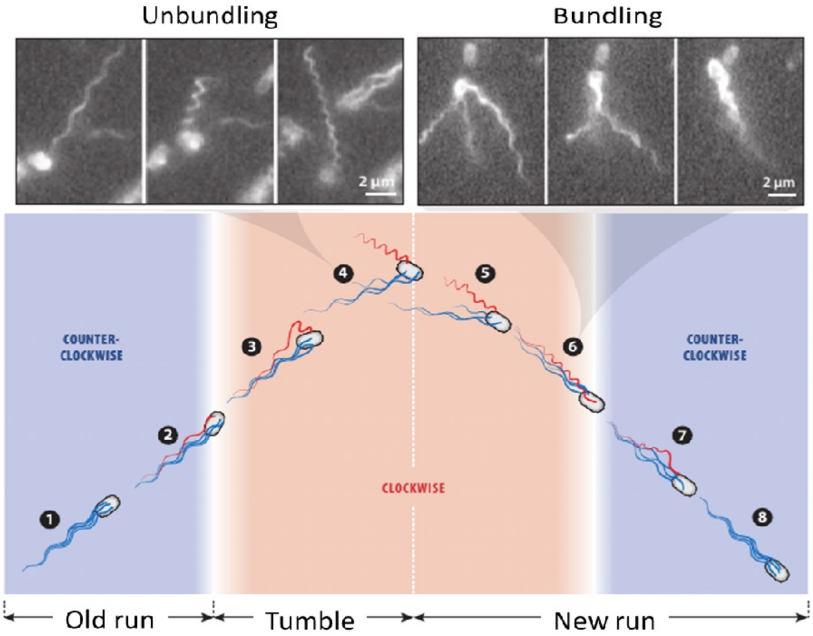

Figure 1.3: The reorientation mechanism in swimming E. coli can be modeled through a run-to-tumble-to-run transition. During the run phase, all motors rotate counterclockwise (indicated in blue). In the tumble phase, one or more motors switch to clockwise rotation (shown in red), causing the associated flagellar filament to undergo polymorphic changes and unbundle. The flagella then return to their normal bundled configuration as the bacterium initiates a new run. Image adapted from [32].

The rotation of the flagella generates torques. To remain torque-free, the cell body must counter-rotate, ensuring no net rotational acceleration. The rotation rate of the flagella is 10 times faster than that of the cell body [32]. This is schematically illustrated in Fig. 1.4(a).

1.3.2 E. coli near a solid interface

The presence of a boundary significantly influences the swimming behavior of E. coli bacteria. Interaction with a solid surface alters the hydrodynamic forces and torques acting on the bacterium, resulting in distinct swimming patterns compared to those in bulk fluid. One notable aspect of locomotion near boundaries is that E. coli bacteria are drawn toward and prefer to stay close to solid surfaces, resulting in longer runs along these surfaces due to hydrodynamic trapping. This leads to a higher concentration of bacteria near the solid surfaces [37]. Additionally, a remarkable feature of bacteria swimming near surfaces is their

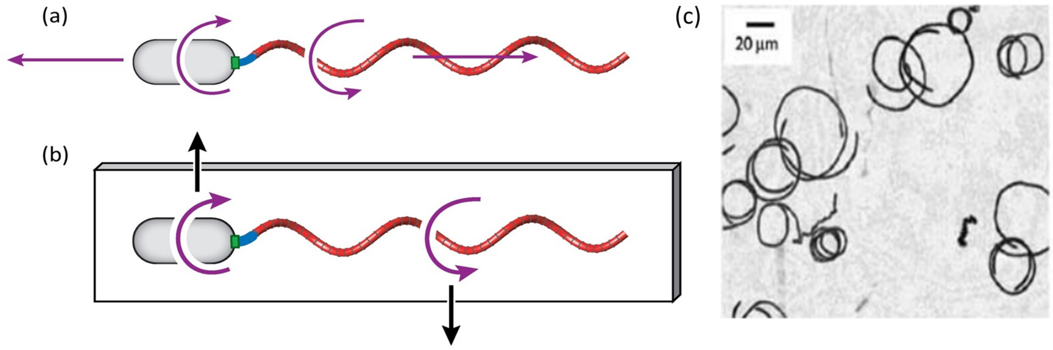

Figure 1.4: The schematic diagram illustrates (a) the force-free and torque-free motion of bacterium in bulk, (b) unbalanced force on bacterium near a solid interface causing a negative torque to rotate the cell in clockwise direction. Image adapted from [32]. (c) The clockwise circular trajectories of E. coli on the solid interface. Image taken from [38].

trajectories become circular, typically rotating clockwise when viewed from above the surface. This behavior is due to hydrodynamic interactions and the asymmetry in the propulsion mechanism, which lead to circular motion near boundaries [38].

When E. coli swims near a solid surface, the force-free and torque-free condition does not hold. The counter-clockwise (CCW) rotation of the flagella bundle, parallel to the no-slip surface, induces a net force in the downward direction. This occurs because the drag force on the flagella facing the surface is greater compared to the other side. Similarly, the clockwise (CW) rotation of the cell body induces a drag force in the direction of its rolling motion here in the upward direction as shown in Fig. 1.4(b) as black arrows. These forces are non-zero when the cell swims near surfaces, and their magnitude strongly depends on the distance to the wall. The spatial distribution of these unbalanced forces creates torque on the bacterium, causing the cell to rotate in the clockwise (CW) direction. This results in the characteristic clockwise circular trajectories of bacteria near the surface [32, 38]. Figure 1.4(c) shows the circular trajectories of bacteria on the solid interface taken from the experimental work [38].

1.4 Hydrodynamics of a single bacterium

Since microswimmers such as E. coli bacteria and Chlamydomonas algae, swim in the absence of external forces and torques, the flow field they create is not characterized by a

Stokeslet or a rotlet, which decay as r^{-1}. Instead, the flow field of force-free microswimmers decays as r^{-2} or even faster, known as a force dipole. Depending on their propulsion mechanism, they can be classified as either pushers or pullers. For example, E. coli bacteria are pushers, while Chlamydomonas algae are pullers [39]. For E. coli, as the flagella bundle rotates, it generates a forward thrust force by pushing against the fluid that propels the cell forward. Simultaneously, as the cell body moves forward, it experiences a drag force from the fluid that acts in the opposite direction to the thrust, effectively pulling the cell body backward. When these forces are balanced, there is no net force acting on the bacterium, leading to smooth, continuous motion. Fig. 1.5(a) illustrates the dipole flow field of bacteria.

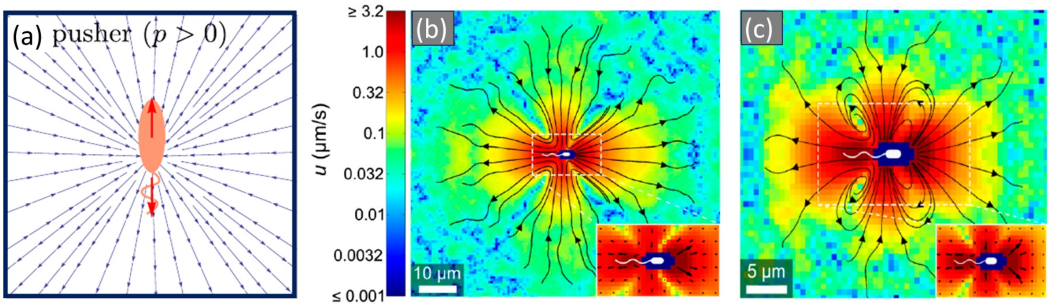

Figure 1.5: (a) The dipoler flow field created by E. coli by balancing the forward thrust and backward drag forces. Image taken from [39]. The experimentally observed flow field created by a single bacterium swimming freely is depicted both far from any surfaces (b) and near a wall (c). The streamlines represent the local flow direction, while the logarithmic color scale reflects the magnitude of the flow speed.. Image adapted from [40].

The pusher force dipole model serves as an effective approximation for the flow field generated by E. coli, both when they are far from surface and near no-slip boundaries. In a study by N. Drescher et al. [40], the velocity flow field of E. coli was examined experimentally and theoretically under these conditions, as illustrated in Fig. 1.5(b)-(c). When the bacterium is far from surfaces, the flow speed decreases with distance r from the center of cell body as $1/r^2$, characteristic of a force dipole. However, when E. coli swims near a wall, the flow decays much faster than in the bulk due to the influence of the nearby no-slip surface. The inward and outward streamlines form closed loops, as depicted in Fig. 1.5(c), a common feature of point singularities close to no-slip boundaries. By solving the stokeslet near a wall,

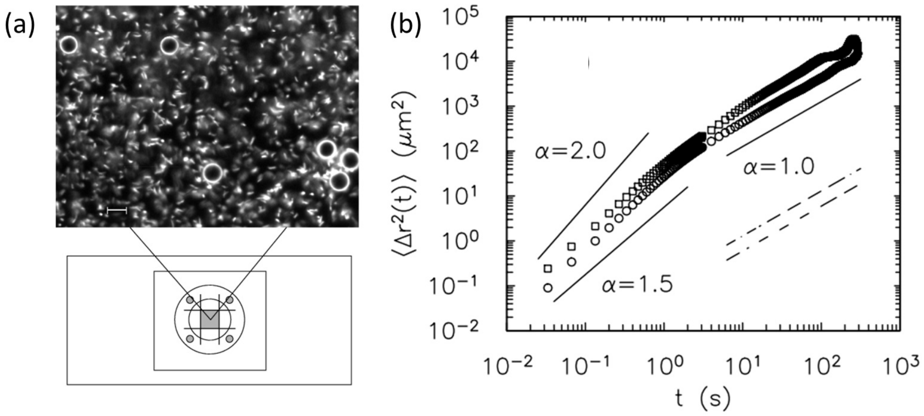

Figure 1.6: (a) The experimental setup and the fluorescence image of passive beads suspended in the bath of E. coli. (b) Mean square displacement of colloids showing super diffusive motion for short time scale and diffusive motion for longer time scale. Image adapted from: [41].

they derived the flow field of a force dipole near such a boundary. The resulting streamlines closely match the experimental observations. Nevertheless, the force dipole model tends to overestimate the flow to the sides and behind the cell body at short distances [40].

1.5 Influence of active liquid on individual passive particles

The previous sections described the motion of a pusher type of swimmer and the associated hydrodynamic flow fields. In this section, we'll see the influence of these active particles on the individual passive particles. In 2000, Wu and Libchaber [41] published a seminal paper studying the transport behavior of colloids in an active bacterial bath. When passive colloids are dispersed in a solution of motile bacteria as shown in Fig. 1.6(a), they display a generic two-time dynamics. At short times, colloids exhibit super-diffusive behavior, with the slope α of mean square displacement $\langle \Delta r^2(t) \rangle \propto t^\alpha$ ranging between $1.5 < \alpha < 2.0$. At longer times, the colloids show normal diffusive dynamics with $\alpha = 1.0$, having an enhanced diffusion coefficient D_{eff}, as shown in Fig. 1.6(b). The D_{eff} of colloids also depends on the density of bacteria. These micron-sized colloids dispersed in a suspension of E. coli appear to diffuse as fast as nano-particles in water. The authors attributed this phenomenon to the collective dynamics of the bacteria. However, subsequent studies demonstrated that even at very dilute bacterial densities, where no collective dynamics occur, the super-diffusive nature persists and is attributed to direct collisions of swimmers with the colloids [42] and hydrodynamic interactions between the bacteria and the colloids [34]. The movement of bacteria induces fluid flow in the surrounding medium, further enhancing the motion of the colloids. The long-time effective diffusion constant D_{eff}, in 2D, is defined as:

$$D_{\text{eff}} = \frac{1}{4}\frac{\delta\langle\Delta r^2(t)\rangle}{\delta t}.$$

It has been found that the effective diffusion constant D_{eff} is approximately 100 times greater than the normal thermal diffusion constant of colloids. One reason proposed is that the continuous activity of the bacteria creates an environment with an effectively higher temperature T_{eff}, leading to increased kinetic energy of the colloids. The dependence of D_{eff} on the size of colloids is often non-monotonic. Unlike thermal diffusion, where smaller particles typically diffuse faster due to less drag, active systems present a more complex picture where intermediate-sized colloids can experience maximum diffusion enhancement due to optimal interactions with the motile bacteria [43].

Before delving into the details of the phase behaviour of passive colloids in active liquid, it's important to first explore the phase behavior of purely active colloids. Several experiments have revealed nonequilibrium phase separation of active colloids, which is characterised by dynamic cluster formation [21,44,45]. The underlying physics of this phenomenon is well described by a theoretical model known as motility induced phase separation.

1.6 Motility induced phase separation (MIPS)

Motility Induced Phase Separation (MIPS) is a phenomenon observed in systems of self-propelled particles, such as active colloids or bacteria, where the particles undergo phase separation due to their motility [46–50]. This process is driven by the active movement of particles rather than by traditional thermodynamic interactions like attraction or repulsion. Although individual particles may not interact attractively, their persistent motion leads to

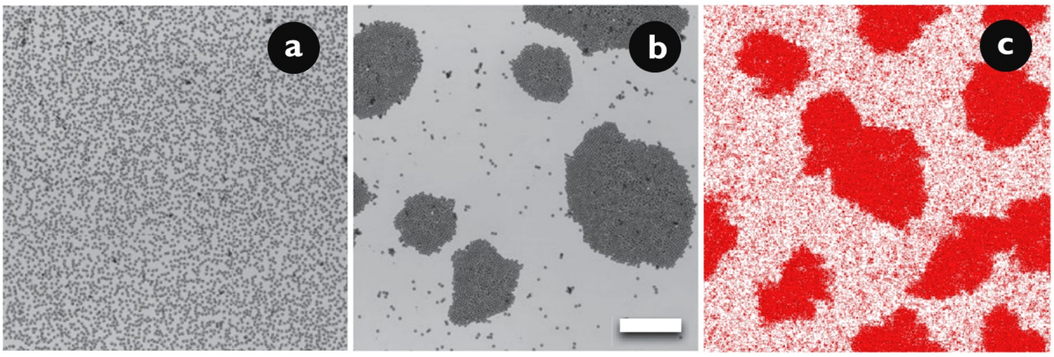

Figure 1.7: Experimental observation of MIPS (a) homogeneous phase (b) phase-separated state. Image adapted from [21]. (c) Dense and dilute phase of active colloidal fluids beyond critical density and activity levels. Image taken from [48].

effective interactions. When particles cluster, their motility is hindered, creating regions of high and low density. The motility of particles is influenced by local density. In high-density regions, particles experience more collisions, slowing down their movement and leading to aggregation. Reduced motility in dense regions leads to further aggregation, creating a positive feedback loop that drives phase separation. The system separates into dense (low motility) and dilute (high motility) phases, analogous to gas-liquid phase separation in equilibrium systems but driven by activity rather than thermal energy. Figures 1.7(a)-(b) shows the experimental observation of MIPS in active Janus colloids from homogeneous phase to dense and dilute phase [21], and Fig. 1.7(c) shows the dense and dilute phases of active colloidal fluids from the simulation work [48]. To further understand the underlying dynamics of MIPS, we turn to the Fokker-Planck equation.

In the context of MIPS, the Fokker-Planck (FP) equation governs the time evolution of the probability density function (PDF) of the particles in the system, $P(\mathbf{r}, \mathbf{u})$, where **r** is the position and **u** is the orientation or propulsion direction of the particles. Due to the active component of motion, the diffusivity of the system can be considered to be increased at a large time scale. Given sufficient coarse-graining, the motion of run-and-tumble particles (RTPs) and active Brownian particles (ABPs) resembles a diffusive random walk. Therefore, by maintaining the description of the active system with explicit coarse-graining, we can write the Fokker-Planck equation for active systems [46,51]. The equation can be written as:

$$\dot{P}(\mathbf{r},\mathbf{u}) = -\nabla \cdot [v_0 \mathbf{u} P(\mathbf{r},\mathbf{u}) - D_t \nabla P(\mathbf{r},\mathbf{u})] + D_r \nabla_{\mathbf{u}}^2 P(\mathbf{r},\mathbf{u}) \tag{1.1}$$

where, v_0 is the velocity of the particle, which depends on its position $v_0(\mathbf{r})$. D_t and D_r are the translational and rotational diffusion coefficients, respectively. To eliminate the angular dependency, the marginal density function $\rho(r)$ is introduced, which is obtained by integrating $P(\mathbf{r},\mathbf{u})$ over all possible orientations:

$$\rho(\mathbf{r}) = \int P(\mathbf{r},\mathbf{u})\, d\mathbf{u} \tag{1.2}$$

The effective Fokker-Planck equation for $\rho(\mathbf{r})$ then becomes:

$$\dot{\rho}(\mathbf{r}) = \nabla \cdot \left[-\frac{v_0(\mathbf{r})}{2D_r} \nabla (v_0(\mathbf{r}) \rho(\mathbf{r})) \right] - \nabla \cdot [D_t \nabla \rho(\mathbf{r})] = -\nabla \cdot \mathbf{J}(\mathbf{r}) \tag{1.3}$$

where,

$$\mathbf{J}(\mathbf{r}) = \left[-\frac{v_0(\mathbf{r})}{2D_r} \nabla (v_0(\mathbf{r}) \rho(\mathbf{r})) \right] - D_t \nabla \rho(\mathbf{r}) = -D \nabla \rho + \mathbf{V} \rho \tag{1.4}$$

with,

$$D(\mathbf{r}) = D_t + \frac{v_0^2(\mathbf{r})}{2D_r} \tag{1.5}$$

and,

$$\mathbf{V}(\mathbf{r}) = -\frac{v_0(\mathbf{r}) \nabla v_0(\mathbf{r})}{2D_r} \tag{1.6}$$

Given that we are already confined to long times within the coarse-grained approach, one can then use a steady state to simplify the problem. The simplest case is a flux-free steady state where $\mathbf{J}(\mathbf{r}) = 0$, then from Eq. 1.4:

$$-D \nabla \rho + \mathbf{V} \rho = 0 \tag{1.7}$$

By putting the values of $\mathbf{V}(\mathbf{r})$ and $D(\mathbf{r})$ and rearranging, we get the steady state solution of

Eq. 1.7:

$$\rho(\mathbf{r}) \propto \frac{1}{\sqrt{D_t + \frac{v_0^2(\mathbf{r})}{2D_r}}} \tag{1.8}$$

If translational diffusion, D_t, is not being included then the ratio of $\mathbf{V}(\mathbf{r})$ and $D(\mathbf{r})$ gives:

$$\frac{\mathbf{V}(\mathbf{r})}{D(\mathbf{r})} = -\nabla \ln \left[v_0(\mathbf{r})\right) \tag{1.9}$$

With D_t, the ratio of $\mathbf{V}(\mathbf{r})$ and $D(\mathbf{r})$ gives:

$$\frac{\mathbf{V}(\mathbf{r})}{D(\mathbf{r})} = -\frac{v_0(\mathbf{r})\nabla v_0(\mathbf{r})}{v_0^2(\mathbf{r}) + 2D_tD_r} \tag{1.10}$$

In the above discussion, we considered the deterministic evolution of a single particle's probability density governed by the diffusion-drift equations. By drawing a comparison to the case of a passive Brownian particle (PBP) in an external potential, we can derive the stochastic equation of motion for the coarse-grained density $\rho(\mathbf{r})$ within a multi-particle system. In this context, $\rho(\mathbf{r})$ represents a coarse-grained version of the microscopic density operator, rather than a probability density.

$$\dot{\rho}(\mathbf{r}) = -\nabla \cdot \mathbf{J}(\mathbf{r}) \tag{1.11}$$

$$\mathbf{J} = -D\nabla\rho + \mathbf{V}\rho + \sqrt{2D\rho}\boldsymbol{\Lambda} \tag{1.12}$$

Here, $D(\mathbf{r})$ and $\mathbf{V}(\mathbf{r})$ follow the relations defined by Eqs. 1.5 and 1.6, and $\boldsymbol{\Lambda}$ represents a unit vector-valued white noise. Eqs. 1.11 and 1.12 can be extended to account for situations where the spatial dependence of diffusivity D and drift velocity $\mathbf{V}$ arises from the motility parameters v and τ being functions of particle density ρ. In the subsequent equations, the term D_t is set to zero, as it does not influence the qualitative behavior. Applying the Fokker-Planck equation to the many-body probability $P[\rho]$, we derive the following result:

$$\dot{P}[\rho] = -\int d\mathbf{r} \left(\nabla \frac{\delta}{\delta\rho(\mathbf{r})}\right) \left[\mathbf{V}\rho - D\nabla\rho - D\rho\left(\nabla\frac{\delta}{\delta\rho(\mathbf{r})}\right)\right] P[\rho]. \tag{1.13}$$

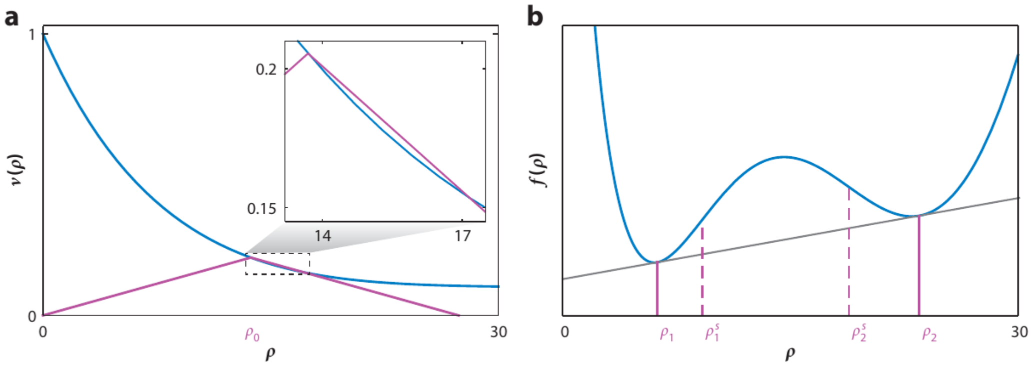

Figure 1.8: The effective free energy density $f(\rho)$ is constructed by mapping active particles with strictly local motility interactions to a fluid of interacting Brownian particles. (a) When $v(\rho)$ decreases sufficiently quickly, the resulting $f(\rho)$ exhibits (b) a region with negative curvature (spinodal), leading to a global equilibrium state characterized by the coexistence of the binodal densities ρ_1 and ρ_2. The instability condition ($f'' < 0$) can be interpreted geometrically on the $v(\rho)$ curve: draw a line from the origin to any point on the curve, then reflect this line across the vertical axis. If the slope of $v(\rho)$ is lower than that of the reflected line, the system is unstable. Image taken from [46].

Here, $[\rho]$ represents an arbitrary functional dependence on the coarse-grained density field $\rho(\mathbf{r})$. An equilibrium-like steady state, denoted by $P_{eq}[\rho]$, is defined by the absence of probability current:

$$\mathcal{J}[p_{eq}] = \left[\mathbf{V}\rho - D\nabla\rho - D\rho\left(\nabla\frac{\delta}{\delta\rho(\mathbf{r})}\right)\right]P_{eq}[\rho] = 0 \tag{1.14}$$

Using the ansatz $P_{eq} = \exp\left(-\beta\mathcal{F}\right)$, we see that Eq. 1.14 admits a flux-free solution, which is given as:

$$\frac{\mathbf{V}\left([\rho],\mathbf{r}\right)}{D\left([\rho],\mathbf{r}\right)} = -\beta\nabla\frac{\delta\mathcal{F}_{ex}}{\delta\rho}, \tag{1.15}$$

where, $\mathcal{F}_{ex}$ is the excess free energy of the system. And we have,

$$\ln[v([\rho],\mathbf{r})] = \beta\frac{\delta\mathcal{F}_{ex}}{\delta\rho} \tag{1.16}$$

If all the assumptions and conditions discussed so far are valid and Eq. 1.16 is satisfied, then the system of interacting active particles can be considered dynamically equivalent, at large length and timescales, to a passive Brownian particle (PBP) system characterized by the following free energy functional:

$$\mathcal{F}[\rho] = \frac{1}{\beta}\int \rho(\ln\rho - 1)d\mathbf{r} + \mathcal{F}_{ex}[\rho]. \tag{1.17}$$

Here, the integral can be interpreted as representing an ideal entropy contribution, while the excess component would, in the case of actual PBPs, arise from an interaction Hamiltonian. It's important to note that coarse-graining cannot establish a general equivalence between active systems, governed by microscopically irreversible dynamics, and passive systems, which obey detailed balance at all scales.

1.6.1 Without translational diffusion ($D_t = 0$)

Assume that ρ varies slowly in space and that the swim speed $v([\rho], \mathbf{r})$ depends isotropically on the values of ρ. By neglecting higher-order terms, we obtain:

$$v([\rho], \mathbf{r}) = v[\rho(\mathbf{r})] \tag{1.18}$$

From the Eq. 1.16:

$$\ln[v([\rho], \mathbf{r})] = \beta\frac{\delta\mathcal{F}_{ex}}{\delta\rho} \tag{1.19}$$

and

$$\mathcal{F}_{ex} = \frac{1}{\beta}\int^{\rho} \ln v(s)ds \tag{1.20}$$

From Eq. 1.17:

$$\mathcal{F}[\rho] = \frac{1}{\beta}\int\left[\rho(\ln\rho - 1) + \int^{\rho}\ln v(s)ds\right]d\mathbf{r} = \int f(\rho)d\mathbf{r} \tag{1.21}$$

The free energy density $f(\rho)$ is then:

$$\beta f(\rho) = \rho(\ln\rho - 1) + \int^{\rho}\ln v(s)ds \tag{1.22}$$

1.6.2 The effect of translational diffusivity ($D_t \neq 0$)

For simplicity, the Brownian translational contribution, D_t, has been neglected thus for. After restoring this term gives the modified integrability conditions, from Eq. 1.10 and 1.15:

$$\beta\nabla\frac{\delta\mathcal{F}_{ex}}{\delta\rho} = \frac{\tau v\nabla v}{v^2\tau + 2D_t} = \nabla\left(\frac{1}{2}\ln[v^2\tau + 2D_t]\right) \tag{1.23}$$

$$\mathcal{F}_{ex} = \frac{1}{\beta}\int^{\rho}\frac{1}{2}\ln\left[v^2(s)\tau + 2D_t\right]ds \tag{1.24}$$

From Eq. 1.17:

$$\mathcal{F}[\rho] = \frac{1}{\beta}\int\left[\rho(\ln\rho - 1) + \int^{\rho}\frac{1}{2}\ln\left[v^2(s)\tau + 2D_t\right]ds\right]d\mathbf{r} = \int f(\rho)d\mathbf{r} \tag{1.25}$$

The free energy density $f(\rho)$ is then:

$$\beta f(\rho) = \rho(\ln\rho - 1) + \int^{\rho}\frac{1}{2}\ln\left[v^2(s)\tau + 2D_t\right]ds \tag{1.26}$$

The free energy density gives the possibility of MIPS; the spinodal region corresponds to:

$$f''(\rho) \leq 0 \iff v^2\tau\left(1 + \rho\frac{v'}{v}\right) \leq -2D_t \tag{1.27}$$

Figure 1.8 illustrates the construction of the free energy density $f(\rho)$. Accurately determining the free energy of a MIPS system requires understanding the relationship between v and ρ. In the work of Tailleur and Cates [46], they proposed an example to illustrate it further.

The MIPS model effectively captures several features observed in experiments, particularly the dynamic clustering of active colloids. While the dynamics of individual colloids in an active bacterial bath have been extensively explored through experimental, theoretical, and numerical methods, the behavior of colloidal assemblies in a nonequilibrium active bath remains largely unexplored. The active fluctuations induced by the bacterial bath impact the clustering of passive beads, with this effect depending on the relative size of the colloids. As colloid density increases, these assemblies form clusters that span the entire field of view. Remarkably, even in this fluctuating environment, colloidal particles undergo coarsening and display ordering.

1.7 About thesis

The nonequilibrium assembly of colloidal particles in active liquids has emerged as a vibrant area of research, motivated by the potential to create novel dissipative structures with tunable properties unattainable in equilibrium systems. This thesis provides a comprehensive investigation of the phase behavior of colloids suspended in chiral active fluids of E. coli, exploring phenomena such as dynamic clustering, percolation of nonequilibrium assemblies, and coarsening in a quasi-2D environment.

Chapter 2 details the materials and methods used in the study, including bacterial culture, sample preparation, data acquisition, data analysis techniques, and the basic characterization of the active system under investigation.

Chapter 3 explores the dynamic clustering of colloids in suspensions of active liquids, which arises from the interplay of activity and an attractive effective potential. As the size of colloids increases, the effective potential becomes stronger, leading to larger clusters and eventually macroscopic phase separation. We highlight the novel aspects of active systems by comparing them to equilibrium systems, such as colloid-polymer mixtures.

Chapter 4 addresses the coarsening of colloidal assemblies in active liquids. The instability of a homogeneous mixture of colloids and swimmers leads to colloidal phase separation via active spinodal decomposition. This process is characterized by dynamic scaling of the spatial correlation function, resulting in non-Porod behavior with diffused interfaces. The correlation function reveals a cusp singularity associated with an exponent α. Furthermore, the power-law exponent θ of the cluster size distribution and the cusp exponent follow the relation $\theta + \alpha = 2$, as established in theoretical and numerical studies of systems with fluctuation-dominated phase ordering. These features point to a novel phase ordering of colloids in chiral active liquids.

Chapter 5 focuses on the percolation of colloidal assemblies in the chiral active liquid. The motion of E. coli near a solid-liquid interface breaks chiral symmetry, resulting in chiral curved trajectories. This effect becomes more pronounced with increasing colloidal particle size. Collisions between such swimmers and colloidal particles lead to persistent rotations of colloidal aggregates. As colloid density increases, the aggregates display several features of a percolation transition that deviate from the predictions of the standard continuum percolation model. We elucidate this aspect by analyzing the critical exponents associated with cluster size distribution, average cluster size, and correlation length near the critical density.

In the final chapter, we discuss the probability distribution of an isolated colloid displacement, which exhibits non-Gaussian statistics, and the aggregation and fragmentation dynamics of clustering, solvable using the master kinetic equation in specific cases. We conclude with a summary of the findings and present some fascinating future outlooks for this field of research.

Chapter 2

Experimental Methods

2.1 Introduction

This chapter provides a detailed description of experimental techniques used to culture the bacteria, prepare the sample, acquire the images, and analyze data to investigate the phase behavior of passive particles in an active chiral bacterial bath. These methods were carefully selected for their accuracy and significance in addressing the research objectives.

2.2 Materials and Methods

For bacteria-colloid system in the study, we have used polystyrene particles of sizes $7\ \mu m$, $10\ \mu m$, $15\ \mu m$, and $31\ \mu m$ as the passive colloids procured from MicroParticles, GmBH, Germany. For the suspension of bacteria as an active bath, we used motile non-florescent E. coli (strain U5/41 from NCMR) and fluorescent E. coli (strain D1 from NCBS). The bacteria were grown using Luria-Bertani (LB) broth as the growth medium and later suspended in a custom-made minimal motility (MM) medium for sustained motility without division. For polymer-colloid mixture, a suspension of polymer, Sodium Polystyrene Sulfonate (NaPSS) with molecular weight $\sim 10^6$ DA, was used as the polymer solution, and silica particles of sizes $3.34\ \mu m$, $10\ \mu m$, and $20\ \mu m$ as colloidal particles. Imaging was performed using a Leica DMi8 inverted microscope in Brightfield mode with a Basler camera and in confocal mode equipped with a photomultiplier tube (PMT) detector.

2.3 Preparation of active liquid and sample chamber

2.3.1 Growth curve of bacteria

Bacterial growth life span have four stages: lag phase, log (exponential) phase, stationary phase, and death phase. When E. Coli is inoculated in LB broth from an agar plate or frozen culture, the cells initially do not divide but acclimate to the environment, repair damage, and prepare for division, known as the lag phase. After acclimation, cells enter the log phase, rapidly dividing and doubling in number every 20 minutes under optimal conditions. This phase is crucial for experiments as cells are healthy and uniform, ideal for use. We typically harvest cells at $\mathrm{OD}_{600} \sim 1.3$ at the mid exponential phase. Following the log phase, cells enter the stationary phase, where division rates equal death rates due to nutrient depletion and toxic waste accumulation. Eventually, cells reach the death phase, where the death rate exceeds the division rate.

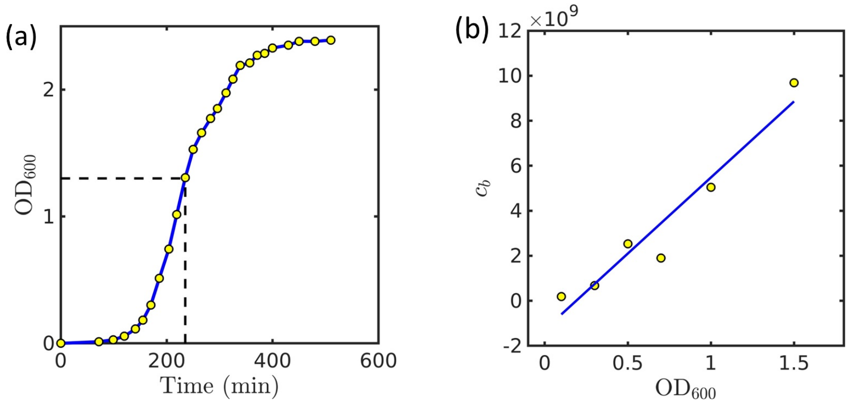

Figure 2.1: (a) Growth curve of E. coli, dashed line points out the mid log phase, (b) Cell density estimation by CFU counting method.

The growth curve of E. coli is shown in Fig. 2.1(a), with the horizontal axis representing growth time and the vertical axis showing OD_{600} values. Here, OD_{600} is the optical density of the bacteria at 600 nm wavelength, measured in the spectrophotometer. Optical density is the absorbance of the bacterial sample, determined by comparing the intensity of the trans-

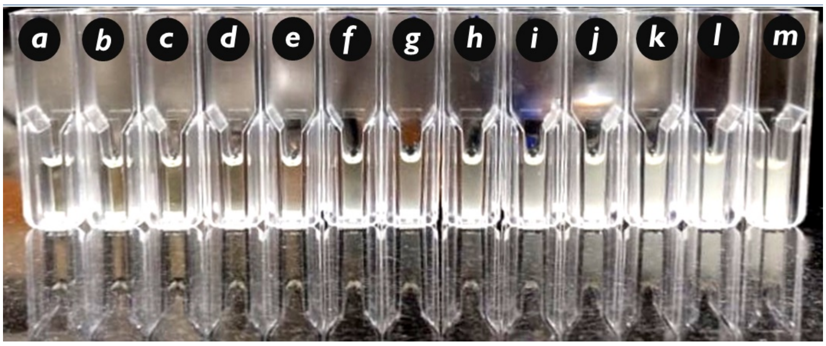

Figure 2.2: The different phases of E. coli growth media with increasing turbidity from left to right.

mitted light I_t with the intensity of the incident light I_0. It quantifies cell concentration in a sample by measuring the light passing through a cuvette containing a cell suspension and is calculated by using the well known Beer Lambert's law:

$$OD_{600} = -\log_{10}\left(\frac{I_t}{I_0}\right) = \epsilon \cdot l \cdot \rho$$

where ρ is the cell density, l is the light path length, and ϵ is a constant calibrated experimentally using cell counting. Figure 2.2 shows the various concentration of bacteria with increasing turbidity from left to right. OD_{600} measurements do not reveal the death phase as media turbidity remains constant. Techniques like colony-forming units (CFU) counting can detect the death phase. Our growth curve shows the lag phase, log phase, and stationary phase.

2.3.2 Cell density of E.coli

To estimate the cell density of E. coli, we used the Colony Forming Unit (CFU) counting technique. Serial dilution and counting of CFUs is a standard method for estimating the cell density of microbiological species such as bacteria. In our experiments, we diluted a sample of E. coli with a known Optical Density to one part per million into MM media. We then spread 100 μL of the diluted sample on an LB agar plate and incubated it overnight at 37°C. The next morning, we counted the individual colonies by eye, each originating from a single

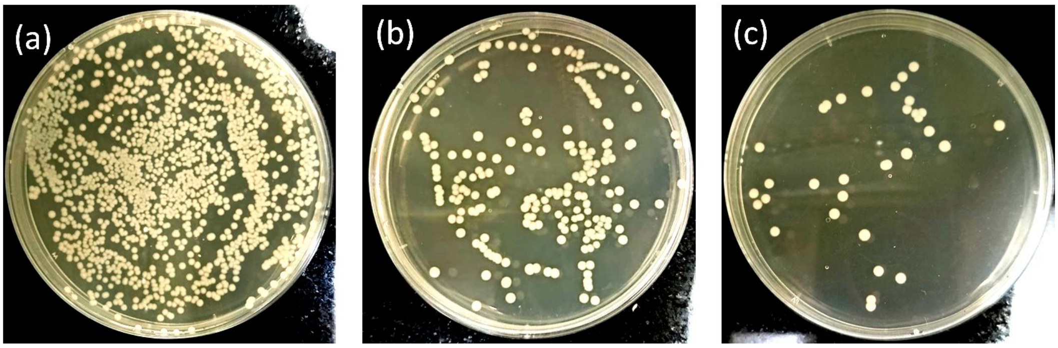

Figure 2.3: The agar plates with Colony forming units (CFUs) originated form single cell after overnight incubation, (a) overgrown (b) ideal for use (c) undergrown.

cell. Only plates with a suitable range of colonies (typically 30-300 colonies) are used for calculations to ensure accuracy. The images of agar plates with CFUs are shown in Fig. 2.3. The left plate is overgrown and the right one in undergrown, the middle one is used for the estimation of cell density. The results of these experiments are summarized in Fig. 2.1(b). This method provides a rough estimate of cell density. Based on the data, the bacteria density (c_b) is estimated to be around 6×10^9 cells/ml (b_0) when the OD_{600} value is 1.

2.3.3 Culturing of bacteria

The active suspensions were prepared by suspending E. coli cells in MM media. The cells were cultured following well-established protocols in the literature [52, 53]. For non-fluorescent E. coli cells (U5/41 type strain), the cells were grown overnight at 37°C on an LB agar plate containing 1% tryptone, 1% NaCl, 0.5% yeast extract, and 1.5% agar. A single colony was then added to 10 ml of LB broth and incubated at 37°C until the OD_{600} (optical density at 600 nm wavelength) reached 1.3. The bacterial cells were harvested and washed three times with minimal motility (MM) media by centrifugation at 3000 rpm for 5 minutes at room temperature to remove any LB broth residue. The pellet was then resuspended in MM media to achieve the desired concentrations. For fluorescent E. coli cells (D1), the cells were grown overnight at 30°C in 2% LB broth. The next day, the saturated culture was diluted 100 times in 2% LB broth and incubated at 30°C for 3 hours. The bacterial cells were then harvested and washed three times with MM media by centrifugation at 3000 rpm for

5 minutes at room temperature to remove any LB broth residue. The pellet was then resuspended in MM media to achieve the desired concentrations. For experimental purposes, it is essential to have swimmers that do not divide to ensure a constant number density of swimmers throughout the experiment and maintain motility for a longer duration. According to the literature, a well-defined chemically defined media proposed by J. Adler et al. [52] achieves this. In this motility media, bacteria remain motile without division. The motility media contains: A buffer to maintain a pH of 7.0 (a combination of K_2HPO_4 and KH_2PO_4), A chelating agent to protect motility from inhibition by heavy metal traces (EDTA), An energy source (L-serine) [54]. Thus the composition of the custom-built minimal motility (MM) media is $10mM$ potassium phosphate (pH 7.0), $0.1mM$ EDTA, 0.002% Tween-20, and 50 mM L-Serine. In this media, bacteria remain motile without dividing.

2.3.4 Sample preparation

To prevent beads from sticking to the coverslips, we coated them with PEG-8000 [55]. First, we washed the coverslips with a 3 M NaOH solution for 15 minutes to remove oil and dust, then rinsed them three times with DI water to eliminate any NaOH residue. Next, we performed Piranha cleaning by immersing the coverslips in a mixture of H_2SO_4 and 30% H_2O_2 in a 3:2 ratio inside a fume hood for 45 minutes. After this period, we rinsed the coverslips 3-4 times with DI water and dried them on a hot plate or using liquid nitrogen gas. We then immersed the coverslips in a silane solution for 6 hours inside a vacuum desiccator. After 6 hours, we removed the silane, washed the coverslips with acetone, and dried them thoroughly on a hot plate. Meanwhile, approximately two hours before the acetone wash, we melted the required amount of PEG 8000 powder in a beaker on a hot plate at $90_{\circ}$C. After the acetone wash, we added the dried coverslips to the molten PEG-8000, maintaining the temperature at 90-100°C for 60-70 hours. Following this period, we rinsed each coverslip with warm DI water to remove any adhered PEG-8000, dried them using an N_2 dryer, and stored the coverslips individually wrapped in threadless tissue. The observation chamber was constructed using double-sided tape with a circular cavity of $1cm$ diameter and $100\mu m$

depth, which was glued to a PEG coated coverslip. The circular cavity was created using a laser cutting facility available in the workshop at the Department of Physics, IISER Pune. A sketch of the sample chamber is shown in Fig. 2.4 The dimensions of the system are not to scale. Depending on the experimental requirements, we use double-sided tape with either one or two circular cavities. For experiments lasting about 1 hour, we use a single cavity filled with the suspension of colloidal particles and E. coli; for longer durations, we use double-sided tape with two cavities. One cavity is filled with the suspension of colloidal particles and E. coli, while the other contains DI water. A cover glass on top of the spacer minimizes evaporation losses and it has small openings in two corners to prevent oxygen depletion, as shown in the schematic diagram.

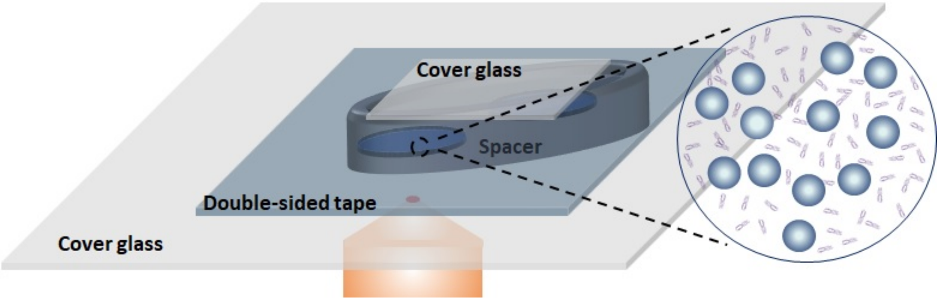

Figure 2.4: Sketch of the sample chamber used in our experiments. The dimensions of the system are not to scale. The double-sided tape has a thickness of $100\mu m$ and it has two circular cavities. One of them is filled with the suspension of colloidal particles and E. coli, and the other cavity contains DI water. The cover glass on top of the spacer minimizes the evaporation losses.

2.4 Data acquisition and Data analysis

After preparing the sample, we place it on the stage of a Leica Dmi8 confocal inverted microscope and acquire images using 5X, 10X, 20X, 40X, and 63X objectives as needed. For colloid-bacteria mixtures, colloid-polymer mixtures, and very dilute bacteria, we capture bright-field images using a Basler acA2040-180km camera with a resolution of 2048 px×2048 px and a sensor size of 11.3 mm × 11.3 mm at desired frame rate. The camera is interfaced with a Bitflow frame grabber through a custom-built LabVIEW program. In spe-

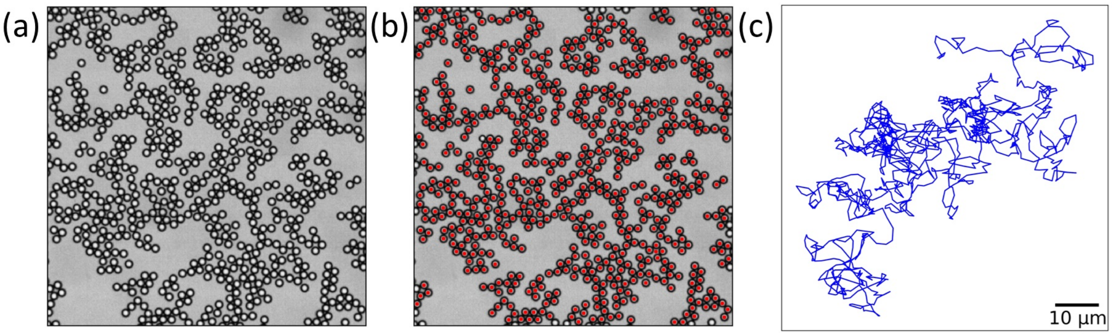

Figure 2.5: (a) Bright field image. (b) The overlapped features/centres of the particles on the bright field image. (c) Trajectory of a single isolated colloid in the active bath after tracking.

cific cases where fluorescent bacteria are used, images are captured in confocal mode using PMT detectors.

2.4.1 Feature finding and tracking by trackpy

For data analysis, we used the Trackpy library to find the position of the colloids. The Crocker and Grier algorithm [56], utilized in Trackpy, is a robust method for locating colloidal particles in microscopy images by identifying bright features against a darker background. The algorithm processes images with a bandpass filter to enhance features of a specific size range while suppressing high-frequency noise and low-frequency variations. It identifies local maxima within a specified pixel radius, corresponding to the brightest spots representing potential colloid positions. To achieve subpixel precision, the positions of these identified features are refined using Gaussian fitting or centroid estimation. Additionally, thresholding and morphological operations are applied to reduce noise and ensure that only significant features are considered. The raw image taken in the bright field microscopy is shown in Fig. 2.5(a) and the overlapped center positions on the image after feature finding is shown in Fig. 2.5(b). Once the particle centers are identified in all the images. These positions are then linked to construct trajectories that describe particle motion using the algorithm devised by Crocker and Grier, implemented in the trackpy library. The algorithm minimizes the sum of squared displacements of particles in successive frames. It only considers particles within a range from the old position to reduce complexity. If no match is

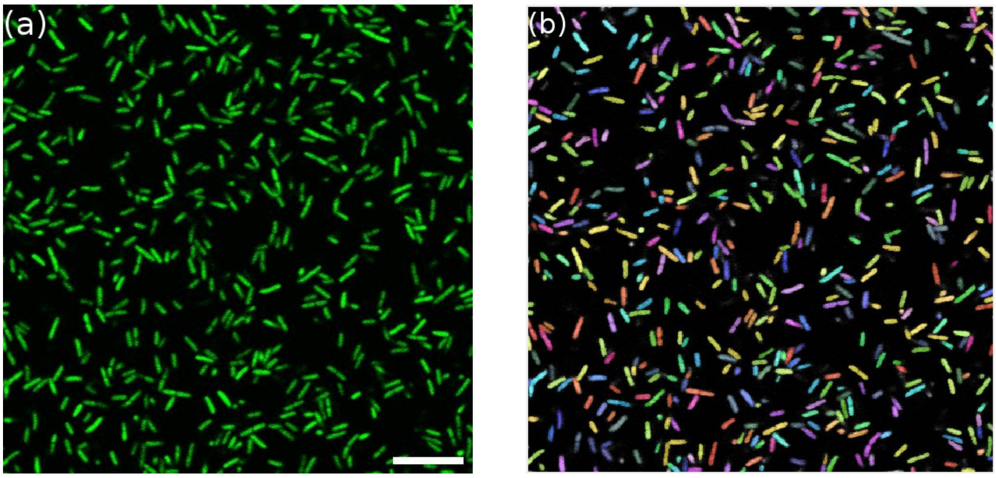

Figure 2.6: The tracking of positions for the dense bacterial systems: (a) Fluorescent image of bacteria at density $c_b = 10b_0$, scale bar measures $10\mu m$ (b) The mask of bacteria morphology captured by Omnipose algorithm [57].

found in the next frame, the particle is considered lost, typically at the boundaries of the imaged volume. These steps are repeated for successive frames to construct particle trajectories. Figure 2.5(c) shows the trajectory of a single particle tracked and linked by the trackpy. To track very dilute bacteria we have used the same method. First threshold and binarise the images then tracked them using trackpy.

2.4.2 Tracking of individual bacterium in dense systems

For some cases where the density of bacteria is high, tracking them using Trackpy becomes difficult. In such cases, we have utilized a deep neural network image-segmentation algorithm called Omnipose [57]. Omnipose excels in identifying bacteria in dense environments where Trackpy fails. This algorithm comes with various pretrained models, and users can further train their own models with modifications and improvements. Figure 2.6(a) shows the fluorescent image at bacterial density $c_b = 10b_0$. By employing the modified Omnipose model, we obtain masks of bacteria, as shown in Fig. 2.6(b). With these masks, we use a custom-built algorithm to extract the positions and orientations of the bacteria. This information allows us to analyze other required parameters. To track the trajectories of the bacteria, we employ the LapTrack algorithm from the work by Kawaguchi [58]. Once the trajectories are determined, we use this data to calculate the velocities of the bacteria.

2.4.3 Particle image velocimetry analysis

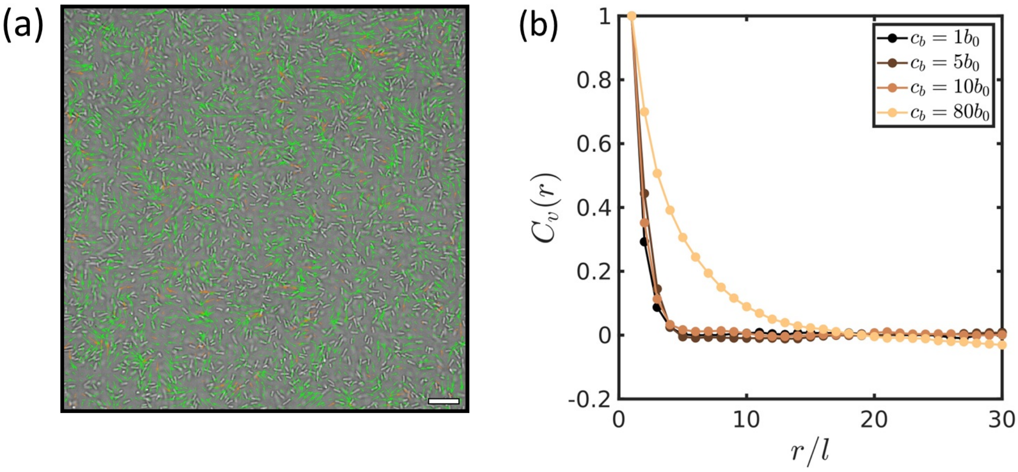

Figure 2.7: (a) The velocity field overlapped on the raw image, green arrows are the velocity field and orange arrow are the extrapolated field, the scale bar measures $20\mu m$, (b) The velocity correlation of various bacterial densities $c_b = 1b_0,\ 5b_0, 10b_0$ and $80b_0$.

Particle Image Velocimetry (PIV) is a widely used technique for measuring fluid velocity fields by tracking the movement of particles suspended within the fluid. These tracer particles are embedded in the fluid and are assumed to follow its flow dynamics closely. During the experiment, a laser sheet illuminates the fluid, and a high-speed camera captures a series of images of the particles at different time intervals. The displacement of these particles between consecutive images is analyzed by evaluating the cross-correlation of small sub-images (interrogation areas) to determine the fluid's velocity field [59]. In studies involving bacteria, which serve as both flow generators and markers, PIV has been used to calculate the flow fields generated by bacterial motion in various studies [28, 29, 60, 61]. For our analysis, we employed PIVlab, a MATLAB-based program to perform the PIV calculations for analysing the flow field of bacteria. After processing with PIV, the resulting bacterial velocity field for $c_b = 5b_0$ is shown in Fig. 2.7(a), where green arrows represent the velocity field and orange arrows indicate the extrapolated field. The scale bar corresponds to $20\mu m$.

We calculate the spatial velocity correlation $C_v(r)$ using the instantaneous velocity fields of the bacteria, as a function of in-plane distance and averaging over the orientations of **r**. This correlation function $C_v(r)$ is expressed as:

$$C_v(r) = \left\langle \frac{\mathbf{v}(r)\cdot\mathbf{v}(r+dr) - \mathbf{v}^2(r)}{\mathbf{v}^2(r)} \right\rangle \tag{2.1}$$

Here, $\langle ... \rangle$ represents the ensemble average. Figure 2.7(b) illustrates the velocity correlation for different bacterial densities: $c_b = 1b_0,\ 5b_0, 10b_0$, and $80b_0$. The figure clearly demonstrates that there is negligible correlation between bacteria at densities up to $10b_0$, indicating that the active suspension used in our experiments remains well below the threshold for collective behavior.

2.5 Characterization of bacterial activity

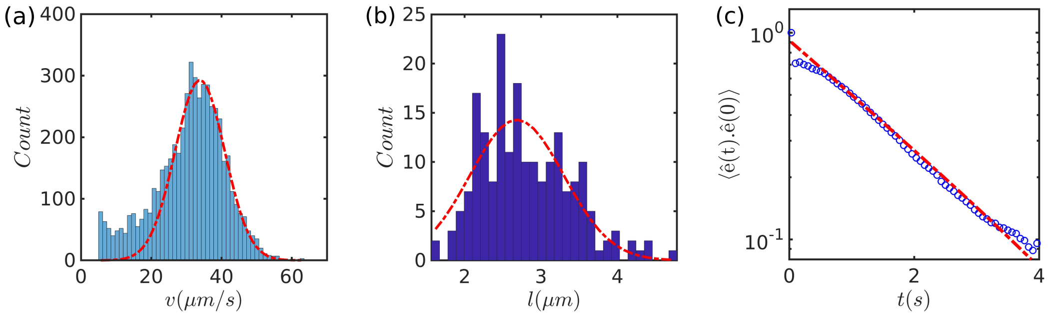

Figure 2.8: (a) Histogram of bacteria velocities. The average velocity is $\langle v \rangle = 33.84 \pm 9.98\ \mu m/s$. (b) Histogram of the size of the bacteria. The size of the bacteria is its length along the longer axis. The average length of the cells is $\langle l \rangle = 2.68 \pm 0.86\ \mu m$. (c) The rotational diffusion time of the bacteria was estimated from their normalised velocity auto-correlation function. The dashed line is an exponential fit to the data, which gives a rotational diffusion time of $\tau_r \sim 1.67\ s$.

2.5.1 The Peclet number of E.coli

To characterize the activity of the bacterial system, we captured a very dilute suspension of bacteria at approximately $c_b \sim 0.05$ and tracked the trajectories of individual bacteria. We then calculated the Peclet number of the bacterial suspension, which is defined as $Pe =$

$\tau_r v/l$, where τ_r is the persistence time, v is the average speed, and l is the average size of the bacteria. The average speed of the cells was found to be $v = 33.84 \pm 9.98\ \mu m/s$ and their average size was $l = 2.68 \pm 0.86\ \mu m$. The rotational diffusion time scale was estimated to be $\tau_r \sim 1.67\ s$. Figures 2.8(a)-(c) show the distribution of speeds and sizes, and the autocorrelations of cell orientations, respectively. The Peclet number for our system was calculated to be $Pe \sim 21$, indicating a moderate range of activity.

2.5.2 Chirality of bacteria

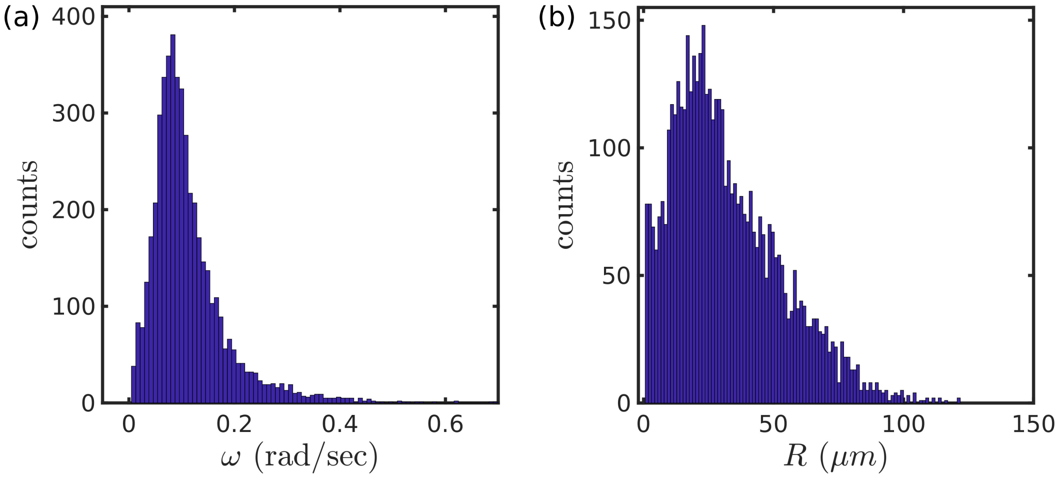

Figure 2.9: (a) Distribution of angular speed of bacteria for very dilute suspension $c_b = 0.01b_0$, the mean angular speed is $\omega = 0.11 \pm 0.08$ rad/sec. (b) Distribution of the radius of curvature of the bacterial trajectories, the mean radius of curvature is $R = 32.1 \pm 20.8\ \mu m$.

As discussed in Chapter 1 (Sec 1.3.1), near solid interfaces, bacteria swim in clockwise circular trajectories, hence also named as chiral swimmers. To account the chiral motion, we characterised their chirality by calculating the angular speed and the radius of curvature. We calculated the angular speed of the bacteria by tracking the their position over time, represented as $(x(t), y(t))$. From this, the angle $\theta(t)$ of the trajectory relative to the x-axis is determined using $\theta(t) = \tan^{-1}(y(t)/x(t))$. The angular displacement is then calculated as $\Delta\theta(t) = \theta(t + \Delta t) - \theta(t)$. The instantaneous angular speed $\omega(t)$ at each point is given by:

$$\omega(t) = \frac{\Delta\theta(t)}{\Delta t} \tag{2.2}$$

By averaging over all time intervals, we obtain the mean angular speed of the bacteria. Fig. 2.9(a) illustrates the distribution of angular speeds for various bacteria. The mean value and standard deviation of this distribution are $\omega = 0.11 \pm 0.08$ rad/sec.

To determine the radius of curvature R of a bacterial trajectory, we used the position of the bacteria over time, $(x(t), y(t))$. The radius of curvature R at any point along the trajectory is calculated using the following expression:

$$R(t) = \frac{(\dot{x}^2(t) + \dot{y}^2(t))^{3/2}}{\dot{x}(t)\ddot{y}(t) - \dot{y}(t)\ddot{x}(t)} \tag{2.3}$$

In this equation, $\dot{x}(t)$ and $\dot{y}(t)$ represent the first derivatives, while $\ddot{x}(t)$ and $\ddot{y}(t)$ are the second derivatives of the position with respect to time. The mean radius of curvature R for a single trajectory is obtained by averaging $R(t)$ over the entire trajectory. The distribution of R across various bacterial trajectories is illustrated in Fig. 2.9(b). The mean value and standard deviation of this distribution are $R = 32.1 \pm 20.8$ μm.

2.5.3 Chiral active bath

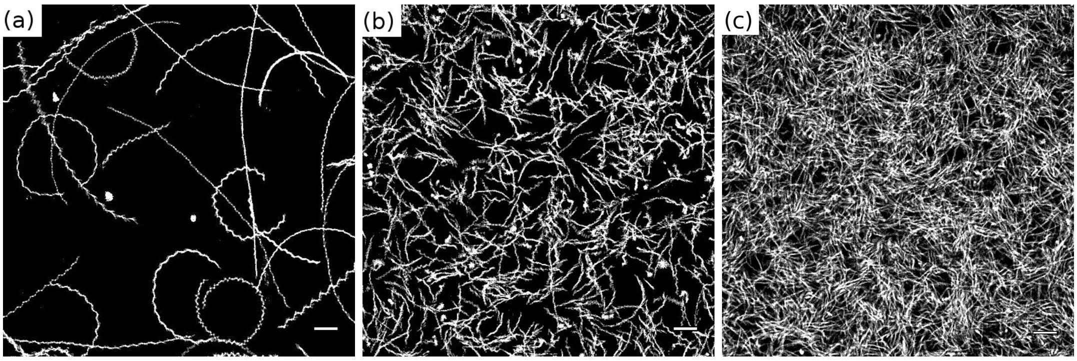

Figure 2.10: Trajectories of bacteria at three different concentrations of bacteria corresponding to $c_b = 0.01b_0$, $5b_0$ and $10b_0$ from left to right, respectively.

The suspension of these active chiral swimmers, E. coli near the solid interface, is referred to as a chiral active bath. Figures 2.10(a)-(c) display the circular trajectories of bacteria at the solid-liquid interface for three different concentrations: c_b = 0.01b_0, 1b_0, and 10b_0. At lower densities, the trajectories are predominantly circular; however, this characteristic diminishes as the concentration increases due to interactions between the swimmers. Even though the nature trajectories become non-circular at higher densities, the interactions between colloids and bacteria induce unbalanced tangential forces on the colloids, causing them to continue rotating persistently (see Sec 5.5.1).

2.6 Single particle characteristics

To characterize the dynamics of single passive particles, we suspended colloids in a bacterial active liquid at very dilute densities, ensuring well-separated and individual trajectories of the particles. We then calculated the mean square displacement (MSD) for various sizes of particles at different bacterial densities and the probability distribution of individual particle displacements over various time scales. The detailed results are presented in the following sections.

2.6.1 Mean square displacement

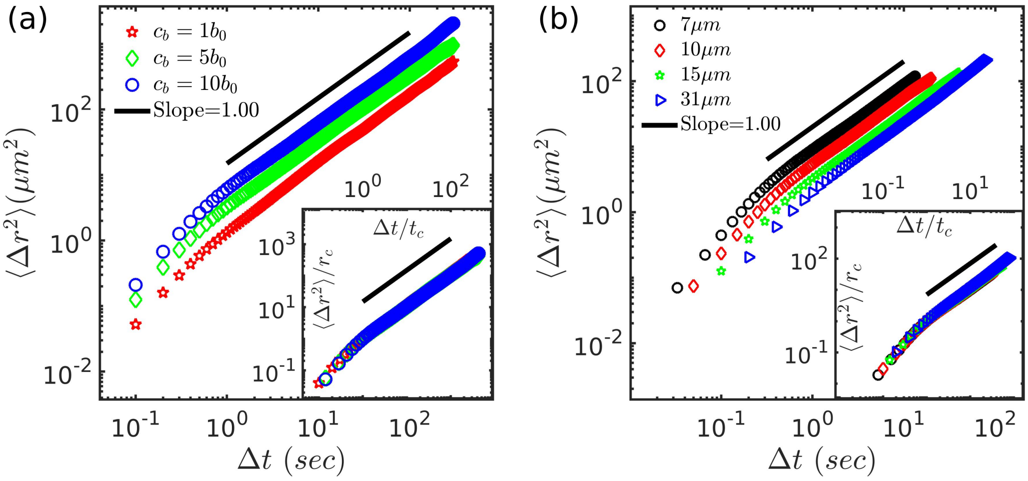

Figure 2.11: (a) The Means square displacement of particle of size $15\mu m$ at various bacterial densities $c_b = 1b_0, 5b_0$ and $10b_0$. Inset shows the scaled MSDs by t_c and r_c to fall on the master curve. (b) The Means square displacement of various particles of sizes $7\mu m$, $10\mu m$, $15\mu m$ and $31\mu m$ at a fixed bacterial density $c_b = 5b_0$. Inset shows the scaled MSDs by t_c and r_c to fall on the master curve.

To calculate the mean square displacement (MSD), we first determine the displacement of each particle over the desired lag time, τ. The lag time ranges from the time between individual frames, $\tau_1 = 1/f$, to the total length of the collected data, T [62].

$$1/f \leq \tau \leq T \tag{2.4}$$

where f is the acquisition frame rate. After tracking the images, we obtain the positions of all particles in every frame, represented as $r_{ij} = (x_{ij}, y_{ij})$, with i as the particle number and j as the frame number. We then calculate the displacement of particles over various lag times, given by:

$$\Delta r_{ij}(n\tau_1) = (\Delta x_{ij} = x_{i(j+n)} - x_{ij},\ \Delta y_{ij} = y_{i(j+n)} - y_{ij}) \tag{2.5}$$

The time-averaged MSD calculated from Δr_{ij} of the i-th particle is given as:

$$\langle \Delta r_i^2(\tau) \rangle_t = \langle \Delta x_i^2(\tau) \rangle_t + \langle \Delta y_i^2(\tau) \rangle_t \tag{2.6}$$

Then the ensemble-averaged MSD over all individual trajectories at each lag time τ is given as:

$$\langle \Delta r^2(\tau) \rangle = \frac{1}{N_t} \sum_{i}^{N_t} \langle \Delta r_i^2(\tau) \rangle_t \tag{2.7}$$

Here, N_t is the total number of particles considered.

Figure 2.11(a) shows the MSD of particles of size 15 μm at various bacterial densities: $c_b = 1b_0$, $5b_0$, and $10b_0$. The MSD curve displays two time regimes as discussed in section 1.5. In the short-time regime, colloids exhibit super-diffusive motion, while in the longer-time regime, they restored to diffusive behavior having slope of 1, with enhanced diffusion coefficient D_{eff}. Additionally, the MSD of colloids depends on the bacterial density c_b. When the MSD is rescaled by the crossover time t_c on the horizontal axis and the crossover mean squared length r_c on the vertical axis, all the curves collapse onto a single master curve, as shown in the inset of Fig. 2.11(a). The values of l_c, r_c and D_{eff} is given in the table 2.1.

c_b (b_0)	D_{eff} ($\mu m^2/sec$)	t_c (sec)	r_c (μm^2)
1	0.4295	1	1.3369
5	0.8287	0.7	2.1944
10	1.5786	0.7	4.0337

Table 2.1: The values of the effective diffusion coefficient D_{eff}, the crossover time t_c and the crossover mean square length r_c for colloids of size $15\mu m$ at various density of bacteria c_b.

Size (μm)	D_{eff} ($\mu m^2/sec$)	t_c (sec)	r_c (μm^2)
7	2.2627	0.43	3.7155
10	1.3129	0.5	2.5232
15	0.8279	0.7	2.1944
31	0.8002	1	1.9911

Table 2.2: The values of the effective diffusion coefficient D_{eff}, the crossover time t_c and the crossover mean square length r_c for colloids of various sizes at a fixed density of bacteria $c_b = 5b_0$.

Figure 2.11(b) displays the MSD of various particles of sizes 7 μm, 10 μm, 15 μm, and 31 μm at a fixed bacterial density of $c_b = 5b_0$. It also shows two time regimes, and for longer times, it reverts to normal diffusive behavior with an enhanced diffusion coefficient, D_{eff}. However, the values of D_{eff} do not follow a monotonic behavior, i.e., $D_{eff} \propto 1/R$, with the size of colloids R, as observed in the case of the thermal diffusion constant. Due to the limited data points, we cannot conclusively determine the exact power of the scaling. However, based on the three initial points, the scaling power appears to be approximately 1.31. In the work of A. Patteson et al. [43], where the effective diffusivity of colloidal particles in a bacterial bath was studied. Their findings show that the scaling of Deff with colloid size is non-monotonic, with the long-time effective diffusivity exhibiting a peak at a particular particle size. When the MSD curves are rescaled by the crossover time (t_c) and length (r_c), all curves collapse onto a single master curve, as shown in the inset of Fig. 2.11(b). The values of t_c, r_c, and D_{eff} are given in Table 2.2.

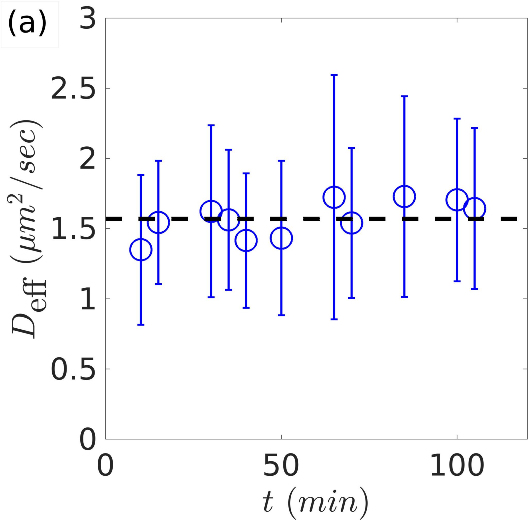

Figure 2.12: The effective diffusion constant D_{eff} of colloidal particles in active liquids at a bacteria concentration $c_b = 10b_0$. The area fraction of colloids is $\phi = 0.005$. The dashed line indicates the mean value. The error bars are obtained from the standard deviations of D_{eff}.

2.6.2 Constancy of the effective diffusion coefficient over time

Since our experiment runs for almost three hours in some cases, we calculated the effective diffusion constant, D_{eff}, of suspended isolated colloidal particles to ensure that bacterial motility remains feasible for this duration using the formula $D_{\text{eff}} = \frac{1}{4}\frac{\delta\langle\Delta r^2(t)\rangle}{\delta t}$ for longer time duration, as discussed in Sec 1.5. We determined D_{eff} at different times starting from the beginning of the experiment and results are shown in Fig. 2.12 is for the colloidal particles at very low area fraction $\phi \sim 0.005$ to maintain the isolated particle suspension to avoid interaction between them and the bacterial density is $c_b = 10b_0$.

Chapter 3

Phase Separation of Colloids in Active Liquids

The contents of this chapter are based on our published work [63]. The simulations were performed by the group of Prof. Shraddha Mishra at IIT BHU.

The transport properties of colloidal particles in active liquids have been studied extensively. It has led to a deeper understanding of the interactions between passive and active particles. However, the phase behavior of colloidal particles in active media has received little attention. Here, we present a combined experimental and numerical investigation of passive colloids dispersed in suspensions of active particles. Our study reveals dynamic clustering of colloids in active media due to an interplay of activity and attractive effective potential between the colloids. The strength of the effective potential is set by the size-ratio of passive particles to the active ones. As the relative size of the passive particles increases, the effective potential becomes stronger and the average size of the clusters grows. The simulations reveal a macroscopic phase separation at sufficiently large size-ratios. We will discuss the effect of density fluctuations of active particles on the nature of effective interactions between passive ones.

3.1 Introduction

The Brownian colloids self-assemble to display a wide variety of phases depending on their shapes and interactions [16, 64, 65]. Their equilibrium phase behavior is governed by the principles of equilibrium statistical mechanics [66, 67]. However, our understanding of the collective behavior of colloids far from equilibrium remains a challenge [68, 69]. In recent years, active matter has emerged as a new paradigm for understanding nonequilibrium systems [19, 23, 26, 27]. They are known to display many interesting phenomena such as flocking [70, 71], motility induced phase separation [72–74], active turbulence [75], superfluidity [53], that are absent in equilibrium systems. Therefore, active matter offers novel approaches to colloidal assembly in systems far from equilibrium. In this chapter, we have investigated the phase behavior of colloidal particles dispersed in active liquids.

Wu and Libchaber [41] did seminal experiments on the active transport of colloidal particles in suspensions of bacteria. They discovered anomalous diffusion and a large effective diffusion constant, when compared to diffusion at equilibrium, which inspired a slew of theoretical investigations and detailed experiments [42, 76–82]. The subsequent efforts have elucidated how enhanced diffusion arises due to an interplay of entrainment of colloids by bacteria, far-field hydrodynamic interactions, direct collisions, and the relative size of bacteria and colloid [79–81]. Further, the effective interaction between a pair of passive particles in active media has been predicted to be attractive, repulsive, and long-ranged, depending on the geometry of passive particles, the activity of active species, and their density [83–91]. This understanding has opened new routes to colloidal assembly mediated by active fluids [69, 92]. The phase behavior of active-passive mixtures is a topic of recent interest [23, 92–100], where experimental investigations are scarce [68, 69]. On the one hand, theory and simulations at high Peclet numbers have shown that homogeneous mixtures of active and passive particles are unstable. The underlying physics is similar to motility induced phase separation (MIPS) [95, 97]. On the other hand, in the diffusive limit, theory and simulations of nonequilibrium binary mixtures with different diffusivities and temperatures reveal phase separation [96, 99, 101] due to spinodal-like instability. Surprisingly, there is little known about mixtures at moderate Peclet numbers. This is the range where most of the active matter experiments involving living matter or synthetic systems, such as diffusio-phoretic colloids, fall. A recent study of colloids in active suspensions of bacteria in experiments and simulations reports dynamical clustering of colloids at moderate Peclet numbers [68]. The clustering was shown to be stabilized by the torque on active particles, which align their velocities tangential to the surface of colloids, leading to micro-phase-separation. The experiments were conducted over a range of densities of bacteria, while the simulations were performed over a range of Peclet numbers and torques of active particles to describe their phase behavior. However, the nonequilibrium steady states of the system are dependent on several other parameters, such as the size-ratio of colloids to bacteria, density of colloidal particles, and the hydrodynamics interactions, and our understanding of these aspects in active-passive matter is far from complete. Here we present a combined experimental and numerical study of the phase behavior of colloidal particles in active media, with a focus on the effect of size ratio on the phase behavior and the role of density fluctuations of active particles in mediating effective interactions between passive ones. Our investigations are motivated by well-studied system of colloid-polymer mixture [102, 103], where the equilibrium phase diagram is determined by the competition between thermal fluctuations and effective interaction that are dependent on multiple parameters such as size-ratio, polymer concentration and density of colloids.

3.2 Effective interactions between colloidal particles in different media

In order to understand the effective interaction between colloidal particles in an active bath, we first review the effective interactions in equilibrium systems, such as the colloid-polymer mixtures, which are equilibrium analog of colloid-bacteria mixtures, and the critical Casimir effect, where effective interaction is induced by thermal fluctuations of binary fluids at critical temperature.

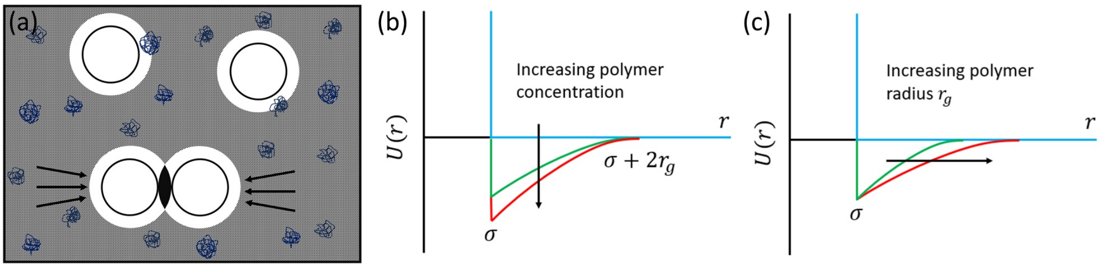

Figure 3.1: (a) Diagram showing the depletion zone and free volume: Each particle is surrounded by a depletion zone (white), an area near the particle surface that polymer molecule centers (blue) cannot access. The hatched black region represents the free volume V_{free} available to the polymer centers. The overlapping black area with arrows indicates the osmotic force driving particles closer together. Image based on [14,104]. (b) Effect of polymer concentration on potential depth: The cyan curve illustrates hard-core interaction, while the green and red curves represent the attractive interactions induced by polymers. The black arrow shows how increasing polymer concentration deepens the potential. Image adapted from [105]. (c) Effect of polymer radius r_g on potential range: The cyan curve depicts hard-core interaction, while the green and red curves show the influence of different polymer radii. The black arrow indicates that a larger polymer radius increases the potential range. Image adapted from [105].

3.2.1 Short-range depletion interaction in colloid-polymer mixtures

In a mixture of flexible non-adsorbing polymers and colloids, the polymers are treated as rigid objects that cannot penetrate the surface of the colloids. This creates a depletion zone around each colloidal sphere where the centers of polymer molecules, with a radius of gyration r_g, are excluded, as shown in Fig. 3.1(a). The white area represents the depletion zone, while the hatched black area is the free volume V_{free} available to the polymers, and the polymer coils are depicted in blue. Non-overlapping depletion zones, with a thickness equal to r_g, restrict the available free volume for polymer molecules. However, when these zones overlap, the free volume increases, allowing more space for polymer molecules. This overlap state is entropically favorable, contributing to an overall increase in the system's entropy. Although overlapped regions are inaccessible to polymers, they can approach the remaining surface of particles, creating a net osmotic force that brings colloidal particles closer together. This force can be strong enough to induce phase separation. The unbalanced osmotic pressure pushing particles together gives rise to an attractive pair potential named as the depletion potential $U_{dep}(r)$ and given as [14];

$$U_{dep}(r) = \begin{cases} +\infty & \text{for } r \leq \sigma \\ -\Pi_p V_{overlap} & \text{for } \sigma < r \leq \sigma + 2r_g \\ 0 & \text{for } r > \sigma + 2r_g \end{cases} \tag{3.1}$$

where, $\sigma = 2R$ is the diameter of colloidal particle, Π_p osmotic pressure of polymer, $V_{overlap}$ is the volume of overlapping depletion zones between two particles at an inter-center separation of r. The osmotic pressure is given as [106],

$$\Pi_p = n_p^{(R)} k_B T \tag{3.2}$$

where, $n_p^{(R)}$ is the number density of polymer in the free volume. The overlapped volume is given as [14]:

$$V_{\text{overlap}} = \frac{\pi}{6}\sigma^3(1+\xi)^3 \left(1 + \frac{3r}{2\sigma(1+\xi)} + \frac{1}{2}\left[\frac{r}{\sigma(1+\xi)}\right]^3\right) \tag{3.3}$$

where, $\xi = \frac{r_g}{R}$ is the size ratio of polymer to colloid. The depth of the depletion interaction is influenced by the osmotic pressure, which is itself dependent on the polymer concentration, as illustrated in Fig. 3.1(b). The range of this interaction is determined by the size of the polymer r_g, as depicted in Fig. 3.1(c). Since the interaction range is governed by the polymer radius r_g, the depletion interaction is considered a short-range interaction. By adjusting the polymer concentration and the ratio of polymer to particle sizes ξ, researchers have explored how the phase behavior of a particle assembly is influenced by the characteristics of their interactions. The polymer volume fraction is defined as:

$$\eta_p^{(R)} = \frac{4}{3}\pi r_g^3 n_p^{(R)} \tag{3.4}$$

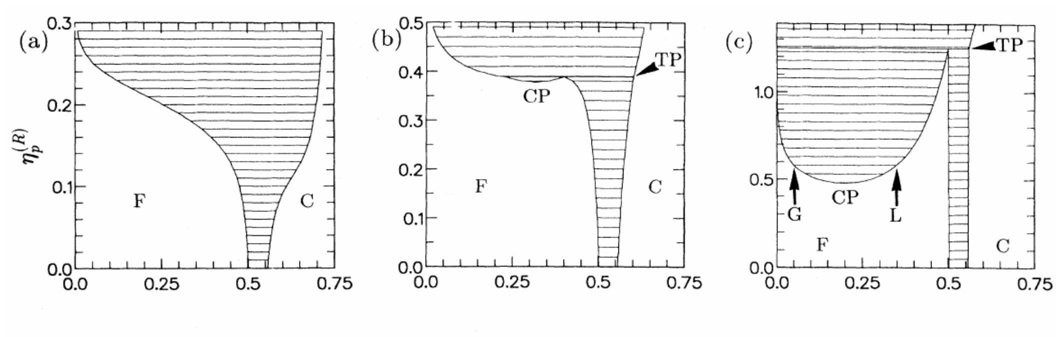

Figure 3.2: Phase Diagrams of Colloid-Polymer Mixtures: Shown in the $(\phi, \eta_p^{(R)})$ plane for size ratios (a) $\xi = 0.08$, (b) $\xi = 0.33$, and (c) $\xi = 0.57$. The horizontal axis represents the colloid volume fraction (ϕ), while the vertical axis represents the effective polymer volume fraction ($\eta_p^{(R)}$). The different regions in the diagram are labeled as F (fluid), C (crystal), G (gas), CP (critical point), and TP (triple point). Image adapted from [104].

where, $n_p^{(R)}$ is the number density of polymers in the free volume as defined above. Ilett et al. [104] investigated the phase diagram of a colloid-polymer mixture in the particle density-polymer concentration $(\phi - \eta_p^{(R)})$ plane for three different values of ξ: 0.08, 0.33, and 0.57. For $\xi \leq 0.33$, as illustrated in Fig. 3.2(a)-(c), adding polymer significantly broadens the fluid-crystal coexistence region. However, when $\xi \geq 0.33$, the phase diagram reveals the presence of a gas-liquid critical point (CP) and a triple point (TP) where gas, liquid, and crystal phases coexist. The horizontal tie lines indicate equal polymer chemical potentials between the two coexisting phases. For comparison with atomic systems, $\eta_p^{(R)}$ can be seen as analogous to the inverse temperature [14, 66, 104, 106].

3.2.2 Long-range interactions between colloids due to fluctuation induced forces

Forces induced by fluctuations between colloidal particles can be significantly long-range, such as the critical Casimir effect, which arises from thermal fluctuations in a binary fluid near its critical temperature. This effect results in either attractive or repulsive forces between colloidal particles and can extend over several particle diameters, making it longer than typical depletion interactions, which are usually short-range. The Casimir effect was

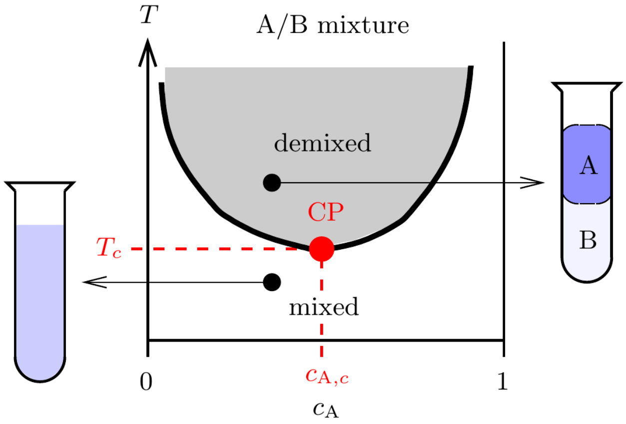

Figure 3.3: A schematic phase diagram illustrates a binary liquid mixture that features a lower critical point (CP). On the left side of the diagram, side views of a test tube containing the binary mixture in its homogeneous (mixed) phase are depicted. Conversely, the right side of the diagram shows the mixture in its separated (demixed) phase. The original image is adapted from [108].

first explored in the seminal work by Casimir [107], in which he investigated the confinement of quantum fluctuations of electromagnetic fields between two conducting plates in a vacuum. This force is inherently attractive and originates from the pressure difference between the modes allowed inside the plates and those outside. Generally, a Casimir-type effect occurs when fluctuations of any kind are confined within a Casimir geometry, such as between two parallel plates, a parallel plate and a sphere, or two spheres. In classical systems, an analogous phenomenon has been observed in binary mixtures. Here, the confinement of thermal fluctuations, especially near a critical point, leads to what is known as the critical Casimir effect. This effect can be controlled through surface treatments and temperature adjustments, allowing for tuning of the strength and sign of the Casimir force, making it either repulsive or attractive in nature [108, 109].

Figure 3.3 depicts the schematic phase diagram of a binary fluid mixture composed of fluid type A and B. In this diagram, the key thermodynamic parameters are temperature (T) and concentration c_A, which represents the mass fraction of component A in the mixture. At a given concentration c_A, the system remains homogeneous at lower temperatures. As temperature increases, the mixture undergoes a phase separation, resulting in regions rich in either component A or B, leading to inhomogeneity. The boundary between the homogeneous and phase-separated states is marked by a first-order transition line, which becomes continuous at the critical point (CP) on this line. To describe the phases, the order parameter $\delta c_A(x) = c_{AB}(x) - c_A$ is used, representing deviations in the local concentration of component A. The spatial correlation function of this order parameter is expressed as: $\langle \delta c_A(x) \delta c_A(x') \rangle - \langle \delta c_A(x) \rangle \langle \delta c_A(x') \rangle \propto \exp(-|x - x'|/\xi)$, where ξ represents the correlation length, which depends on both temperature and concentration c_A. When crossing the transition line, the correlation length ξ remains finite. However, as the system approaches the critical point, ξ diverges following the relation $\xi \sim \xi_0 |(T - T_c)/T_c|^{-\nu}$, where ξ_0 is a system-dependent constant, and ν is a universal critical exponent. The correlation length ξ defines the range of fluctuations, which become more pronounced as the system nears the critical point. When these fluctuations are confined within a Casimir geometry, critical Casimir forces emerge. If both the correlation length ξ and the confinement thickness L are significantly larger than the microscopic scale (e.g., molecular scale l_{micro}), the free energy of the confined system can be expanded in a series with decreasing powers of L, assuming a fixed ratio of L/ξ [108].

$$\mathcal{F}(T, L) = \mathcal{F}_{bulk} + \mathcal{F}_{surf} + S \frac{k_B T}{L^2} \Theta_{||}(L/\xi) + \text{corr.} \tag{3.5}$$

In this equation, $\mathcal{F}_{bulk}$ represents the free energy of the bulk medium, while $\mathcal{F}_{surf}$ accounts for the free energy associated with the presence of the confining walls. The third term captures the interaction energy between the two walls, which is influenced by the scaling function $\Theta_{||}$ and depends on the ratio L/ξ. Unlike the long-range Casimir forces observed in quantum systems, the interaction between the walls in this case is characterized by a finite range determined by the correlation length ξ. Specifically, this interaction is significant only when the separation L between the walls is comparable to or smaller than ξ, and it diminishes when L is much greater than ξ. A small change δL in the distance between the confining walls results in a corresponding change $\delta \mathcal{F}$ in the free energy, leading to a force $-\delta \mathcal{F}/\delta L$

on the displaced wall. The net force per unit area $F(T, L)/S$ is given by:

$$\frac{F(T, L)}{S} = \frac{k_B T}{L^3} \vartheta_{||}(L/\xi) \qquad \text{for } L, \xi \gg l_{micro} \tag{3.6}$$

where, $\vartheta_{||}(u) = -2\Theta_{||}(u) + u\Theta'_{||}(u)$ and it gives the force per unit area between the walls that accounts for both the scaling function and its rate of change, reflecting how the critical Casimir force varies with the separation L and the correlation length ξ. The critical Casimir effect has been used in numerous studies to manipulate the interactions between colloidal particles, enabling investigations such as colloidal phase transitions with controlled interaction, colloidal aggregation, and gelation [110–112]. In recent studies, a novel class of fluctuation known as giant number fluctuation has been observed in active matter systems consisting of living bacteria or synthetic active particles [19, 45, 113]. The confinement of these fluctuations has been found to give rise to Casimir-like forces. In the active matter system, numerical simulations with run-and-tumble dynamics have been employed to study the Casimir effect [84]. The magnitude of the attractive force between the walls in these systems depends on the run length, and a crossover from attraction to repulsion can be achieved by adjusting the separation and length of the walls. Similarly, studies employing Brownian dynamics simulations have demonstrated the ability to tune the effective force between two walls from long-range repulsion to long-range attraction by varying the density of active particles [85]. Experimental investigations involving colloidal particles suspended in a bath of bacteria and held in optical traps have also revealed the presence of an attractive force between the particles [90]. Similar experiments conducted with two parallel walls have shown a net attraction between the plates induced by the presence of bacteria on passive objects [114]. The force exerted by the active particles on passive objects, whether spheres or planes, is interchangeably referred to as active depletion force or active Casimir effect. This attractive force is responsible for the formation of colloidal clusters [68, 83]. Dolai et al. [98] reported in their simulation study that a binary mixture of small active and large passive particles exhibits clustering of passive particles. This clustering depends on the size ratio of passive to active particles. The study revealed that the surrounding active medium induces an effective attraction between passive particles, which leads to phase separation when the size ratios and volume fractions of the active particles are sufficiently large.

3.3 Experimental system and simulation models

3.3.1 Experimental method

The active-passive mixtures in experiments are realized using large colloidal particles and suspensions of motile bacteria. We have used Polystyrene colloids of sizes ranging from $5\mu m$ to $15\mu m$. The active suspensions were prepared using E.coli cells (U5/41 type strain). The cells were cultured using well established protocols in the literature [52,53]. The protocol for preparing the active liquid and observation chamber is detailed in Section 2.3. The bacteria density (c_b) of the sample with $\text{OD}_{600} = 1$ was estimated to contain 6×10^9 cells/ml (b_0). The density of bacteria in our experiments was fixed at $10b_0$, which was well below the density threshold for the onset of collective motion. The Peclet number, defined as $Pe = \tau_r v/l$ where τ_r is the persistence time, v is the average speed, and l is the average size of the bacteria, is approximately $Pe \sim 21$ for our system. See Section 2.5.1 for details.

The phase behavior of colloidal particles in suspensions of bacteria was investigated by varying the size and density of the beads at a constant density of bacteria. The diameters of the particles used in the experiments were $\sigma = 7\mu m,\ 10\mu m$ and $15\mu m$, and their density is varied from $\phi \sim 0.1 - 0.4$, where $\phi = N\pi\sigma^2/(4A)$ is the area fraction, N is the number of colloidal particles in the field of view of area A. The size-ratio $S = \sigma/l$ is defined as the ratio of the diameter of colloids to the length of the bacteria.

3.3.2 Simulation method

The simulations were performed using a binary mixture of active Brownian particles (ABP) with N_a small active particles of radius a_a and N_p big passive particles of radius a_p $(a_p > a_a)$ moving on a two dimensional frictional substrate. The active particles are associated with a self propulsion speed v and an orientation unit vector $\mathbf{v}_i = (\cos\theta_i, \sin\theta_i)$, where θ_i is the

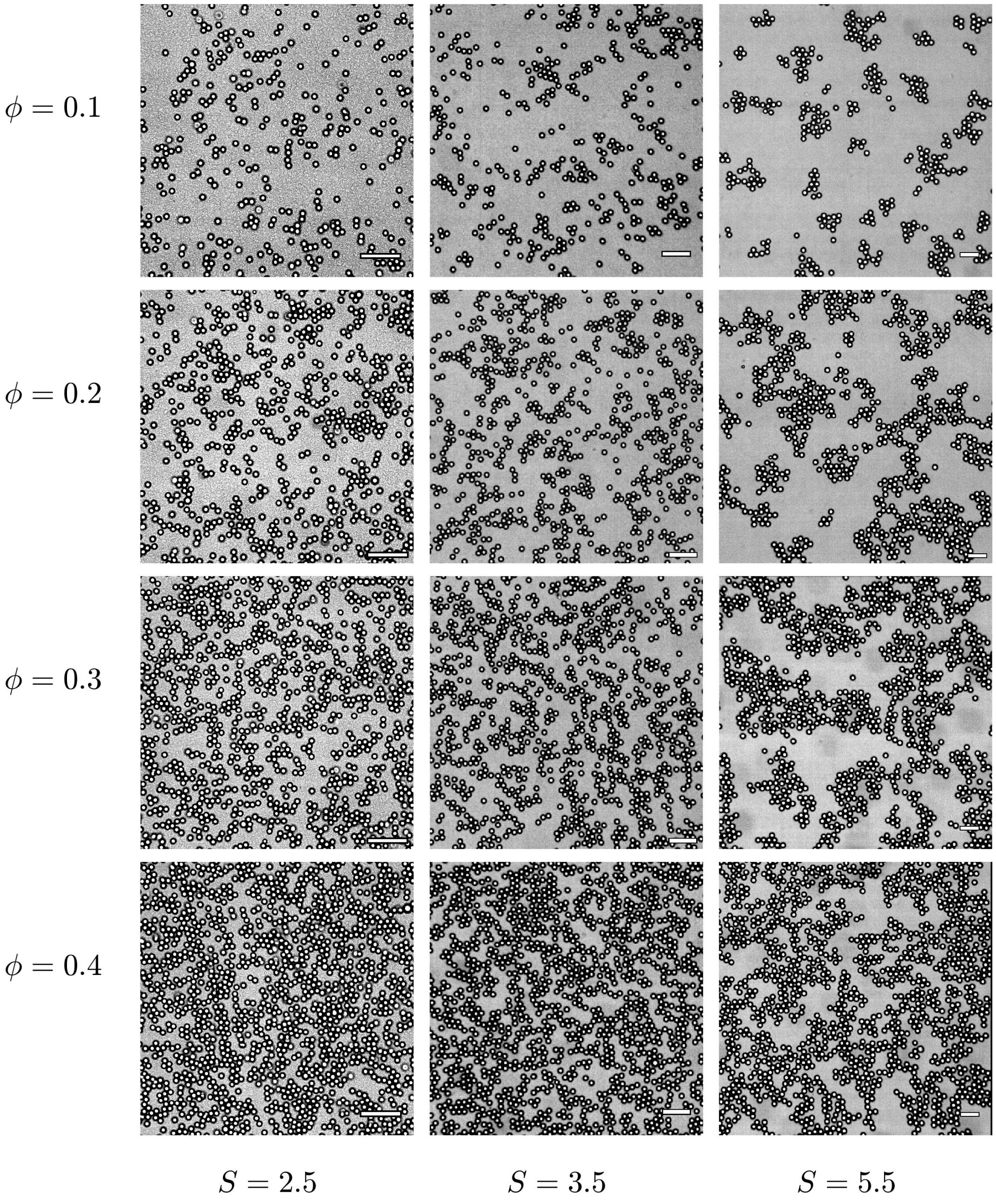

Figure 3.4: Bright field images for various area fractions of colloids $\phi = 0.1,\ 0.2,\ 0.3,$ and 0.4 and size ratio $S = 2.5,\ 3.5,$ and 5.5 at density of bacteria $10b_0$. The scale bar measures $50\mu m$. Field of view is of $50\sigma \times 50\sigma$.

angle between the velocity vector and a reference direction [47, 115, 116]. The motion of active Brownian particles (ABP) is governed by the following Langevin equations:

$$\frac{d\mathbf{r}_i}{dt} = v\mathbf{v}_i - \mu_1 \sum_{j \neq i} \mathbf{F}_{ij} + \sqrt{2D_T}\boldsymbol{\eta}_{Ti} \tag{3.7}$$

$$\frac{d\theta_i}{dt} = \Gamma \sum_{i} sin(\theta_i - \theta_{ij}) + \sqrt{2D_r}\eta_{ri}. \tag{3.8}$$

Here μ_1 is the mobility and $\mathbf{F}_{ij}$ is the force acting on particle i due to particle j. The noise term is defined as $< \eta_{ri,Ti}(t)\eta_{rj,Tj}(t') >= 2D_{r,T}\delta_{ij}\delta(t-t')$, D_T and D_r are the translational and rotational diffusion constants of active particles and Γ is the magnitude of torque that aligns the velocity vector of active particles tangential to the surface of passive particle [42] and $\theta_{ij} = \arg(\mathbf{r}_i - \mathbf{r}_j)$. The persistence length $l_p = v/D_r$ of active particles is constant in our simulations, it is set at $l_p = 20a_a$. The other constants in our simulations are $D_T = 0.005$ and $\Gamma = 1$.

The equation of motion for passive particles is

$$\frac{d\mathbf{r}_i}{dt} = \mu_2 \sum_{j \neq i} \mathbf{F}_{ij}, \tag{3.9}$$

where μ_2 is the mobility of passive particles. There is no translational noise in Eq. 3.9, so the dynamics of passive particles is only due to interaction force. We choose the mobility of both species to be the same i.e., $\mu_1 = \mu_2 = \mu$. Particles interact through short ranged soft repulsive forces $\mathbf{F}_{ij} = F_{ij}\hat{\mathbf{r}}_{ij}$, where $F_{ij} = k(a_i + a_j - r_{ij})$ when $r_{ij} \leq (a_i + a_j)$ and $F_{ij} = 0$ otherwise; $r_{ij} = |r_i - r_j|$ and k is a constant. The elastic time scale in our system is defined by $(\mu k)^{-1} = (150)^{-1}$.

We simulate the system in a square box of length l_{box}, with periodic boundary conditions. The system is defined by the area fractions $\phi_a = N_a\pi a_a^2/l_{box}^2$ and $\phi_p = N_p\pi a_p^2/l_{box}^2$ of the active and passive particles respectively, the activity v of active particles and the size-ratio $(S = a_p/a_a)$ defined as the ratio of the radius of a passive particle to the radius of an active

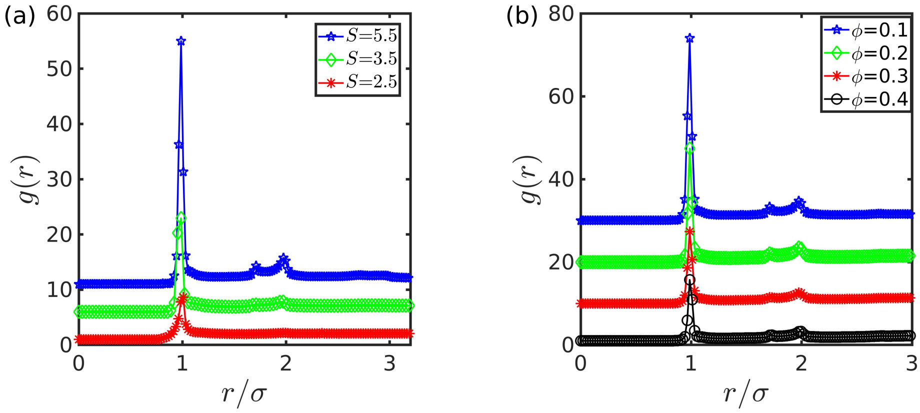

Figure 3.5: The structure of colloidal clusters in active liquids. (a) The pair correlation function $g(r)$ for $\phi \sim 0.10$ at $S \sim 2.5,\ 3.5,$ and 5.5. (b) The pair correlation function $g(r)$ at $S \sim 5.5$ for $\phi \sim 0.10,\ 0.20,\ 0.3$ and 0.4. The $g(r)$ curves are shifted along the y-axis for clarity.

particle. A random homogeneous distribution of active and passive particles in the box and with random directions for the velocity of active particles are the initial conditions in simulations. The Eqs. (3.7-3.9) are updated for all particles and one simulation step is counted after a single update for all the particles. The simulations does not include the hydrodynamic interactions that are present in experiments. The effect of hydrodynamic interaction can be included using coarse-grained studies similar to [117].

3.4 Experimental results

3.4.1 Dynamic clusters of colloids in active liquids and the effect of size ratio

We first present the experimental results. The colloids used in our experiments are non-Brownian as they are bigger than 5 μm. However, they diffuse in suspensions of bacteria due to active fluctuations with a characteristic super-diffusive motion on short time scales and a diffusive motion on long time scales. In the Fig. 3.4, we have shown the bright field images of the colloid-bacteria system at various area fraction $\phi \sim 0.1,\ 0.2,\ 0.3,$ and 0.4 with size ratios $S \sim 2.5,\ 3.5,$ and 5.5 at density of bacteria $10b_0$. The scale bar measures

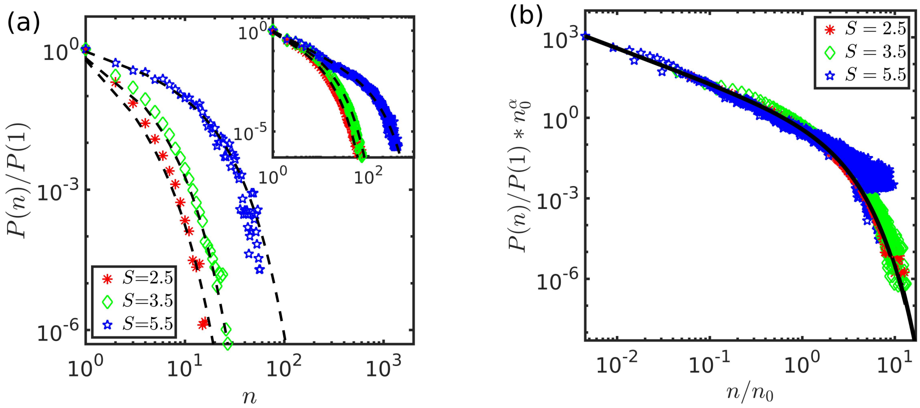

Figure 3.6: Size of colloidal clusters and the effect of size ratio. (a) Cluster size distribution in the main panel is shown for different size-ratios $S \sim 2.5,\ 3.5,$ and 5.5 at a density of $\phi \sim 0.10$. The symbols distinguish different size ratios. The inset shows the CSD plot for same size ratios at $\phi \sim 0.3$. (b) CSD plots for all ϕ and S overlappped at master curve. Black thick curve is master fitting curve.

$50\mu m$. The field of view of all images are $50\sigma \times 50\sigma$. To investigate their structural behavior in active suspensions, we analyze their pair correlation function $g(r)$, defined in 2D as:

$$g(r) = \frac{\rho_l}{\rho_g} = \frac{N}{2\pi r dr} \cdot \frac{1}{\rho_g} \tag{3.10}$$

where, ρ_l is local density at a distance between r and $r + dr$ away from the considered particle, ρ_g is the global density and N is the total number considered to calculate $g(r)$. The plot of $g(r)$ is displayed in Fig. 3.5(a), which corresponds to an area fraction of $\phi \sim 0.10$ and size ratios $S \sim 2.5 - 5.5$. Additionally, Fig. 3.5(b) presents the plot for $S \sim 5.5$ and $\phi \sim 0.1 - 0.4$. The normalized $g(r)$ curves are shifted along the y-axis for clarity. What is prominent is the presence of a sharp peak at $r = \sigma$, and additional peaks develop at $r = 1.7\sigma$ and $r = 2\sigma$ with increasing size ratio. The peak at 2σ indicates a second shell of neighbors, and the one at 1.7σ is a signature of hexagonal ordering in the cluster. These observations are evident in the bright field images presented in Fig. 3.4. The larger size ratios lead to larger clusters with enhanced order. These images are reminiscent of clustering in systems of purely active particles [73]. However, the clusters of passive particles in our experiments break and form much more rapidly for smaller size ratio. A real-time video of

ϕ	α	n_0		
		$S = 2.5$	$S = 3.5$	$S = 5.5$
0.1	0.5704	1.5026	2.2956	8.7437
0.2	0.9143	3.2158	4.6593	20.6330
0.3	1.1779	6.2079	8.4074	65.5227
0.4	1.2966	15.9624	22.6369	221.6055

Table 3.1: The power law exponent α and characteristic size of clusters n_0 at various ϕ and S.

dynamic cluster formation is presented in the supplementary video S1 [63] for $\phi \sim 0.10$ and $S \sim 2.5$. Recent simulations have reported similar dynamic clustering and traveling interfaces of active-passive particles that are not observed in our current study [95, 97]. One of the main difference between our experiments and these simulations are the large Peclet numbers used in simulations. Further, as reported by earlier investigations, clustering is a manifestation of an attractive effective potential between the passive particles due to active fluctuations [83].

We next turn our attention to cluster size distribution(CSD), $p(n)$, which is a count of clusters of n particles [98, 118]. The clusters in our experiments were determined by setting a distance criterion of $r_c \leq 1.1\sigma$ to identify pairs of particles as neighbors. This was set based on the position of the first peak of $g(r)$ in Fig. 3.5(a) to account for small polydispersity ($< 5\%$) in the size distribution of colloidal particles. The results of our analysis are presented in Figs. 3.6(a) and 3.6(b). The main panel in Fig. 3.6(a) shows CSD for varying size ratios of $S \sim 2.5,\ 3.5,$ and 5.5 at a density of $\phi \sim 0.1$. For small size ratios $S < 5$, $p(n)$ has an exponential form $exp(-n/n_0)$ as observed in the equilibrium case [47]. The clustering is weak at these size ratios, however, for $S > 5$ the $p(n)$ displays a power-law decay with an exponential cut-off at large n, i.e., it is best described by the equation:

$$p(n)/p(1) \sim 1/n^{\alpha}\, exp(-n/n_0) \tag{3.11}$$

where α is the exponent of power law and n_0 is the cutoff cluster size . The fits of this

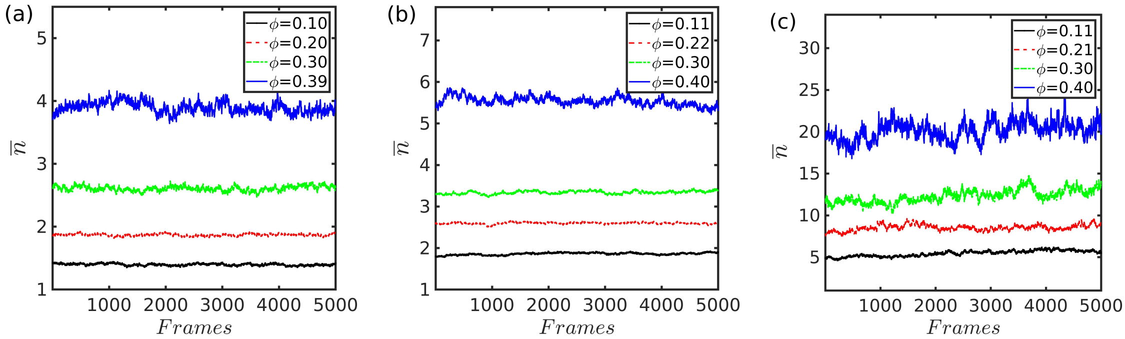

Figure 3.7: Average cluster size $\overline{n}$ for each frames at various area fraction $\phi \sim 0.1 - 0.4$ and the size ratio S, (a) $\overline{n}$ at $S \sim 2.5$. (b) $\overline{n}$ at $S \sim 3.5$. (c) $\overline{n}$ at $S \sim 5.5$.

form to our data are shown in the figure using dashed lines. The value of α varies with the area fraction ϕ of colloids. While the value of n_0 varies with ϕ as well as S. All the values of α and n_0 at various ϕ and S are given in the Table 3.1. These results indicate that the characteristic size of clusters grows with increasing size ratio. The growth of clusters is dramatic at larger area fractions, the inset of Fig. 3.6(a) shows cluster distribution at $\phi \sim 0.3$. When the CSD curves are scaled by the characterstic size of clusters n_0 and the respective exponents of power law α, all the curves fall on the master curve. Fig. 3.6(b) shows the master CSD curves and the black line is the fitted curve.

We further elucidate the clustering of colloids by computing the average cluster size using the expression

$$\langle \overline{n} \rangle = \sum n\, p(n), \tag{3.12}$$

where $\langle ... \rangle$ represents the ensemble average over various configurations and $\overline{n}$ represents the average cluster size for each frame. The values of $\overline{n}$ are presented in Fig. 3.7(a)-(c) for different size ratios $S = 2.5 - 5.5$ at various ϕ respectively. These figures of average cluster size $\overline{n}$ shows that measurements were made in the steady state. Further the ensemble averaged cluster size $\langle \overline{n} \rangle$ is shown in the Fig. 3.8(a) where the curves with different symbols correspond to different area fractions ranging from $\phi \sim 0.1 - 0.4$. What is clear from Fig. 3.8(a) is that increasing the size-ratio or the relative size of colloids leads to larger cluster sizes. This suggests that the effective potential between the colloids becomes stronger with an increasing size ratio.

One can intuitively understand the underlying physics by considering the interaction between an isolated colloidal particle and a swimmer. When the size of a particle is small, bacterium entrains the particle to larger distances before changing its direction of motion. However, when the particle is large, the entrainment distance is small, and the scattering angle of the swimmer is large [81]. It indicates that the bacteria can suppress cluster formation when the colloidal particles are smaller. What is not clear from our experiments is whether larger size-ratios lead to a macroscopic phase separation in our system. To understand this aspect, we turn to numerical simulations that allow a detailed exploration of parameter space.

3.5 Simulation results

3.5.1 Effective potential between a pair of passive particles in active media

We turn to simulations in order to understand the experimental observations. We first investigate the effective potential between a pair of passive particles in active media in our simulations. Consider two passive particles with their positions at $\mathbf{r}_1$ and $\mathbf{r}_2$ in a system of ABPs with $N_a = 1800$, corresponding to an ABP area fraction of $\phi_a = 0.5$. The position of the first particle at $\mathbf{r}_1$ is fixed, while the position of second particle is slowly varied in small steps of $\Delta x = 0.5a_a$ starting from the zero surface to surface distance between two passive particles. The cartoon of the system simulated for the force calculation for a fixed r is shown in top inset of Fig. 3.8(b). The ABPs are shown in red and passive particles in blue for $S = 8$. For resolution, only a part of the system near the two passive particles is shown. The active particles' positions and orientations are updated according to the Eqs. (3.7 and 3.8). For each configuration at a given distance between two passive particles, the system is allowed to reach the steady state. Further, we use the steady state configuration to calculate

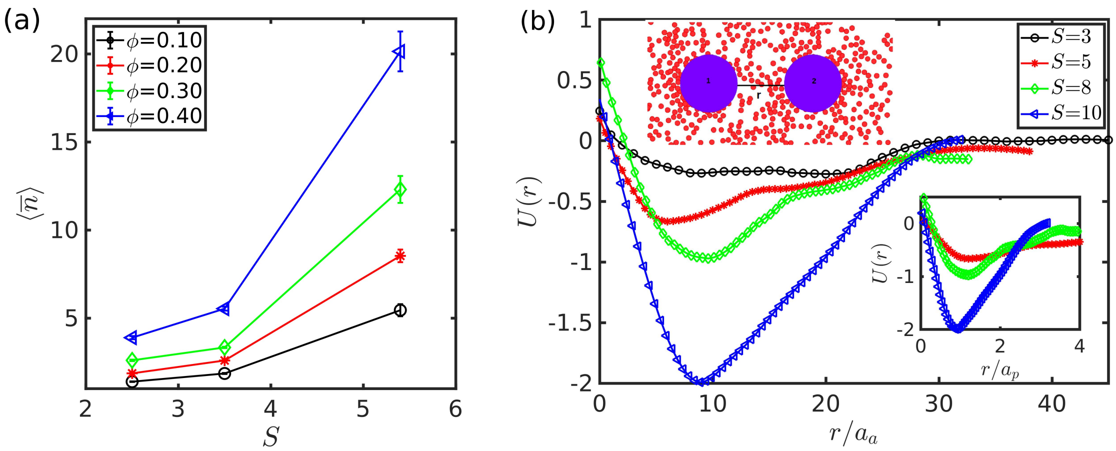

Figure 3.8: (a) The average cluster size $\langle\overline{n}\rangle$ for varying S. The curves with different symbols correspond to different particle densities, ranging from $\phi \sim 0.1 - 0.4$. (b) The effective potential between a pair of colloidal particles. The main panel shows the plot of the effective potential $U(r)$ vs. scaled distance r/a_a for $Pe = 25$ and size-ratios $S = 3,\ 5,\ 8,$ and 10. The top inset shows a snapshot of the part of the system used to calculate the potential. The two bigger particles are passive particles with the left one marked as particle 1 and the right one marked 2 with positions $\mathbf{r}_1$ and $\mathbf{r}_2$, respectively. The red circles are ABPs. The line shows the surface to surface distance r between two passive particle. The bottom inset shows the effective potential with the scaled distance r/a_p.

the effective force $\mathcal{F}^S(r)$ acting on a particle at a surface to surface separation r, such that:

$$\mathcal{F}^S(r) = \mathbf{F}_{12}(r) + \sum_{i=1}^{N_a} \mathbf{F}_{1i}(r) \tag{3.13}$$

Here $\mathbf{F}_{12}(r)$ is the force due to passive particle 2^{nd} on 1^{st}, and $\sum_{i=1}^{N_a} \mathbf{F}_{1i}(r)$ represents the sum of all the forces due to active particles on 1^{st} passive particle for a given configuration of two passive particles at separation r. The potential is then calculated by integrating the force over the distance [119–121] which is given as:

$$U(r) = \int_{-\infty}^{r} \mathcal{F}^S(r)dr \tag{3.14}$$

Here we set the lower limit as one-fourth of the box-length. The results are averaged over 30 independent realizations.

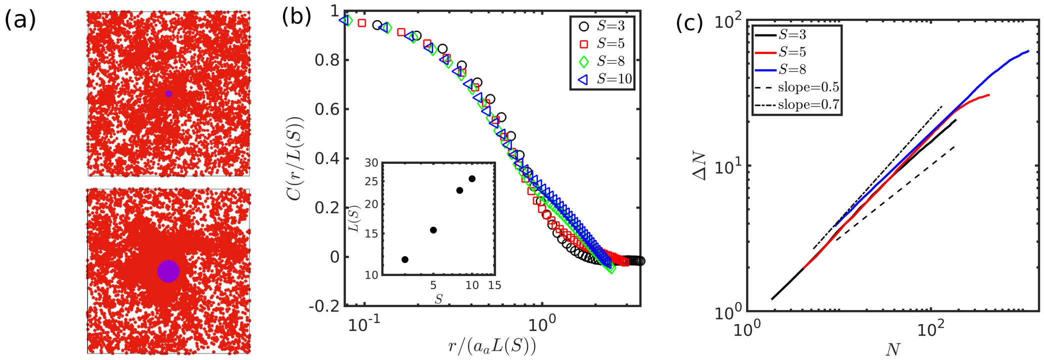

Figure 3.9: (a) The top and bottom panels show instantaneous snapshots of the system for size ratios $S = 3$ and 8, respectively. Many such configurations are used to calculate the density correlations $C(r)$. Red particles are ABP's and blue particle at the center is the bigger passive particle. (b) The main panel shows normalized correlations of density fluctuations $C(r)$ due to a passive particle for various size ratios S. The inset show the length scale extracted from $C(r)$ as function of the size-ratio. The length scale is expressed in terms of active particle size. (c) Number fluctuations of active particles around an isolated passive particle for three sizes S = 3, 5 and 8.

The main panel of Fig. 3.8(b) shows the effective potentials $U(r)$ computed at $Pe = 25$ and four size-ratios $S = 3$, 5, 8 and 10, which are comparable to experimental values. The distance is normalized by the radius of active particles, which is kept fixed to $0.1a_a$. The negative side of the potential shows attraction and the positive nature is repulsion. For all the parameters the potential approaches zero at large distances, and it is negative at intermediate distances. The depth of the potential becomes deeper with increasing S. The inset shows the effective potential with the distance r scaled by the size of passive particles. Surprisingly, the minima of the potentials for the size ratios $S = 5$, 8 and 10 fall at $r/a_p = 1$, which implies that the length scale characterizing the range of the interaction potential is set by the size of passive particles.

3.5.2 Density fluctuations of active particles

The interactions between passive particle in simulations are primarily mediated by active particles. Naturally, their density fluctuations will influence the effective potential between passive particles. This notion is reminiscent of the role that concentration fluctuations play in the origin of critical Casimir forces in a binary mixture [111,122] and the density fluctuations

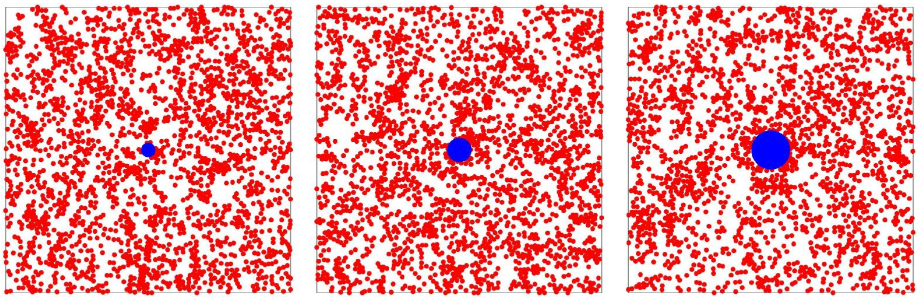

Figure 3.10: Clustering of active particles in the presence of single passive particles at the center. Snapshots of the system for ABPs packing fraction $\phi_a = 0.3$, for different size ratio S=3, 5 and 8, from left to right, respectively. The active particles are colored red and centered blue particle is passive particle.

of depletant that are responsible for depletion forces in colloid-polymer mixture [102, 103]. To highlight these aspects in our simulations, we consider a single passive particle in a system of ABPs. An instantaneous snapshot of the active particles and a passive particle is shown in the top and bottom panels of Fig. 3.9(a) for size ratios $S = 3$ and 8, respectively. The active particles cluster around the passive particle, and this clustering is enhanced for larger size ratios. This effect is elucidated by computing the time averaged density correlation of active particles.

$$C(r) = (\langle\rho(0)\rho(r)\rangle - \langle\rho(r)\rangle^2)/(\langle\rho(r)^2\rangle - \langle\rho(r)\rangle^2) \tag{3.15}$$

The correlations are calculated by considering circular bins of width $dr = 0.5a_a$ around the particle center, starting from its surface. So, $\rho(0)$ is the average particle density in the first bin from the surface of the particle and $\rho(r)$ is the average particle density in a bin at a distance r from the surface with an area $2\pi r dr$. The scaled correlations $C(r/L(S))$ corresponding to size ratios $S = 3, 5, 8$ and 10 are shown in Fig. 3.9(b). It is evident that the correlations shows a good scaling with respect to the correlation length $L(S)$. The inset of Fig. 3.9(b) shows a correlation length $L(S)$ extracted from $C(r)$ to characterize the typical size of clusters, $L(S)$ is measured in terms of size of ABP. Clearly, $L(S)$ increases linearly with S. Apparently, increasing the size-ratio leads to a larger number of active particles interacting with a passive particle, so it promotes bigger clusters. Since the correlation $C(r)$ scales with $L(S)$, the relative size of passive particle determines the density correlation of ABPs. These results strongly suggest that larger passive particles interact over longer distances due to enhanced density correlations of active particles.

The number fluctuation is defined as:

$$\Delta N = \sqrt{\langle \Delta N^2 \rangle} = \sqrt{\langle N^2 \rangle - \langle N \rangle^2} \tag{3.16}$$

The examination of number fluctuations ΔN of active particles around an isolated passive particle yields similar conclusions. It is computed considering an annular disc with inner radius equal to the radius of the passive particle and outer radius is varied. The mean and variance of number of ABP's are calculated for different outer radius of the disc. The same is repeated for three different sizes of the passive particle or for three different size ratios $S = 3$, 5 and 8. In the Fig. 3.9(c), we show the plot of ΔN *vs.* average N for three sizes $S = 3$, 5 and 8. In all cases, the graph follows a power law, $\Delta N \sim N^{\alpha}$, where $\alpha = 0.5$ for thermal fluctuations and $\alpha > 0.5$ for Giant Number Fluctuations (GNF). For moderate values of N, this relationship holds across all S, but deviations occur as N increases. These deviations appears at relatively larger N as the size ratio increases. Hence increasing the size of passive particle increases the stretch of density fluctuation of ABP's. These results establish that increasing the size ratio leads to longer density correlations that play a central role in the emergence of long-range effective potential between passive particles in our simulations.

The above results of numerical simulation were obtained at a packing density of $\phi_a = 0.5$ of ABPs. Keeping in mind that experiments are performed at lower packing densities of bacteria, we present the snapshots of the configuration of ABPs around a single passive particle for a lower packing fractions of $\phi_a = 0.3$ in Fig. 3.10. The corresponding videos S2 and S3 for S= 3 and 8 are provided as supplementary material [123]. The snapshots and videos suggest that the density correlation of ABP's increase with increasing size ratio S at lower packing fractions as well. And the density fluctuations of active particles observed in

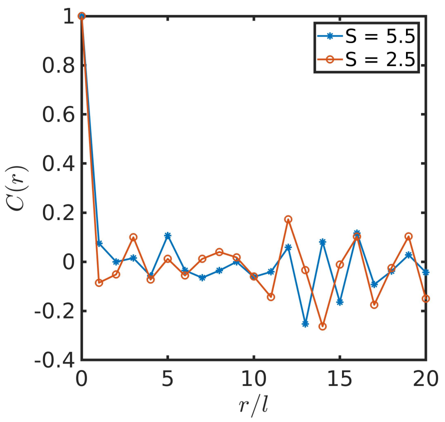

Figure 3.11: The correlations of density fluctuations $C(r)$ of bacteria in experiments. It is shown for two different size ratios $S \sim 2.5$ and 5.5 of a colloidal particle. The x-axis is scaled by the size of the bacteria l.

Fig. 3.9(c) persist even at lower packing densities.

A similar analysis of the time averaged density correlations $C(r)$ of bacteria in experiments, which is computed for bacteria around an isolated colloidal particle in experiments, are shown in Fig. 3.11 for size ratios S=2.5 and 5.5, and they reveal that the density correlations are suppressed in our experiments. In addition to activity, the interactions between colloidal particles are mediated by hydrodynamics due to the presence of fluid medium. Earlier studies of active-passive matter have shown that hydrodynamic interactions play an important role in promoting clustering [124, 125]. However, a comprehensive understanding of these aspects would necessitate further investigations that are deferred for future work.

3.5.3 Phase behaviour of active-passive mixture

We elucidate the effect of the above effective potential on the full microscopic simulations of active-passive mixture performed using the Eqs. (3.7-3.9). We simulated the system for $Pe = 25$ and size ratio $S = 3, 5$ and 8, which are close to experimental values. In the Fig. 3.12, the steady state snapshots of passive (blue, bigger) and active (red, smaller) are shown for different size ratios $S = 3$, 5 and 8 from left to right, respectively. Clusters with moderate to strong ordering are found on increasing S. For small $S = 3$, clusters are present but without strong local hexagonal ordering. As we increase S, the ordering and clustering

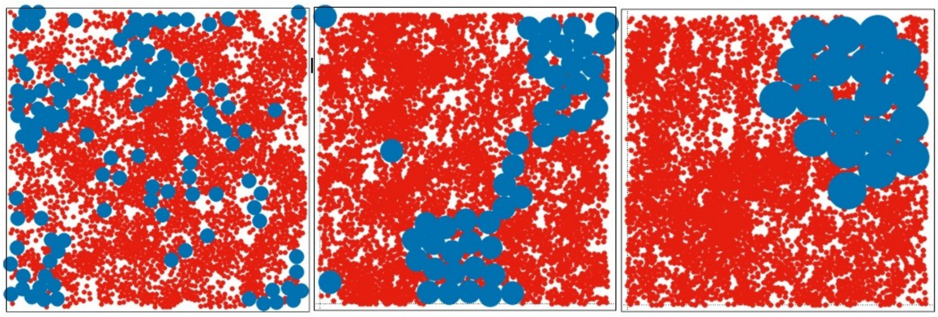

Figure 3.12: Snapshots of the system obtained from the microscopic simulation: two types of particles for different size ratio $S = 3, 5$ and 8 (left, central and right columns) at $Pe = 25$. Red particles are ABPs and blue particles are passive particles, for fixed packing fraction $\phi = 0.60$ in a system of size $l_{box} = 140a_a$.

is enhanced. We also calculated the percent of passive particles participating in the largest cluster for different size ratios and it increases from 35% to 67% as we increase size from 3 to 8 (data not shown). Hence for large size ratio passive particles show the macroscopic phase separation.

3.6 Conclusion

In summary, we have shown that the phase behavior of passive particles in active media is determined by the interplay of activity and the attractive effective potential of interaction. Our study establishes that the size-ratio of passive to active particles provides a convenient way of tuning the effective potential to manipulate the nonequilibrium assembly of passive particles. When the size-ratio is large, the effective potential is strong enough to lead to macroscopic phase-separation of passive particles. Furthermore, our simulations have demonstrated that density fluctuations (correlations) of active particles play a key role in the origin of stronger effective potentials as the size-ratio increases.

The colloidal particles in our experiments display dynamic clustering. However, the average size of clusters were observed to grow on increasing the size-ratio (Fig. 3.8(a)). This is because when the size of the colloidal particles is similar to that of bacteria, the clusters are disturbed easily by the bacteria. In contrast, the clusters of larger particles are relatively more stable. To understand these aspects in a better way, we performed simulations using a mixture of ABPs and passive particles. The effective potential between a pair of passive particles in active media was found to be attractive and dependent on the size-ratio (Fig. 3.8(b)). Increasing the size-ratio made the effective potential stronger and long-ranged. Further, our study suggests that the long-ranged interactions originate from enhanced density fluctuations of active particle around a passive particles. As the interactions of passive particles in our simulations are mediated by active particles, the density fluctuations of active particles have considerable influence on the nature of effective interactions between passive particles. The recent studies of colloid-bacteria mixture had concluded that the torque on active particle stabilizes the passive colloidal clusters [68]. Here, we provide an alternate view of the phenomenon based on effective potential that is intimately tied to density fluctuations of active particles.

The full simulations of active-passive mixtures showed that when the size-ratio is small, the passive particles form dynamic clusters. However, when the size-ratio is large, the effective interactions become strong enough to cause phase separation of colloidal particles. Even though our system displays many similarities with equilibrium mixture of colloid-polymer, the underlying physics is strongly out of equilibrium. The simulations in our study have ignored the effect of hydrodynamic interactions. In experiments, the interactions between colloids are mediated by activity and hydrodynamics interactions. Exploring these aspects in detail will lead to a comprehensive understanding of active-passive mixtures.

Chapter 4

Kinetics of the Phase Ordering of Colloids in Active Liquids

Colloidal particles exhibit dynamic clustering and persistent rotations in chiral active liquids of E. coli. Their assembly displays several features that are not found in equilibrium systems. Here, we investigate the coarsening of colloidal particles, highlighting the novel features of ordering in systems with strong fluctuations. A homogeneous mixture of colloids and swimmers is unstable, so the colloids spontaneously phase separates to form dynamic clusters. The spatial correlation function of the order parameter exhibits dynamic scaling, and the system displays non-Porod behaviour indicating domains featuring diffuse interfaces. The correlation function reveals a cusp singularity that is associated with an exponent α. Furthermore, the power-law exponent θ of the cluster size distribution and the cusp exponent follow a relation $\theta + \alpha = 2$, which has been established in several systems with fluctuation dominated phase ordering. The coarsening length-scale in our experiments grows as $L \sim t^{1/4}$, which demonstrates a strong deviation from the Lifshitz-Slyozov law. All these features point to a novel phase ordering of colloids in chiral active liquids.

4.1 Introduction

Homogeneous binary mixtures that are thermodynamically stable at high temperatures become unstable when cooled below the coexistence curve. This instability leads to formation of domains of ordered phases that grow and eventually result in a stable, phase-separated state [126, 127]. This fascinating phenomenon of phase separation is pervasive in nature and has attracted considerable attention due to its relevance across various fields, including physics, materials science, biology, and everyday life. For example, phase separation can be seen in the separation of vinegar and oil in the kitchen, the formation of alloys in materials science [128, 129], and the creation of membraneless organelles formed by protein condensates in cells [130, 131].

Some well-understood aspects of phase separation include the coarsening or ordering kinetics and the interfacial structure of the domains that separate different phases. The phase ordering that occurs after quenching is not instantaneous; instead, the length scale of the ordered regions gradually increases over time, starting from an initially disordered state. The timescales for complete phase separation in the thermodynamic limit can be exceedingly large, as the largest relaxation time diverges with system size in the ordered phase. Interestingly, the morphology of the coarsening pattern remains similar as the domains evolves in time, indicating dynamic scaling of the domains. In systems with a conserved order parameter, where hydrodynamic effects are absent, the characteristic size of the domains grows according to the Lifshitz-Slyozov law, which scales as $t^{1/3}$ [126, 127]. The interfaces between the phases are sharp, leading to a singularity in the correlation function of the order parameter at short distances. The underlying physics of this phenomenon is well described by continuum models where the free energy function is considered to be a quartic polynomial in the order parameter with square gradient terms [126, 127]. These models are also known as Cahn-Hilliard equation or Model B in the athermal limit.

In recent years, active systems of self-propelled particles have been shown to undergo a novel type of phase transition known as motility-induced phase separation (MIPS) [46]

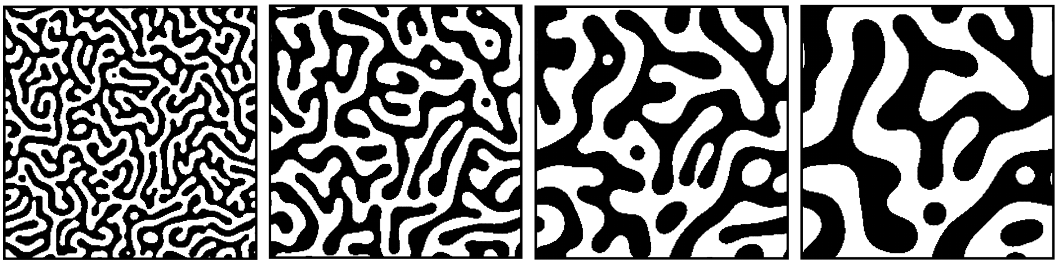

Figure 4.1: Snapshots depict the evolution of a homogeneous binary (AB) mixture, which has been quenched below the coexistence curve at time $t = 0$. The sequence illustrates the spinodal decomposition process at different times $t = 100$, 500, 2000, and 5000 (from left to right). The two shades in the images represent the distinct phases formed during the decomposition process. Image adapted from [127].

with certain characteristics similar to those of conventional phase separation. It manifests beyond a critical density of particles due to their persistent motion. Tailleur and Cates [46] demonstrated that particles with propulsion velocities that decrease as local particle density increases, such as due to interparticle collisions, are generically prone to phase separation. This reduction in velocity leads to the accumulation of particles, which in turn further decreases their speed, creating a positive feedback loop. The theory was in fact motivated by observations made in earlier simulations of active Brownian particles (ABP) [47, 48] and experiments with active Janus colloids [45, 132]. In particular, the simulations of Redner et al. [48] reveal that the cluster growth in the coarsening regime deviates from the conventional $t^{1/3}$ growth in systems approaching equilibrium. Further theoretical efforts have led to continuum models of phase separation that are relevant to active systems. They are referred to as to active model B [133]. We present a brief overview of these models and a detailed discussion of our experimental results in the following paragraphs.

4.2 Coarsening and phase ordering:

Phase separation within the classical thermodynamic framework is a transient, non-equilibrium process where an initially homogeneous equilibrium state transitions into a demixed equilibrium state due to changes in thermodynamic conditions. When a binary liquid mixture is rapidly cooled from a uniform state to demixed state, it undergoes phase separation resulting in distinct ordered phases. During this transition, domains of the two equilibrium phases form, expand, and gradually coarsen over time. The formation of these domains can proceed via two primary mechanisms: nucleation and growth, or spinodal decomposition. Although these mechanisms differ in their initiation, both routes result in the qualitatively similar coarsening patterns during the late stages of growth. In the later stages of domain growth, a dynamical scaling regime emerges, characterized by self-similarity of domain morphologies over time, up to an overall coarsening length. This means that while domains continue to evolve and grow in size, their overall structure remains statistically similar over time, exhibiting scaling behavior independent of the specific details of the phase separation mechanism. Figure 4.1 shows a series of snapshots depicting the evolution of a homogeneous binary (AB) mixture that has been quenched below the coexistence curve at time $t = 0$, illustrating spinodal decomposition and the self-similar behavior of domain growth over different times [127].

4.2.1 Scaling hypothesis

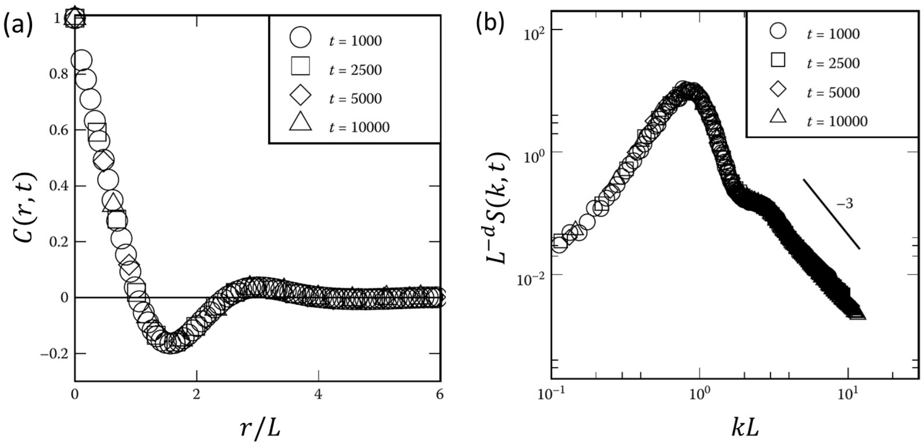

Figure 4.2: (a) The scaled spatial correlation function $C(r,t)$ is plotted as a function of r/L at various time points. (b) The corresponding scaled structure factor $L^{-d}S(k,t)$ is presented as a function of kL, reflecting the data shown in (a). Image taken from: [127].

After domain formation, as time progresses, the domain pattern expands with a characteristic length scale $L(t)$ that follows a power-law relation with time:

$$L(t) \sim t^n$$

Here, the growth exponent n varies depending on the specific dynamics governing the system. According to the scaling hypothesis, during the later stages of evolution, there exists a single characteristic length scale $L(t)$, such that when all lengths are scaled by $L(t)$, the domain structure becomes statistically time-independent. Two commonly employed measures for analyzing domain structure are the equal-time spatial correlation function $C(\mathbf{r}, t)$ and its Fourier transform, the equal-time structure factor $S(\mathbf{k}, t)$, defined as follows:.

$$\begin{aligned} C(\mathbf{r}, t) &= \langle \phi(\mathbf{x} + \mathbf{r}, t)\phi(\mathbf{x}, t) \rangle \\ S(\mathbf{k}, t) &= \langle \phi_{\mathbf{k}}\ \phi_{-\mathbf{k}} \rangle \end{aligned}$$

The presence of a single characteristic length scale $L(t)$ suggests that both the spatial correlation function $C(\mathbf{r}, t)$ and the structure factor $S(\mathbf{k}, t)$ can be expressed in scaling forms as follows:

$$C(\mathbf{r}, t) = f\left(\frac{\mathbf{r}}{L(t)}\right) \tag{4.1}$$

$$S(\mathbf{k}, t) = L^d g(kL(t)) \tag{4.2}$$

where, d denotes the dimensionality of the system, and $g(x)$ represents the Fourier transform of $f(y)$. The scaled spatial correlation function and scaled structure factor for the binary (AB) mixture are depicted in Fig. 4.2(a) and 4.2(b) [127].

4.3 Phase separation kinetics: Model B

The kinetics of phase separation are often described using dynamic field theories that utilize a conserved scalar order parameter, typically represented by ϕ. A standard approach involves simplifying the free energy into a quadratic polynomial in ϕ, including a square gradient term, and assuming local diffusive dynamics. This leads to a theoretical formulation known as Model B, which is crucial for understanding phase separation processes under time-reversal symmetry. When stochastic noise is incorporated into Model B, it extends into the Cahn-Hilliard-Cook equation. To achieve a continuum description with a coarse-grained order parameter field $\phi(\mathbf{r}, t)$, a Ginzburg-Landau free energy functional is utilized to characterize the ordered phase [134].

$$\mathcal{F}[\phi] = \int \left(\frac{a}{2}\phi^2 + \frac{b}{4}\phi^4 + \frac{K}{2}|\boldsymbol{\nabla}\phi|^2 \right) d\mathbf{r} \tag{4.3}$$

where the parameter a in the equation is temperature-dependent, $a \sim a(T - T_C)$, whereas $b > 0$ is constant parameter and $K > 0$ is related to the interfacial tension between A-rich and B-rich domains. In the presence of a conserved order parameter with local diffusive dynamics, the equation of motion becomes [126, 134]:

$$\frac{\partial \phi}{\partial t} = \nabla^2 \frac{\delta \mathcal{F}}{\delta \phi} \tag{4.4}$$

In binary liquid or alloy systems, the exchange between A-type and B-type molecules is restricted to local interactions, preventing long-distance exchanges and leading to a diffusive transport of the order parameter. This process can be described by a continuity equation, which is the standard formulation of Model B, as shown in Eq. 4.4:

$$\partial_t \phi = -\boldsymbol{\nabla} \cdot \boldsymbol{J} \tag{4.5}$$

$$\boldsymbol{J} = -M\boldsymbol{\nabla}\mu + \sqrt{2Mk_BT}\,\boldsymbol{\Lambda} \tag{4.6}$$

$$\mu = \frac{\delta \mathcal{F}}{\delta \phi} = a\phi + b\phi^3 - K\nabla^2\phi \tag{4.7}$$

where, M represents mobility, $\boldsymbol{\Lambda}$ stands for Gaussian white noise, and μ denotes chemical potential [134]. Model-B serves as a descriptive framework for understanding phase separation in equilibrium systems such as binary alloys, polymer blends and binary liquids. This operates within the regime where the transport of the order parameter is primarily driven by the Lifshitz-Slyzov mechanism. This mechanism is characterized by the evaporation of molecules from regions with high interfacial curvature and their condensation onto regions with lower curvature, occurring before hydrodynamic effects become significant [135]. To explore the phase diagram of Model B, consider a mixture of A-type and B-type molecules. A coarse-grained order parameter $\phi(\mathbf{r})$ can be defined, where $\phi = 0$ represents regions with equal mixing of A and B molecules, and $\phi = \pm\phi_b$ corresponds to A-rich and B-rich regions, respectively, with ϕ_b being a non-zero constant. The associated free energy density is then given by:

$$f(\phi) = \frac{a}{2}\phi^2 + \frac{b}{4}\phi^4 + \frac{K}{2}|\boldsymbol{\nabla}\phi|^2$$

The behavior of the system is determined by the sign of $a(T - T_C)$, leading to two distinct scenarios. If $a > 0$, the function $f(\phi)$ has a single minimum at $\phi = 0$, indicating that the system remains uniformly mixed without undergoing phase separation. Conversely, if $a < 0$, the function $f(\phi)$ develops a double well with minima at the binodal points $\pm\phi_b$. In this case, the free energy of the homogeneous state is higher than that of the phase-separated state. As a result, the system minimizes its free energy by separating into two distinct phases: a dilute phase with a density of $-\phi_b$ (rich in component A) and a dense phase with a density of $+\phi_b$ (rich in component B). This is graphically depicted in Fig. 4.3(a), which shows the free energy density $f(\phi)$ as a function of the relative concentration ϕ.

Figure 4.3(b) illustrates the schematic phase diagram for Model-B, showing the relation between temperature (T) and relative concentration (ϕ). In this model, temperature is integrated via the noise term. The boundary separating the mixed and demixed states is referred to as the binodal curve, while the spinodal curve marks the set of inflection points within the diagram. When the system crosses the phase boundary at a critical point, it undergoes a second-order phase transition, where the mixed phase becomes globally unstable, leading to phase separation via spinodal decomposition. This process results in the formation of bicontinuous domains rich in A and B molecules. On the other hand, crossing the phase boundary

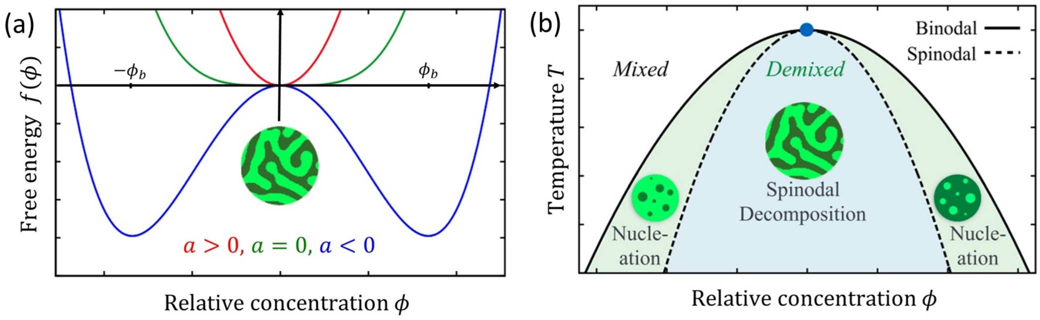

Figure 4.3: Thermodynamics of phase separation:(a) the free energy function may exhibit different forms, such as a single minimum for a homogeneous phase or a double well for phase-separated states, (b) the phase diagram of binary systems with regions of mixed and demixed phase stability: The binodal boundary marks the limits of phase coexistence, while the spinodal boundary delineates the region where the mixed phase becomes unstable and spontaneous phase separation occurs. The critical point, indicated by a blue dot, represents the conditions under which the distinction between phases disappears, Figure adapted from [136].

away from the critical point triggers a first-order phase transition, where phase separation occurs between the binodal and spinodal curves. In this case, droplets of the minority phase nucleate, grow, and coarsen until the system reaches its demixed equilibrium state [136].

4.3.1 Interfaces and Interfacial tension

In systems undergoing phase ordering, sharp interfaces are regarded as topological defects for the scalar order parameter. These defects manifest in two forms: kink and antikink. The kink - antikink solutions are obtained by minimizing the free energy $\mathcal{F}$ under appropriate boundary conditions [127, 134] and give as:.

$$\phi(x) = \pm \tanh\left[\frac{x - x_0}{\xi_{eq}}\right] \tag{4.8}$$

Here, ξ_{eq} is the interfacial width, x denotes the coordinate normal to the interface, and x_0 is the midpoint of the interface. Fig. 4.4(a) depicts the form of the topological defect with a positive sign (kink) and Fig. 4.4(b) with a negative sign (antikink). In the kink configuration, ϕ transitions from -1 at $x = -\infty$ to $+1$ at $x = +\infty$, while in the antikink configuration, the

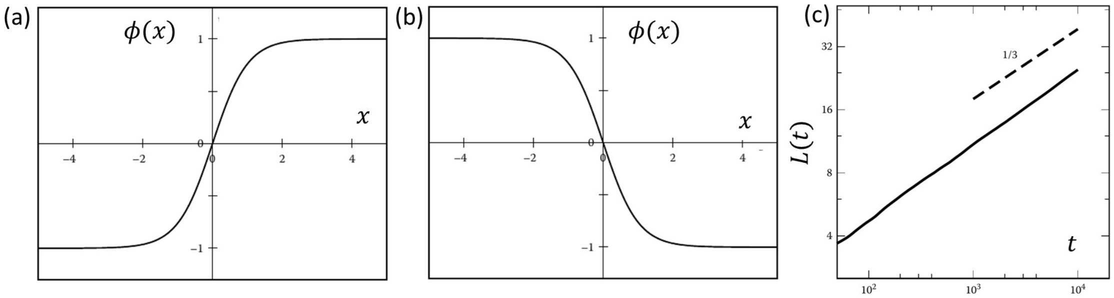

Figure 4.4: Order parameter variation [$\phi(x)$ versus x] for (a) the static kink profile and (b) the static anti-kink profile.(c) The dynamic length scale $L(t)$ with respect to time t showing $L(t) \sim t^{1/3}$ growth law. Image source: [127].

transition occurs in the opposite manner.

The interfacical tension is a crucial quantity in the phase separation and it quantifies the energy required to create and maintain the interface between these phases. It can be defined as the excess of free energy per unit area of a flat interface and given as [127, 134]:

$$\sigma_{eq} = \sqrt{\frac{-8Ka^3}{9b^2}} \tag{4.9}$$

In equilibrium, the interfacial tension sets many physical quantities such as Laplace pressure. Which refers to the pressure difference across the interfaces between two phases such as liquid-vapour and given as.

$$\Delta p = \frac{(d-1)\sigma_{eq}}{R} \tag{4.10}$$

where d is the dimensinality of the system and R in the radius of curvature of the interface. Laplace pressure is inversely proportional to the R. this means the pressure inside a curved surface is higher than the pressure outside.

4.3.2 Ostwald ripening: Diffusion-limited growth

Ostwald ripening occurs in systems where small droplets of a minority phase are dispersed within a majority phase. Due to differences in chemical potential, smaller droplets have higher surface energy per unit area than larger ones. As a result, material flows from the smaller droplets to the larger ones, causing the smaller droplets to shrink while the larger ones grow. This process reduces the overall surface area of the dispersed phase, thereby minimizing the system's free energy. The Laplace pressure contributes in driving this mass transfer, as the higher curvature of smaller droplets results in greater internal pressure compared to larger droplets. This pressure difference promotes material flow from smaller to larger droplets. To analyze the dynamics of the largest droplet during Ostwald ripening, consider a phase-separated system with two droplets of radii R_1 and R_2, where $R_1 > R_2$. The growth dynamics of the larger droplet, with radius R_1, can be described by the following equation:

$$\dot{R} = \frac{\beta}{R\Delta\phi}\left[\frac{1}{R_2} - \frac{1}{R_1}\right] \tag{4.11}$$

Here, $\Delta\phi$ represents the difference in density between the two binodals, and β is the Ostwald ripening rate.

4.3.3 Lifshitz-Slyzov law: Dynamic length scale

The Lifshitz-Slyozov law describes the kinetics of Ostwald ripening during phase separation, where larger droplets grow at the expense of smaller ones. Over time, the average size of the dispersed droplets follows a power-law relation, specifically $L(t) \sim t^{1/3}$, as depicted in Fig. 4.4(c). In systems with a conserved order parameter, the movement of interfaces between different phases occurs through the transport of material across the bulk phases. The chemical potential μ at the surface of a domain of size L is given by $\mu \sim \frac{\sigma}{L}$, where σ is the surface tension. Considering the concentration current as $D|\nabla\mu|$, where D is the diffusion constant and $|\nabla\mu|$ represents the gradient of the chemical potential, which scales as $|\nabla\mu| \propto \sigma/L^2$, the concentration current becomes $D|\nabla\mu| \propto D\sigma/L^2$. Since the rate of change in domain size dL/dt is governed by the diffusion of material across domain boundaries, we have $dL/dt \propto D|\nabla\mu|$, leading to the relationship:

$$dL/dt \sim D\sigma/L^2 \implies L(t) \sim (D\sigma t)^{1/3}$$

4.3.4 Porod's law: Sharp interfacial structure scattering

In phase-ordering systems, the existence of sharp interfaces significantly impacts the short-distance behavior of the spatial correlation function $C(\mathbf{r}, t)$ and the large wave vector behavior of the structure factor $S(\mathbf{k}, t)$. To illustrate this, consider a kink defect of size L, with a distance r from the defect core such that $\xi_{eq} \ll r \ll L$. Here, r must be much larger than the equilibrium correlation length ξ_{eq} for the field to be saturated, and much smaller than L for the defect field to be largely unaffected by other defects. When considering points $\mathbf{x}$ and $\mathbf{x} + \mathbf{r}$ within this range, the product $\phi(\mathbf{x})\phi(\mathbf{x} + \mathbf{r})$ will be -1 if a domain wall lies between them and +1 if no wall is present. Consequently, $C(\mathbf{r}, t)$ represents the probability that a randomly placed rod of length r intersects a domain wall:

$$C(\mathbf{r}, t) \approx (-1)\frac{r}{L} + (+1)\left(1 - \frac{r}{L}\right) = 1 - \frac{2r}{L}$$

The non-analytic behavior of this equation at $\mathbf{r} = 0$ is captured by the scaling variable x. The large field gradients near defects cause non-analytic behavior at $x = 0$ in the scaling function $f(x)$ of the pair correlation. This non-analyticity implies a power-law tail in the structure factor, which can be derived by considering the scaling of powers:

$$S(k) \sim \frac{L^d}{(kL)^{d+1}} \tag{4.12}$$

This result is universally recognized as Porod's law.

4.4 Active model B

Active materials are characterized by their violation of microscopic time-reversal symmetry (TRS), as their constituent particles continuously convert energy from fuel into motion. Traditional models that assume TRS are inadequate to describe the phase separation dynamics in such systems. To account for this, an additional term that breaks detailed balance is necessary, with the simplest option being a non-integrable gradient term. This modification, combined with the standard field theory for locally diffusive phase separation, is referred to as Active Model-B (AMB). In AMB, the chosen gradient term breaks detailed balance, meaning that this model cannot be derived from any free energy functional. As a result, AMB represents a new class of models where the breaking of TRS is closely tied to the behavior of interfaces. For a conserved scalar order parameter field $\phi(\mathbf{r}, t)$ at position $\mathbf{r}$ and time t, the equation of motion is given by [133]:

$$\partial_t \phi = -\boldsymbol{\nabla} \cdot \boldsymbol{J}, \tag{4.13}$$

$$\boldsymbol{J} = -\boldsymbol{\nabla} \mu + \boldsymbol{\Lambda}, \tag{4.14}$$

$$\mu = \mu_0 + \mu_1 = -\phi + \phi^3 - \nabla^2 \phi + \lambda (\nabla \phi)^2. \tag{4.15}$$

In this framework, all quantities are dimensionless and normalized using natural units, consistent with the variables defined in Model B. The chemical potential μ is sum of bulk and gradient contributions. The bulk component is $\mu_0 = -\phi + \phi^3$, while the gradient component, μ_1, is further divided into two terms: μ_1^P and μ_1^A. The first term, $\mu_1^P = \nabla^2 \phi$, represents an integrable contribution that can be derived as a functional derivative of some free energy functional $\int f_1 \, d^d r$. However, the second term, $\mu_1^A = \lambda (\nabla \phi)^2$, is an active contribution that cannot be expressed in terms of a free energy functional. In this non-integrable term, the constant λ acts as the activity parameter.

The square gradient term in the chemical potential introduces subtle changes in the coarsening dynamics but has a significant impact on the phase diagram by causing a pressure jump across flat interfaces. Figures 4.5(a)-(b) illustrate the dynamics of Active Model-B (AMB) for both symmetric ($\phi_0 = 0$) and asymmetric ($\phi_0 = -0.4$) quenches in 2D, across different values of $\lambda = 0, -1, -2$, where a uniform initial state evolves over time. For symmetric quenches, the λ term breaks the $\phi \to -\phi$ symmetry, leading to the formation of droplets rather than bi-continuous domain structures, which is characteristic of a slightly asymmetric quench. Previous research by Wittkowski et al. [133] demonstrated that the characteristic domain size follows a power law growth $L(t) \sim t^z$, with the exponent z showing slower

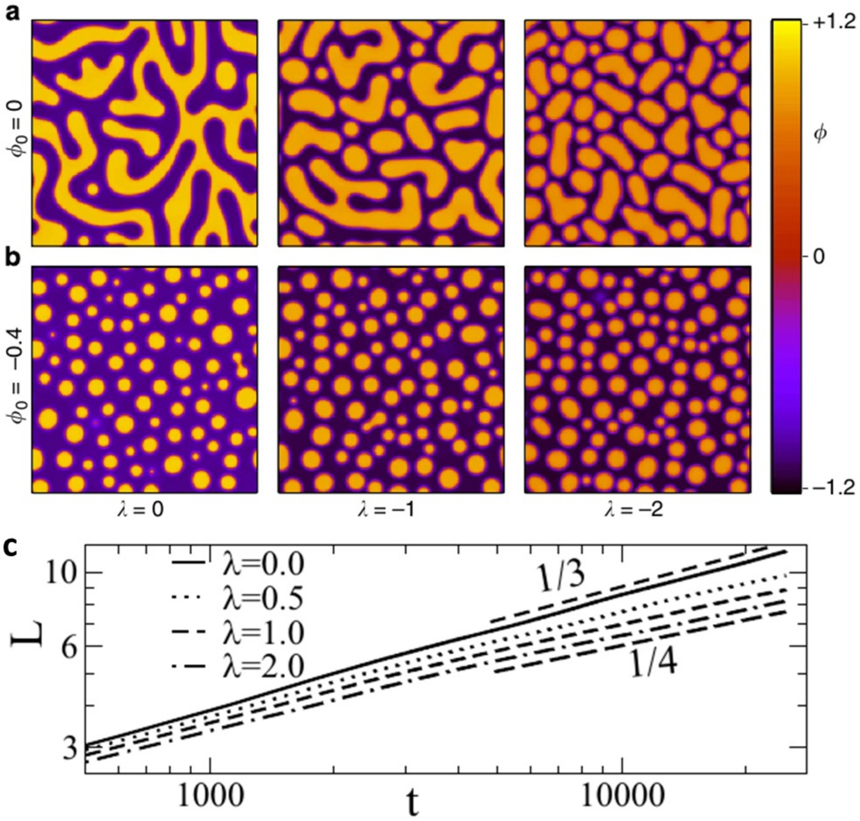

Figure 4.5: (a) Evolution snapshots of domain structures for $\lambda = 0,\ -1,\ -2$ in symmetric ($\phi_0 = 0$) and (b) asymmetric ($\phi_0 = -0.4$) quenches, adapted from [133]. (c) Time evolution of the dynamic length scale L, showing the crossover of the exponent α from 1/3 to 1/4, image sourced from [137].

asymptotic growth as $|\lambda|$ increases, though the exact value of the slower exponent z was not definitively established. Building on this, Pattanayak et al. [137] conducted a similar study, showing that the growth exponent z transitions from $1/3$ at early times to $1/4$ at later stages, depending on the value of λ. The crossover time, t_c, was found to decrease as a power law with the activity strength, following the relation $t_c \sim \lambda^{-3/2}$. This crossover in the growth exponent is depicted in Fig. 4.5(c).

Although a domain growth law described by $L \sim t^{1/4}$ has been suggested for systems where phase separation mainly occurs through surface diffusion rather than bulk diffusion [138], it is clear that surface diffusion does not play a significant role in the observed crossover in the AMB, especially considering the non-connected droplet morphology.

4.5 Fluctuation dominated phase ordering (FDPO)

In the previous sections, we presented phase separation in active matter systems. We next consider nonequilibrium models consisting of hard-core sliding down a fluctuating surface. Das, Barma and coworkers [139, 140] have pioneered these studies using lattice models. These system displays a unique type of phase ordering known as fluctuation-dominated phase ordering (FDPO), in which there are large fluctuations of the order parameter that do not diminish even in the thermodynamic limit. Because of fluctuations, the state is characterized by long-range order of variable magnitude.

FDPO is identified by two key characteristics. Firstly, the order parameter distribution remains broad even as the system reaches the thermodynamic limit. Secondly, the scaling function of the two-point density-density correlation function exhibits a cusp singularity, which is influenced by spacing relative to the system size (in the steady state) or by coarsening length (during coarsening). FDPO was initially observed in a system of passively sliding particles on a fluctuating surface. Since its discovery, it has been identified in various other nonequilibrium systems [141, 142] and in an equilibrium Ising model with long-range interactions [140, 143].

4.5.1 Broad distribution of the order parameter

In a typical two-phase ordering system, a large finite system in a steady state predominantly resides in one phase before transitioning to the other. In the context of an Ising ferromagnet with non-conserved dynamics, where s_j represents the spin at site j, the order parameter $m = \frac{1}{L}\sum_{j=1}^{L} s_j$ is defined. The probability distribution of m, Prob(m), exhibits a prominent peak at either m_s or $-m_s$, with infrequent transitions between these values as shown in the left of Fig. 4.6(a). As the system approaches the thermodynamic limit ($L \to \infty$), the peak widths around $\pm m_s$ converge to zero.

In contrast, the FDPO steady state is characterized by substantial fluctuations while main-

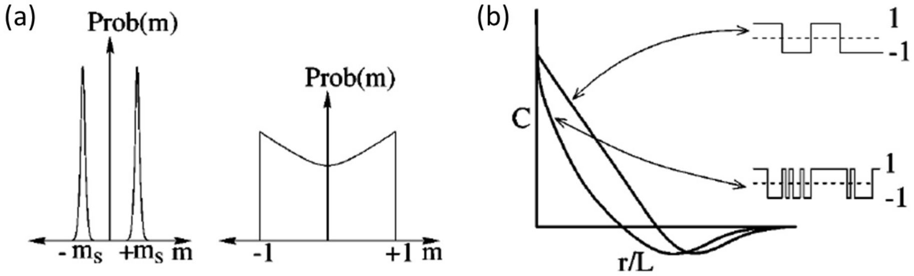

Figure 4.6: (a) Schematic depiction of Prob(m) against m in steady state for non-conserved order parameter left: a normal phase ordering system, and right: a system showing FDPO. Image taken from [140]. (b) Schematic depiction of a linear decay and a cuspy decay of $C(r)$ as a function of r/L, characteristic of normal phase ordering and FDPO. Image adapted from [140].

taining macroscopic order, with the order parameter displaying significant variation in time. As a result, the order parameter distribution remains broad, as illustrated on the right side of Fig. 4.6(a). The limiting distribution Prob(m) does not narrow but instead remains spread over a broad range of m, even in the thermodynamic limit.

When the order parameter is conserved, the magnetization stays constant and identical in both the ordered and disordered phases. As a result, it's necessary to identify a quantity that can effectively distinguish between order and disorder. And these distinguishing quantities are the long-wavelength Fourier modes, $Q_n = \frac{1}{L}\sum_{j=1}^{L}|e^{iqj}(1+s_j)/2|$, with $q = \frac{2\pi n}{L}$, where n is an integer. In such a phase separated state in equilibrium, the first Fourier mode Q_1 serves as a suitable order parameter, exhibiting a sharply peaked probability distribution at a single value. However, in states exhibiting FDPO, a single Fourier mode is insufficient to fully characterize the order. Instead, multiple order parameters are required to adequately describe the system's behavior under FDPO. The multiple order parameter relates to interesting 'make and break' aspect of the FDPO cluster dynamics in study state. The largest cluster that forms is macroscopic in size and it is highly dynamic and occasionally fragments into smaller macroscopic clusters, causing Fourier modes other than $n = 1$ to become significant and pick up that value. The distribution of Q_1, as well as Q_2, Q_3 and so forth, remains broad as the system approaches the thermodynamic limit.

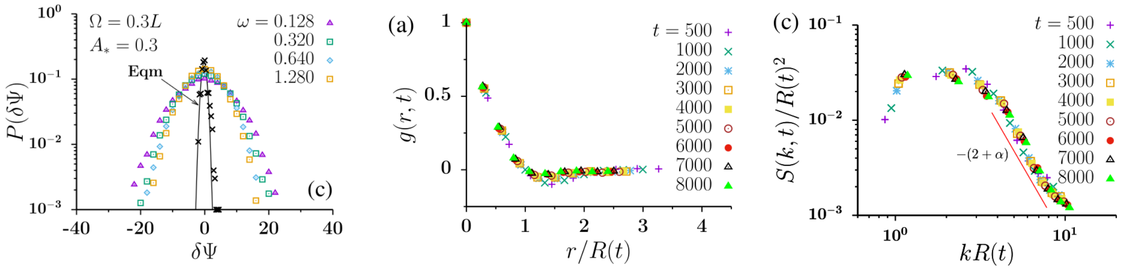

Figure 4.7: (a)Probability distribution of local density (b) Scaled two point correlation (c) Scaled structure factor, Image taken from: [141].

4.5.2 Cusp singularity and non-Porod behaviour

The spatial correlation function $C(r)$ maintains a scaling form in $|r/L|$, akin to what is observed in equilibrium systems. However, it displays a cusp singularity at small values of $|r/L|$. This cusp behavior can be described by:

$$C\left(\frac{r}{L}\right) = c_0 - c_1\left|\frac{r}{L}\right|^{\alpha}, \quad \left|\frac{r}{L}\right| \ll 1 \tag{4.16}$$

where α represents the cusp exponent ($\alpha < 1$), and c_0, c_1 are the constants. Consequently, the scaled structure factor $S(k)$ has the form:

$$s(k) \sim \frac{L^d}{(kL)^{d+\alpha}} \tag{4.17}$$

where d denotes the dimensionality. This observation marks a significant departure from the Porod law. This deviation arises due to the power-law distribution of clusters within the interfacial region that separates the domains of pure phases. In contrast to traditional phase ordering, where the interfacial region between phases is well-defined, in FDPO, this region occupies a significant fraction of the system size and has a complex structure. The interfacial area contains segments of pure phases interwoven with similar regions, forming a repeating pattern throughout the system. A schematic representation of this distinction is depicted in Fig. 4.6(b), illustrating the linear decay typical of normal phase ordering and the cuspy decay indicative of FDPO.

A. Das et al. [141] performed a simulation study on the phase segregation of passive advective scalars within a medium of dynamic asters, which are localized contractile structures. The study examined how aster density and the ratio of aster remodeling rates to particle diffusion rates affect phase segregation. The model used in this study involved passive and inert particles distributed within an active two-dimensional medium. The results showed that the dynamics of segregation and the characteristics of the active phase-segregated state differ significantly from those of conventional phase segregation. Firstly, unlike traditional segregation driven by chemical potential gradients, active phase segregation is driven by active advection, enabling it to occur at temperatures higher than those required for equilibrium segregationâan effect particularly relevant in cellular environments. Secondly, the domain coarsening behavior deviates significantly from Porod's law, indicating that the interfaces are diffuse with low interfacial tension. Lastly, the active segregated phase displays significant fluctuations in both the integrated order parameter and domain size, with broad, non-Gaussian distributions, in contrast to the narrow, peaked distributions typically seen in equilibrium systems. Figure 4.7(a) illustrates the distribution of the order parameter, 4.7(b) shows the scaled correlation function of the order parameter, and 4.7(c) depicts the non-Porod behavior of the order parameter.

4.6 Cusp exponent and cluster size distribution

Macroscopic fluctuations have a significant impact on both spatial correlation and cluster distribution. As observed, when the two-point correlation function $C(r)$ is scaled by the coarsening length scale L, all the curves collapse onto a single curve, with the scaled correlation function $C(r/L)$ following the relation 4.16. In a 1D system, if clusters are defined as continuous lattice sites l occupied by similar particles, the cluster size distribution $P(l)$ follows a power law, $P(l) \sim l^{-\theta}$, where θ represents the associated exponent. The physical origin of the cusp is the interfacial regions between particle-rich and particle-poor areas, where several particle and hole clusters are present, leads the structures that is responsible for the observed non-Porod behavior [139].

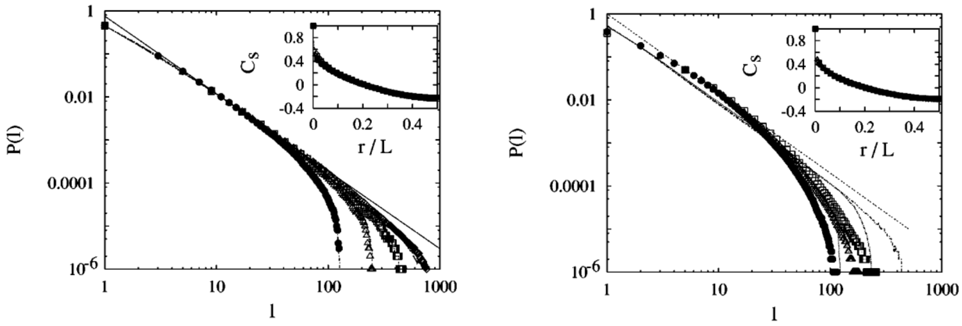

Figure 4.8: (a) The distribution of cluster sizes $P(l)$ as a function of l for clusters and holes in the sliding particle (SP) model with an Edwards-Wilkinson (EW) surface across various system sizes. The distribution $P(l)$ exhibits a power-law decay characterized by $\theta \approx 1.8$. The inset shows the collapsed curve of $C(r)$, corresponding to a cusp exponent $\alpha \approx 0.5$. (b) The $P(l)$ vs l distribution for clusters and holes in the SP model with a Kardar-Parisi-Zhang (KPZ) surface for different system sizes, where $P(l)$ also follows a power-law decay with $\theta \approx 1.85$. The inset displays the collapsed curve of $C(r)$ with a cusp exponent $\alpha \approx 0.25$. Image adapted from [140].

Within the Independent Interval Approximation (IIA) framework, there is a relationship between the cusp exponent α and the cluster size distribution exponent θ. In this method, the probability of having n consecutive intervals is approximated by the product of the distributions of individual intervals. These intervals represent successive clusters of particles and holes. By applying the mathematical techniques discussed in [139, 140, 144], the correlation function $C(r)$ can be approximated as follows:

$$C(r) \approx 1 - \frac{b}{a\Gamma(3-\theta)} \left|\frac{r}{L}\right|^{2-\theta} \tag{4.18}$$

This expression has the same scaling as Eq. 4.16. By comparing the cusp singularity in Eqs. 4.16 and 4.18, the relation between θ and α is given by:

$$\theta + \alpha = 2 \tag{4.19}$$

This relation has been validated in certain models. Figure 4.8(a) displays the cluster size distribution $P(l)$ as a function of l for clusters and holes in the Sliding Particle (SP) model

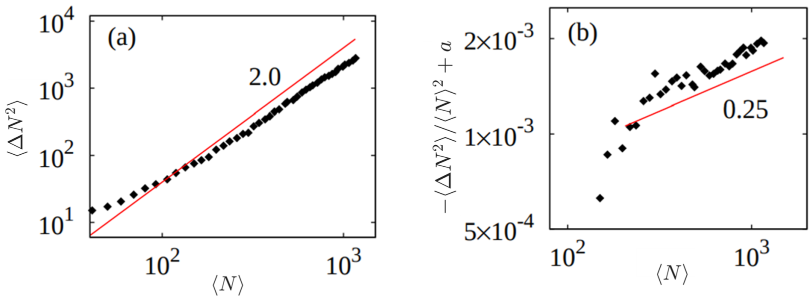

Figure 4.9: (a) The number fluctuation $\langle \Delta N^2 \rangle$ as a function of $\langle N \rangle$, (b) The subleading corrections after the leading term is subtracted from $\langle \Delta N^2 \rangle$. Image adapted from SI of [146].

with an Edwards-Wilkinson (EW) surface, across various system sizes. The distribution $P(l)$ exhibits a power-law decay with an exponent $\theta \approx 1.8$, and the inset presents the collapsed curve of $C(r)$, corresponding to a cusp exponent $\alpha \approx 0.5$, resulting in $\theta + \alpha \approx 2.3$. Figure 4.8(b) shows the $P(l)$ vs l distribution for clusters and holes in the SP model with a Kardar-Parisi-Zhang (KPZ) surface for different system sizes. Here, $P(l)$ also follows a power-law decay with $\theta \approx 1.85$, and the inset depicts the collapsed curve of $C(r)$ with a cusp exponent $\alpha \approx 0.25$, leading to $\theta + \alpha \approx 2$. These findings indicate that, although the IIA provides valuable insights, it is not entirely precise. These results suggest that even thought the IIA is not exact, it provides useful insights.

4.7 Cusp exponent and giant number fluctuation

The fluctuations in particle density within the ordered phase are characterized by the number fluctuation, $\langle \Delta N^2 \rangle = \langle N^2 \rangle - \langle N \rangle^2$, where N represents the particle count. In active matter systems, the relation $\langle \Delta N^2 \rangle = \langle N \rangle^\beta$ is observed, with $\beta > 1$ signifying giant number fluctuations (GNF), while $\beta = 1$ corresponds to normal thermal fluctuations. Numerous studies have reported the presence of giant number fluctuations in active matter systems [20, 45, 113, 145].

Coarsening in active matter systems with a dynamic length scale $l(t)$ shows non-Porod behavior. Supravat et al. [146] studied numerically to determine whether the fluctuations leading to giant number fluctuations (GNF) are the same as those responsible for the violation

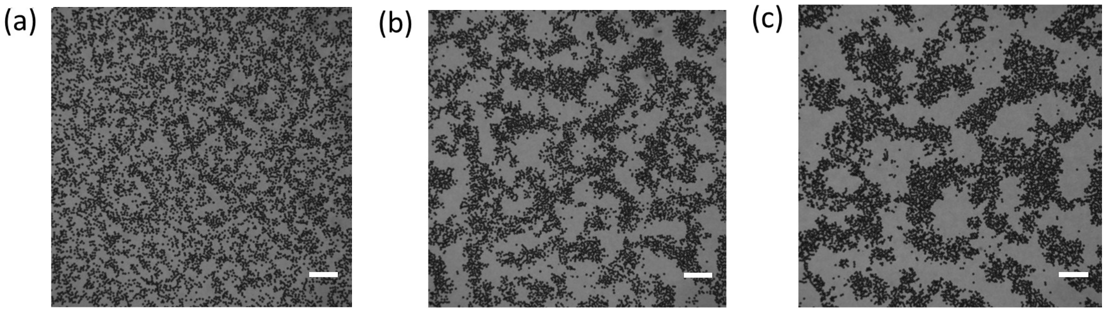

Figure 4.10: Bright field images at different times:(a) after 1 min (b) after 40 min (c) after 210 min, scale bar $200\mu m$.

of Porod's law. The number fluctuation, including subleading terms, can be expressed as:

$$\langle \Delta N^2 \rangle \sim a\langle N \rangle^2 - \frac{b}{l^\alpha}\langle N \rangle^{\alpha/d+2} + ... \tag{4.20}$$

They propose that by measuring the subleading correction to GNF, the cusp exponent of non-Porod behavior can be directly obtained. Figure 4.9(a) illustrates $\langle \Delta N^2 \rangle$ as a function of $\langle N \rangle$. A clear deviation from the slope of 2.0 is observed at large $\langle N \rangle$, which can be explained by the subleading term in Eq. 4.20. To determine the cusp exponent α, the plot of $\langle \Delta N^2 \rangle / \langle N \rangle^2 + a$ against $\langle N \rangle$ is shown in Fig. 4.9(b), where the growth follows a power law with $\alpha/d \approx 0.25$, leading to $\alpha \approx 0.5$.

4.8 Experimental methods

In our study, we employed a suspension of E. coli as an active fluid, complemented by polystyrene beads of $15\mu m$ in size, serving as passive beads. The procedure for preparing the active fluid is same as the one detailed in Section 2.3. Throughout our experiments, we maintained a constant bacterial density equivalent to $5b_0$, where $b_0 = 6 \times 10^9$ cells/ml. Notably, the colloidal beads used in this study are sufficiently large that makes them athermal and non-Brownian. The dynamic behavior of the passive beads within the active fluid is exclusively driven by the inherent activity of the fluid medium and their hydrodynamic interactions. To facilitate our measurements, we constructed an observation chamber by affixing a

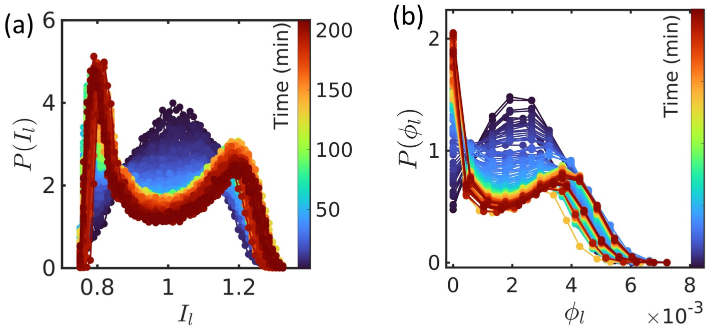

Figure 4.11: (a) Probability distribution function $P(I_l)$ for local intensity I_l. (b) Probability distribution function $P(\phi_l)$ for local density ϕ_l. The color bar indicates time progression in minutes.

circular cavity of 1 cm in diameter and 100 μm in depth to a coverslip coated with polyethylene glycol (PEG), using double-sided tape. For experimentation, we thoroughly mixed the active fluid and passive beads before introducing them into the sample chamber, which was subsequently mounted on the microscope stage. Following the loading procedure, we started taking measurements right from the beginning. Throughout our data collection process, we captured snapshots of the sample at regular intervals of 2 FPS over a total duration of 3 hours and 30 minutes.

4.9 Results and discussions

Figure 4.10(a)-(c) shows bright field images of the phase-ordering system captured at different time intervals: $t = 1$ min, $t = 40$ min, and $t = 210$ min. The scale bar corresponds to 200 μm. In our analysis, we began by computing the distribution of local intensity $P(I_l)$ directly from the raw images. This was done using a box size of $3\sigma \times 3\sigma$, where I_l is defined as the mean intensity of pixels within this box, divided by the mean intensity of the entire image. Figure 4.11(a) illustrates the distribution of local intensity. At the initial time $t = 0$ min, the colloid-bacteria mixture is homogeneously distributed, as reflected in $P(I_l)$. As time advances, the system undergoes phase separation, leading to a bimodal distribution in $P(I_l)$. Additionally, we calculated the local coarse-grained number density (ϕ_l) using the same box size of $3\sigma \times 3\sigma$. The local number density ϕ_l is determined by counting the number of particles within the box and dividing it by the area of the box. The resulting distribution $P(\phi_l)$, shown in Figure 4.11(b), follows a similar trend as $P(I_l)$. The color bar indicates time progression in minutes. Notably, while both distributions capture the same overall trend, $P(I_l)$ and $P(\phi_l)$ diverge at the lower end of the x-axis, because in the case of particle position, we may get box with no particles but we'll always get some finite value of mean intensity in the defined box.

The probability distribution function $P(\phi_l)$, shown in Fig. 4.11(b), is calculated from the position coordinates of the colloids obtained through tracking. After characterizing the local density (or local intensity), we introduced an order parameter, denoted as ψ. While a box of size $3\sigma \times 3\sigma$ was used for calculating $P(I_l)$ and $P(\phi_l)$ for better representation of distribution, subsequent calculations employed a box of size $2\sigma \times 2\sigma$. The order parameter ψ takes the value of $+1$ when the local density ϕ_l (or local intensity I_l) is equal to or greater than the global density ϕ (or global intensity I), and -1 when the local density ϕ_l (or local intensity I_l) is less than the global density ϕ (or global intensity I). Mathematically, this can be expressed as:

$$\psi = \begin{cases} +1 & \text{for } \phi_l \geq \phi \text{ (or } I_l \geq I) \\ -1 & \text{for } \phi_l < \phi \text{ (or } I_l < I) \end{cases} \tag{4.21}$$

To visually distinguish the differences, refer to the upper panel of Fig. 4.12. In 4.12(a), the raw bright-field image is displayed. 4.12(b) shows the local intensity calculated within a $2\sigma \times 2\sigma$ box, and 4.12(c) presents the corresponding order parameter. Whereas, the lower panel of Fig. 4.12(d)-(e) shows the particle positions from the images, the local density (ϕ_l) defined in a $2\sigma \times 2\sigma$ box, and the associated order parameter.

The equal-time spatial correlation function $C(\mathbf{r}, t)$ of the order parameter is defined as:

$$C(\mathbf{r}, t) = \langle \psi(\mathbf{r}_1, t)\psi(\mathbf{r}_2, t) \rangle - \langle \psi(\mathbf{r}_1, t) \rangle \langle \psi(\mathbf{r}_2, t) \rangle \tag{4.22}$$

where $\mathbf{r}_1$ and $\mathbf{r}_2$ are the position vectors of the order parameters ψ, separated by the distance vector $\mathbf{r}$. The equal-time structure factor, denoted as $S(\mathbf{k}, t)$, is then defined as the Fourier

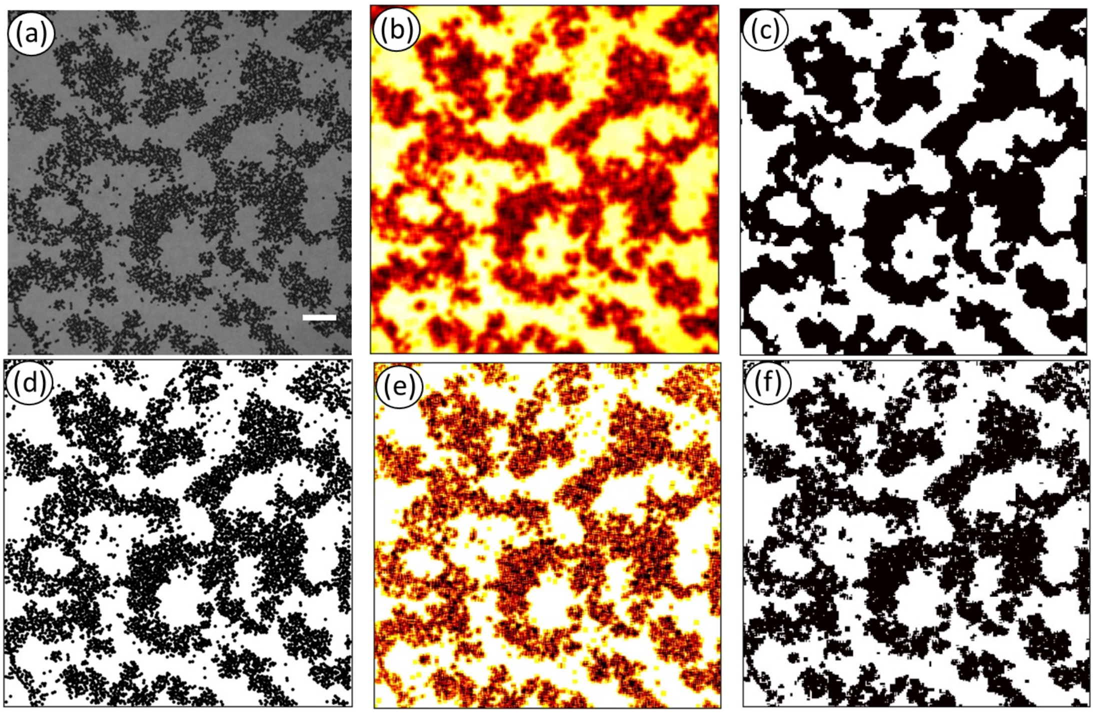

Figure 4.12: Upper panel: (a) Bright-field image at $t = 210$ min, with a scale bar of 200 μm. (b) Local intensity I_l, as defined in a $2\sigma \times 2\sigma$ box, corresponding to the image in (a). (c) Order parameter ψ, calculated based on I_l. Lower panel: (d) Particle positions tracked from the image in (a). (e) Local density ϕ_l defined within a $2\sigma \times 2\sigma$ box. (f) Order parameter ψ, calculated using ϕ_l.

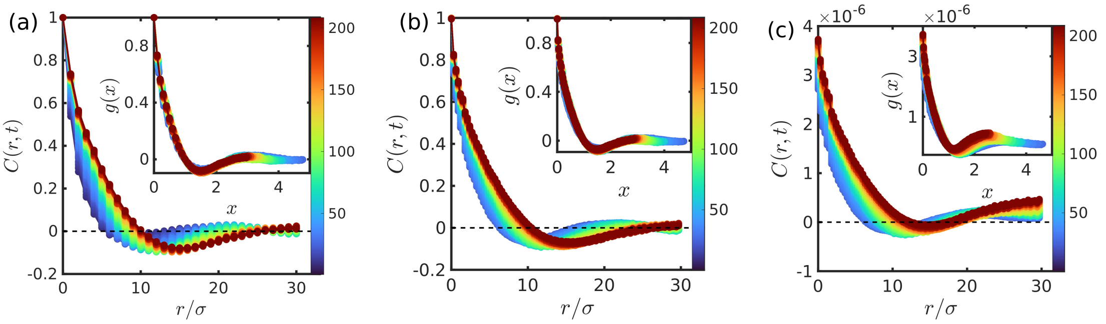

Figure 4.13: Main panel: Spatial correlation function $C(r,t)$ as a function of the separation distance r/σ, where σ is the diameter of colloids. The dynamic length scale $l(t)$, determined from the point where $C(r,t)$ intersects the zero level, is indicated by the dashed black line. Inset: The scaled spatial correlation function, represented by $C(\mathbf{r},t) = f(\mathbf{r}/l(t)) = g(x)$, is plotted against the scaled variable x. Color bar represents the increasing time. (a) Correlation for the order parameter ψ calculated from local intensity I_l. (b) Correlation for ψ calculated from local density ϕ_l. (c) Correlation for the local density ϕ_l itself.

transform of $C(\mathbf{r},t)$:

$$S(\mathbf{k},t) = \langle \tilde{\psi}(\mathbf{k},t)\tilde{\psi}(-\mathbf{k},t)\rangle \tag{4.23}$$

Here, $\langle ... \rangle$ represents ensemble averaging, and $\tilde{\psi}$ represents the Fourier transform of ψ. The dynamic length scale $l(t)$ is obtained from the point where $C(\mathbf{r},t)$ intersects the zero level. Notably, when $C(\mathbf{r},t)$ is scaled by $l(t)$, all curves collapse onto a single universal curve, indicating the presence of a single characteristic length scale. Consequently, both $C(\mathbf{r},t)$ and $S(\mathbf{k},t)$ follow scaling forms:

$$C(\mathbf{r},t) = f\left(\frac{\mathbf{r}}{L(t)}\right) \tag{4.24}$$

$$S(\mathbf{k},t) = L^d g(kL(t)) \tag{4.25}$$

Here, the dimensionality d is equal to 2 for our system.

Figure 4.13(a) and 4.13(b) display the spacial correlation function $C(\mathbf{r},t)$ using the order parameter ψ, which is derived from the local intensity I_l and local density ϕ_l, respectively. These figures demonstrate that the results are exactly same regardless of whether the order parameter is defined by local intensity or local density. We will use the order parameter de-

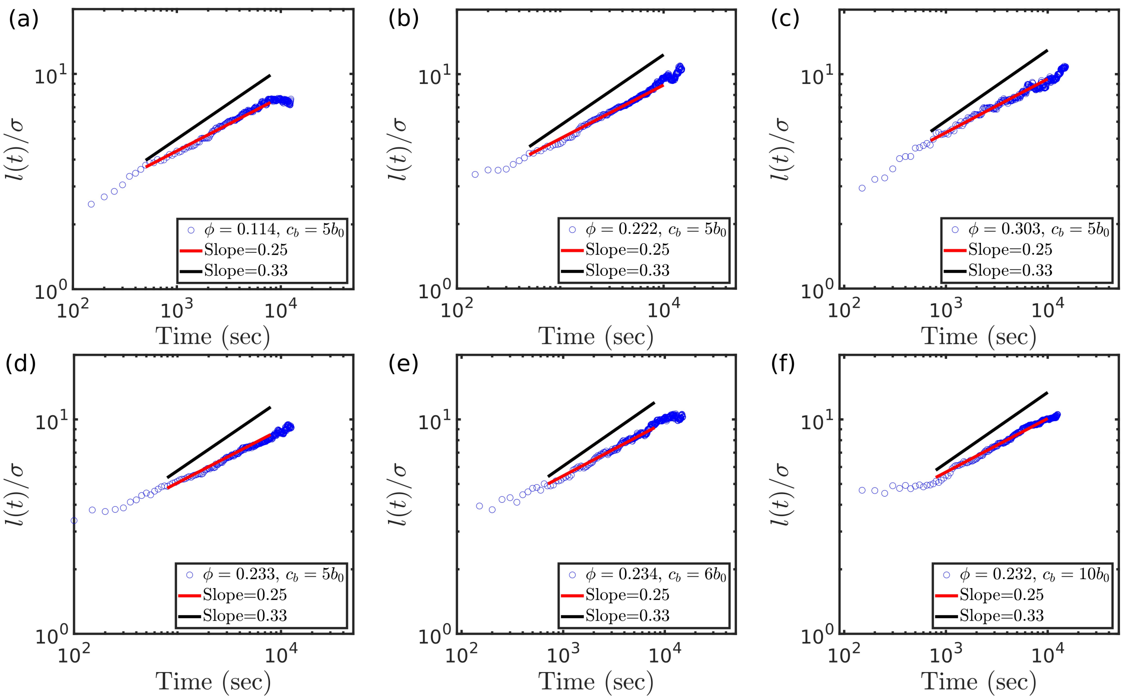

Figure 4.14: Upper panel (a)-(c): Length scale $l(t)$ at various area fraction$\phi = 0.1,\ 0.2,$ and 0.3 for fixed bacterial density $c_b = 5b_0$. lower panel(d)-(e): Length scale $l(t)$ at various bacterial density $c_b = 5b_0,\ 6b_0$ and $10b_0$ for fixed area fraction $\phi \sim 0.2$. Red line and black line has slope 0.25 and 0.33 respectively.

fined by local density for all subsequent results. Figure 4.13(c) shows the spacial correlation function $C(\mathbf{r}, t)$ of local density ϕ_l itself. The main panel of the all plots presents $C(r, t)$ as a function of r in terms of σ. The dynamic length scale $l(t)$ extracted from $C(r, t)$ when it intersects the zero level indicated by the dashed black line. While the inset shows the scaled spatial correlation represented by $C(\mathbf{r}, t) = f(\mathbf{r}/l(t)) = g(x)$ as a function of the scaled variable x with color bar indicating the increasing time. The dynamical length scale, $l(t)$, extracted from $C(r, t)$ at the zero-crossing point, grows over time as $l(t) \sim t^{1/4}$ which is slower than the thermal coarsening length scale $l(t) \sim t^{1/3}$. To further confirm the robustness of the dynamic length scale, we have plotted $l(t)$ for various area fraction of colloids $\phi = 0.1,\ 0.2,$ and 0.3 at fix bacterial density $c_b = 5b_0$ as shown in Figs. 4.14(a)-(c), and for different bacterial density $c_b = 5b_0,\ 6b_0$ and $10b_0$ at fix area fraction $\phi \sim 0.23$, as shown in Figs. 4.14(d)-(e). Red curve has slope 0.25, while black curve has slope 0.33. All the length

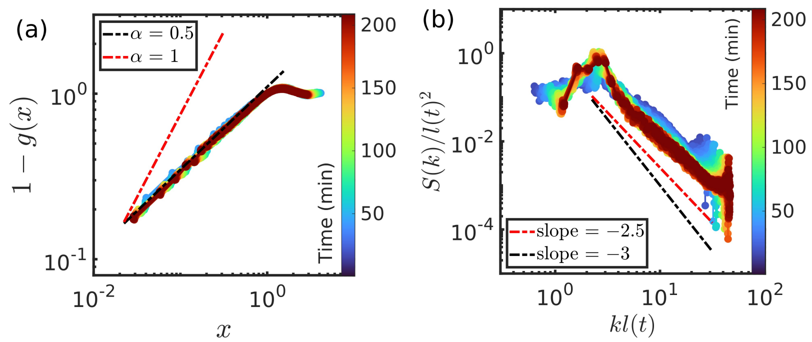

Figure 4.15: (a) Log-log plot of $(1 - g(x))$ as a function of x to observe the cusp exponent. The black and red dashed lines represent slopes of 0.5 and 1, respectively. (b) Scaled structure factor of the order parameter $S(k)/l(t)^2$ plotted against $kl(t)$. The black and red dashed lines correspond to slopes of -3 and -2.5, respectively. The color bar indicates the time progression in minutes.

scales $l(t)$ were extracted from the spatial correlation function of order parameter defined by local density ϕ_l.

In this far-from-equilibrium system, the behavior deviates from the well-known Porod's law. Specifically, the correlation function $C(r, t)$ does not follow a linear decay as r approaches zero. Instead, it exhibits a cusp singularity near this limit. The short-distance scaled $C(r, t)$ can be expressed as:

$$g(x) = 1 - Ax^{\alpha} + \dots \tag{4.26}$$

where α is the cusp exponent, with a value less than 1. Figure 4.15(a) shows the log-log plot of $1 - g(x)$ against x, based on Eq. 4.26. The black and red lines correspond to slopes of 0.5 and 1, respectively. It's clear from Fig. 4.15(a) that for small x, the slope is approximately 0.5, which is significantly different from the slope of 1 observed in systems undergoing thermal coarsening.

The deviation from Porod's law is further captured by the structure factor $S(k, t)$, which is defined as:

$$S(k, t) \sim \frac{L^d}{(kL)^{d+\alpha}} \tag{4.27}$$

where d denotes the dimensionality of the system. In Fig. 4.15(b), the scaled structure factor

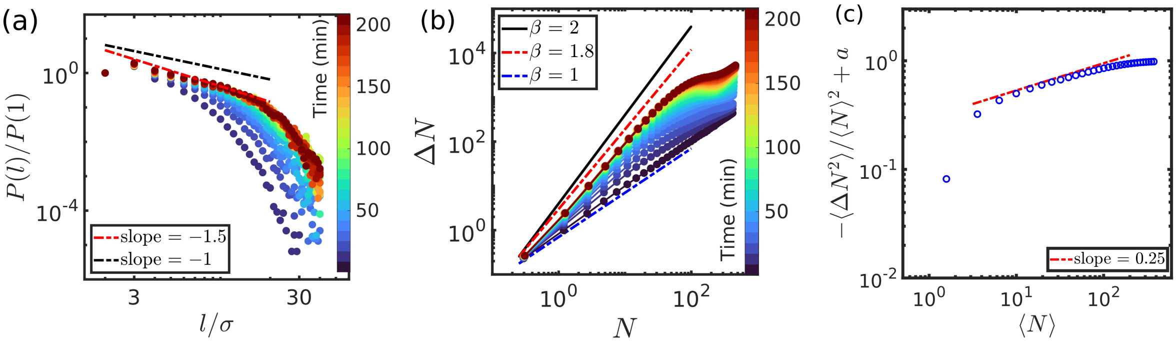

Figure 4.16: (a) The cluster size distribution $P(l)$ for 1-D clusters of length l with continuous $\psi = +1$, obtained from horizontal and vertical cuts in the order parameter space. (b) Giant number fluctuations characterized by an increasing exponent β that evolves from 1 to 1.8 over time. (c) Subleading corrections to $\langle \Delta N^2 \rangle$ after subtracting the leading term.

$S(k,t)/l(t)^2$ is plotted against $kl(t)$. The black and red lines have slopes of -3 and -2.5, respectively. Here, we observe a power-law decay in $S(k,t)$ for sufficiently large values of $kl(t)$, with the slope of 2.5 confirming the presence of non-Porod behavior.

In previous studies, the clusters in the cluster size distribution was defined by counting the number of particles within a cluster that satisfies a cutoff distance of 1.2σ. In a 2D system, this approach correlates the number of particles to the area occupied by the cluster. Here, we define clusters as the length l of continuous occurrence of ψ with value $+1$, from 1-dimensional cuts taken horizontally and vertically through the order parameter space. The distribution of these line segments, $P(l)$ vs l, is presented in Fig. 4.16(a). The vertical axis has been normalized using $P(1)$ for comparison across all plots, while the horizontal axis represents l in units of σ. The red and black lines correspond to slopes of -1.5 and -1, respectively. In Figure 4.16(a), a power-law decay is evident at large time scales, described by $P(l)/P(1) \sim l^{-\theta}$, where θ is approximately 1.5 in this instance. This result is consistent with the relationship $\theta + \alpha = 2$, further validating the observation.

Giant number fluctuations are observed in phase-ordering systems, as described in Sec. 4.7 with the slope $\beta > 1$. Figure 4.16(b) illustrates that when particles are initially homogeneously distributed, the slope is approximately $\beta \sim 1$. Over time, the slope increases and eventually stabilizes at $\beta \sim 1.8$, indicating the presence of giant number fluctuations. The subleading corrections to these fluctuations, as outlined in Eq. 4.20, have been calculated and are presented in Fig. 4.16(c) with a constant $a = 1$.

4.10 Conclusions

In summary, we conducted a detailed investigation into the coarsening of colloidal clusters in active liquids. The homogeneous mixtures of colloids and swimmers are inherently unstable, leading to spontaneous phase separation through the formation of dynamic clusters. While our experiments successfully capture the early stages of coarsening, observing the late stages exceeds our experimental timescales. We have discovered interesting effects of activity on the phase ordering of colloids. The correlation functions of the scalar order parameter reveal dynamic scaling, with the dynamic length scale growing as $L(t) \sim t^{1/4}$, indicating deviations from the Lifshitz-Slyozov law. The deviations from Lifshitz-Slyozov predictions have been reported in several numerical studies [133, 137, 141]. However, experiments with active colloids and colloid-bacteria mixtures have reported Ostwald ripening with $t^{1/3}$ growth [21, 147, 148]. To the best of our understanding, our results are first experimental illustration of deviations from Lifshitz-Slyozov law in active matter. Furthermore, the correlation functions of the order parameter displays a cusp singularity, suggesting rough interfaces separating the colloid-rich and colloid-poor phases in our system. These signatures are robust and the calculation of structure factor indeed confirms non-Porod behavior. Also, the scaling of the radius of gyration of the clusters reveals the fractal nature of clusters with rough boundaries. These results strongly demonstrate that activity lowers the interfacial tension, leading to diffuse and rough interfaces. Our system exhibits all the characteristics of fluctuation-dominated phase ordering, a phenomenon first reported in lattice models. The exponents reported in our experiments match closely with the exponents predicted in FDPO lattice models. Once again, these are first experimental demonstration of FDPO in active matter. All these results point to a novel phase ordering of colloids in active liquids.

Chapter 5

Percolation of Nonequilibrium Assemblies of Colloidal Particles in Active Chiral Liquids

The contents of this chapter are based on our published work [149].

The growing interest in the non-equilibrium assembly of colloidal particles in active liquids is driven by the motivation to create novel structures endowed with tunable properties unattainable within the confines of equilibrium systems. Here, we present an experimental investigation of the structural features of colloidal assemblies in active liquids of chiral E. coli. The colloidal particles form dynamic clusters due to the effective interaction mediated by active media. The activity and chirality of the swimmers strongly influence the dynamics and local ordering of colloidal particles, resulting in clusters with persistent rotation, whose structure differs significantly from those in equilibrium systems with attractive interactions, such as colloid-polymer mixtures. Our colloid-bacteria mixture displays several hallmark features of a percolation transition at a critical density, where the clusters span the system size. A closer examination of the critical exponents associated with cluster size distribution, average cluster size, and correlation length in the vicinity of the critical density show deviations from the prediction of the standard continuum percolation model. Therefore, our experiments reveal a richer phase behavior of colloidal assemblies in active liquids.

5.1 Introduction

A defining characteristic of active matter is the internal energy source that drives the system out of equilibrium [19, 23]. Various living and synthetic systems, spanning a wide range of length scales and featuring diverse interaction rules among their elementary constituents, fall within this category. Examples include living systems, ranging from animals to bacteria, and synthetic systems such as microtubules driven by molecular motors [150], suspensions of Janus particles [151] or Quincke rollers [71], and others. The distinguishing feature of active systems lies in their departure from the principles of detailed balance and time reversal symmetry. This deviation from equilibrium constraints gives rise to fascinating emergent phenomena, such as flocking [70, 71, 152], motility-induced phase separation [74, 95, 132], active turbulence [153], and superfluidity [30]. Nonequilibrium fluctuations in active systems have been exploited for various applications, including micron sized heat engines [154], the self-assembly of novel biomimetic materials [25, 155, 156] with diverse functionalities and drug delivery, among others [23].

In recent years, there has been a growing interest in understanding the phase behavior of mixtures involving both active and passive components, particularly emphasizing the phase behavior of passive entities in active liquids. Earlier experiments investigated the hierarchical organization of bio-polymers driven by molecular motors, leading to considerable insight into active gels [155–158]. These materials are inherently out of equilibrium, mimicking the nonlinear mechanical properties of cellular materials. Such studies have inspired the investigation of colloidal analogs of active gels. However, experiments on this topic are limited [159]. The aspects that have received attention include the transport properties of colloidal particles at dilute densities [41, 160–162] and the effective interaction between a pair of colloidal particles in active fluids [83, 86, 87, 89, 90, 114]. This has led to a better understanding of the interaction between passive and active particles. Despite these advances, the collective behavior of dense assemblies of colloidal particles in active liquids remains poorly explored in experimental systems. Recent experiments have reported dynamic clustering of colloidal particles in active liquids of E. coli suspensions [63,68,148]. The structure and size of the aggregates were reported to depend on the size ratio of colloidal particles to active particles [63, 98] and the density of active particles [68, 148]. Earlier studies had revealed that E. coli swims in clockwise circular trajectories close to solid boundaries [38, 163], and their chiral motion leads to interesting effects, such as the persistent rotational motion of microscopic gear-like structures suspended in such liquids [164,165]. The authors [164] found that both asymmetric and symmetric gear-like structures at solid-liquid interfaces display clockwise rotation. This rotation was attributed to the chiral motion of bacteria. These ideas were further elucidated by Grober and coworkers [159] using a toy model. They showed that the collision between an active swimmer moving along a chiral curved trajectory and a circular aggregate gives rise to unbalanced tangential forces, resulting in a net torque and rotation of aggregates. Their experiments were performed using suspensions of colloidal particles, E. coli and depleting polymers. Furthermore, this system was reported to form unconventional gel structures endowed with novel properties not achievable in equilibrium analogs. What is not clear from their study is the role of activity and its influence on the phase behavior of colloids when the depletion interaction due to polymers is absent. The thermal analogs of such physical gels, assembled using colloid-polymer mixtures, have received wide attention [9, 112, 166–168], and the emergence of rigidity in these systems is well studied. The role of percolating networks, particularly the directed percolation and isotropic percolation scenarios [112, 168–170], is well appreciated. However, there is limited discussion about percolation of colloidal assemblies in active liquids where the colloids form dynamic clusters [171–173] due to effective interactions mediated by active media.

Here, we present the findings of an experimental investigation of the percolation transition in a system of colloids particles suspended in active liquids of chiral E. coli. The experiments are conducted in close proximity to a solid-liquid interface, where the swimmers exhibit chiral trajectories. The circular trajectories are apparent at low densities of bacteria, but this feature diminishes at higher densities due to interactions between the swimmers (see section 2.5.3). Despite the absence of such circular trajectories, the interaction between bacteria and a colloidal particle results in unbalanced tangential forces, leading to persistent rotations of colloids and their aggregates (see supplementary videos SV1 and SV2 of [149]). This indicates that the chiral nature of bacterial fluid does not disappear even at high densities. Therefore, we refer to suspensions of E. coli as chiral active liquids. Two notable differences between our experiments and those presented in a recent work by Grober and co-workers [159] are that our spheres are athermal or non-Brownian and there is no depletion interaction between the colloids due to polymers. In our system, the effective interaction between the colloidal particles arises solely due to the activity of the bath, leading to the formation of dynamic clusters [63, 68, 98], in contrast to the irreversible aggregates formed in [159]. Furthermore, the interactions of swimmers with the colloidal particles break the chiral symmetry of colloids, resulting in clusters with persistent rotations. It hinders the orientational ordering of colloids within the clusters, leading to distinct structural features compared to equilibrium colloid-polymer mixtures. The clusters in our system grow with increasing density of colloids and eventually span the system size. This phenomenon displays several hallmark features of equilibrium percolation [174–176]. However, the presence of activity and chirality gives rise to exponents that deviate from standard percolation models.

5.2 Network formation and connectivity: Percolation theory

Percolation theory serves as a fundamental concept in statistical mechanics, providing insights into the emergence of connected structures in random systems. Its broad applicability spans disciplines ranging from materials science and earth sciences to social networks and biological systems. It offers a rich framework for understanding complex phenomena characterized by phase transitions and critical behavior [167, 174, 177]. The study of percolation involves random lattice models, where the system is represented by a discrete lattice or network. This includes site percolation, where individual lattice sites are either occupied or vacant, and bond percolation, where bonds between neighboring sites are either present or absent. The combination of site and bond percolation, known as site-bond percolation. The schematic representation of site-percolation (a) , bond-percolation (b) and continuum percolation (c) is shown in the Fig. 5.1.

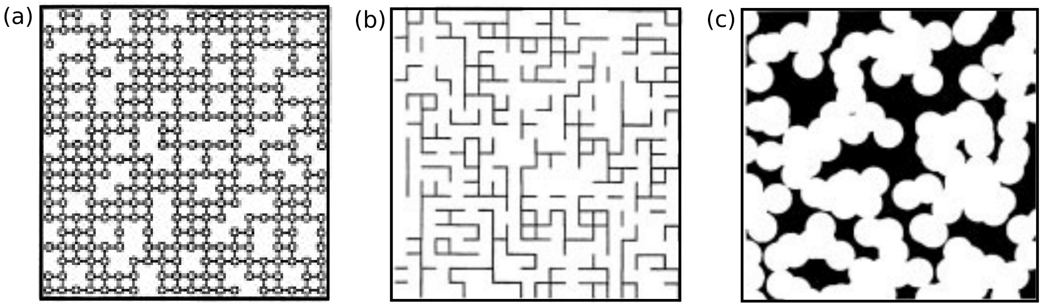

Figure 5.1: The schematics representation of (a) Site percolation (b) bond percolation (c) continuum percolation. Images has been taken from [178].

While most natural systems correspond to continuum percolation, where components are not confined to discrete lattice sites, much analytical and numerical work has focused on lattice percolation. This preference is justified by the shared universality class of continuum and lattice percolation. However, when addressing non-universal properties such as threshold location, discrete and continuum models must be analyzed individually [178,179]. To gain a deeper understanding of the percolating system and explore critical exponents and associated properties, let's examine an exactly solvable lattice model in one dimension (1-D) [174,180].

5.2.1 Percolation theory in one-dimensional systems

The 1-D percolation problem can be solved exactly, and some aspects of this solution are applicable to higher dimensions as well. Consider a lattice consisting of L sites, as illustrated in Fig. 5.2. Each site on the lattice can be occupied with a probability p or left empty with a probability $(1-p)$. Here, p represents the occupation probability or concentration. Given that the sites are occupied randomly, the probability that a cluster of s consecutive sites is fully occupied is p^s, while the probability that one end of this cluster is adjacent to an empty site is $(1-p)$. Since the two ends are statistically independent, the total probability that a

Figure 5.2: Schematic illustration of percolation in a 1-D lattice: Empty sites are marked with crosses, while occupied sites are shown as solid circles. In the segment of the infinite 1-D lattice depicted above, there is one cluster of size 5, one cluster of size 2, and three clusters of size 1. Image adapted from [180].

site is occupied or not, while being the left (or right) end of an s-cluster, is $p^s(1-p)^2$.

Now, let's consider the probability of an arbitrary site being part of an s-cluster, denoted as $s(1-p)^2p^s$, and the number of such clusters being $s(1-p)^2p^sL$. As $L \to \infty$, we can ignore boundary effect. Then, the number of s-cluster per site, denoted as $n_s(p)$, is calculated as follows:

$$\begin{aligned} n_s(p) &= (1-p)^2p^s \\ &= (1-p)^2\exp(\ln(p^s)) \\ &= (1-p)^2\exp(s\ln p) \\ &= (p_c-p)^2\exp(-\frac{s}{s_\xi}) \end{aligned}$$

where, s_ξ is characteristic cluster size with

$$s_\xi = -\frac{1}{\ln p} = -\frac{1}{\ln(p_c-(p_c-p))} \to \frac{1}{p_c-p} = (p_c-p)^{-1}$$

In the limit $p \to p_c (= 1)$, $\qquad s_\xi \propto (p_c-p)^{-1}$.

In the last expression, Taylor's expansion has been used in the limit $x \to 0$

$$\ln(1-x) = -x - \frac{1}{2}x^2 - \frac{1}{3}x^3 - ... \approx -x$$

This divergence is also observed in higher dimension with the critical exponent σ. The general form of cluster size distribution is given as follows:

$$n_s(p) \propto s^{-\tau} \exp(-\frac{s}{s_\xi}), \quad \text{for } s \gg 1 \tag{5.1}$$

with,

$$s_\xi \propto |p_c - p|^{-\frac{1}{\sigma}}, \quad \text{for } p \to p_c$$

Every occupied site is part of a cluster, so the likelihood that any given site is part of a cluster is simply the probability p that the site is occupied.

$$\sum_{s=1}^{\infty} s n_s(p) = p, \quad \text{for } p < p_c$$

The mathematical proof is given as,

$$\begin{aligned}
\sum_{s=1}^{\infty} s n_s(p) &= \sum_{s=1}^{\infty} s(1-p)^2 p^s \\
&= (1-p)^2 \sum_{s=1}^{\infty} p \frac{d(p^s)}{dp} \\
&= (1-p)^2 p \frac{d}{dp} \left(\sum_{s=1}^{\infty} p^s \right) \\
&= (1-p)^2 p \frac{d}{dp} \left(\frac{p}{1-p} \right) \\
&= p
\end{aligned}$$

The probability that a site is occupied is p. For any arbitrary site, whether occupied or not, the probability that it belongs to an s-cluster is given by $sn_s(p)$. Thus, w_s denotes the probability that the cluster containing any randomly chosen occupied site consists of exactly s sites.

$$w_s = \frac{sn_s(p)}{p} = \frac{sn_s(p)}{\sum_{s=1}^{\infty} sn_s(p)}$$

Thus the average cluster size is defined as,

$$\begin{aligned}
S(p) &= \sum_{s=1}^{\infty} s w_s \\
&= \frac{\sum_{s=1}^{\infty} s^2 n_s(p)}{\sum_{s=1}^{\infty} s n_s(p)} \\
&= \frac{1}{p}(1-p)^2 \sum_{s=1}^{\infty} s^2 p^s \\
&= \frac{1}{p}(1-p)^2 \left(p\frac{d}{dp}\right)^2 \left(\sum_{s=1}^{\infty} p^s\right) \\
&= \frac{1}{p}(1-p)^2 \left(p\frac{d}{dp}\right)^2 \left(\frac{p}{1-p}\right)
\end{aligned}$$

applying the operator $p\frac{d}{dp}$ twice, we arrive at

$$S(p) = \frac{1+p}{1-p} = \frac{p_c+p}{p_c-p}$$

Here, p_c refers to the critical occupation probability, or percolation threshold, which is defined as the concentration p at which an infinite cluster first emerges in an infinite lattice. In the case of a 1-D lattice, the critical occupation probability is $p_c = 1$. As p approaches p_c, the equation above simplifies to:

$$S(p) = \frac{p_c+p}{p_c-p} \rightarrow \frac{2p_c}{p_c-p} \propto (p_c-p)^{-1}$$

In 1-D percolation, as the concentration p nears the critical occupation probability p_c, the average cluster size increases indefinitely according to a power law. This behavior is similarly observed in higher dimensions, where it is described by the critical exponent γ. The critical exponent linked to the average cluster size is defined as:

$$S(p) \propto |p_c-p|^{-\gamma}, \quad \text{for } p \rightarrow p_c \tag{5.2}$$

The correlation function, or pair connectivity, represented by $g(\mathbf{r})$, defines the probability that a site at position **r** relative to an occupied site is part of the same finite cluster. This definition specifically excludes any contributions from the infinite cluster. If we let $r = |\mathbf{r}|$, it's clear that $g(r = 0) = 1$ because the site is occupied by definition. In one dimension, for the site at position **r** to be occupied and part of the same finite cluster, this site, along with the $(r - 1)$ intermediate sites, must also be occupied. Therefore, we have:

$$\begin{aligned} g(r) &= p^r \\ &= \exp(\ln(p^r)) \\ &= \exp(r \ln p) \\ &= \exp(-\frac{r}{\xi}) \end{aligned}$$

where, ξ is the correlation length and it characterizes the linear size of finite clusters both below and above the critical probability p_c. It represents the characteristic length scale in percolation and is defined as the average distance between two sites within the same finite cluster.

$$\xi = -\frac{1}{\ln(p)} = -\frac{1}{\ln(p_c - (p_c - p))} \to \frac{1}{(p_c - p)} = (p_c - p)^{-1} \quad \text{for } p \to p_c$$

This divergence is also observed in higher dimensions and is governed by the critical exponent ν. The critical exponent related to the correlation length ξ is defined as:

$$\xi \propto |p_c - p|^{-\nu}, \quad \text{for } p \to p_c \tag{5.3}$$

In 1-D, the correlation length ξ is equal to the length scale associated with the cluster size distribution, s_ξ, such that $s_\xi = \xi$. However, in higher dimensions, these quantities are related by $s_\xi \propto \xi^{d_f}$, where d_f denotes the fractal dimension. By summing over all possible distances

r of the correlation function, the average cluster size can be expressed as:

$$\sum_{\mathbf{r}} g(\mathbf{r}) = S(p)$$

Then the correlation length ξ is defined as,

$$\xi^2 = \frac{\sum_{\mathbf{r}} r^2 g(\mathbf{r})}{\sum_{\mathbf{r}} g(\mathbf{r})}$$

For a given s-cluster, $2R_{gs}^2$ denotes the mean squared distance between any two sites within the cluster. The probability that a site belongs to an s-cluster is $sn_s(p)$, and it is connected to s sites. Taking the average of $2R_{gs}^2$ gives the squared correlation length:

$$\xi^2 = \frac{2\sum_s R_{gs}^2 s^2 n_s(p)}{\sum_s s^2 n_s(p)} \tag{5.4}$$

Here, R_{gs} refers to the radius of gyration of a cluster of size s, which represents the average distance between two sites within the cluster. It is defined as:

$$R_{gs}^2 = \frac{1}{s}\sum_{i=1}^{s} |\mathbf{r}_i - \mathbf{r}_{cm}|^2 = \frac{1}{2}\frac{1}{s^2}\sum_{ij} |\mathbf{r}_i - \mathbf{r}_j|^2 \tag{5.5}$$

In this context, $\mathbf{r}_i$ and $\mathbf{r}_j$ represent the positions of the i^{th} and j^{th} occupied sites within a cluster of size s. Moreover, the radius of gyration R_{gs} is associated with the cluster size s as follows:

$$s \propto R_{gs}^{d_f}, \quad \text{for } s \gg 1 \quad \text{at } p = p_c \tag{5.6}$$

Where, d_f represents the fractal dimension. Near p_c, both the infinite cluster and the finite clusters exhibit self-similarity on length scales smaller than ξ. Above p_c, the infinite percolating cluster becomes compact on length scales larger than ξ, while below this scale, the cluster maintains a fractal, self-similar structure. This non-trivial self-similarity at scales smaller than ξ is characterized by the fractal dimension d_f. Let $M(r)$ represent the average mass of the percolating cluster within a circle of radius r, which scales with r as $M(r) \sim r^{d_f}$, reflecting the fractal dimension d_f. Assuming $s \sim R_{gs}^{d_f}$ without loss of generality, we can express this relationship as:

$$s = \begin{cases} R_{gs}^{d_f} & \text{if } R_{gs} \ll \xi \\ R_{gs}^{D} & \text{if } R_{gs} \gg \xi \end{cases} \tag{5.7}$$

Thus, the 1-D lattice model serves as a foundational framework for analyzing key quantities and concepts such as cluster size distribution $n_s(p)$, average cluster size $S(p)$, correlation length ξ, and radius of gyration R_{gs}, as well as their associated critical exponents τ, γ, ν, and d_f during the percolation transition. This framework remains valid even in higher dimensions with minor modifications.

5.3 Percolation in gelation: necessary but not sufficient condition

Gelation is the process by which a liquid transforms into a solid-like mass, forming a three-dimensional network structure. This structure is created when particles such as monomers or biological macromolecules is suspended in a liquid which aggregate under specific conditions and results in a gel. The properties of a gel can vary widely, from soft to solid like viscoelastic behavior where elastic properties dominate over viscous ones, depending on its constituents and the gelation process. Although percolation transition is a key to understand gelation and network formation. However, it is only a necessary condition, not sufficient to fully describe gelation [8]. Gelation is classified into two types, the first one is Chemical gelation that involves the cross-linking of polymers to form an infinite network with a finite shear modulus and infinite zero shear viscosity, meaning it ceases to flow. Epoxy resins is one of the example of this process, where polymer chains interconnect through cross-linkers, creating irreversible bonds. In contrast, physical gelation occurs through the formation of gel networks via reversible bonds, driven by physical interactions comparable to thermal energy (k_BT). These bonds can repeatedly break and reform during an experiment, resulting in transient gel networks. Examples include colloid-polymer systems, where bonds arise from depletion interactions. In chemical gelation, the gel point coincides exactly with the formation of an infinite spanning network, making percolation theory an ideal framework to describe this irreversible transformation. However, in systems with transient physical bonds, percolation theory only captures static connectivity properties and fails to consider the dynamic nature of bond breakage and reformation.

Here are some studies that utilize the percolation transition to explore and understand the gelation process in colloidal systems. For instance, study by Rouwhorst et al. [112] has shown that gelation in systems with moderate particle density and short-range attractive interactions that is driven by a non-equilibrium percolation process. This process gives critical exponents similar to those found in standard 3-D percolation. The term ”non-equilibrium” arises because the detailed balance between particle aggregation and fragmentation is broken, leading to the formation of structures that are far from equilibrium. To study the onset of gelation, they have used the evolution of the average coordination number as an order parameter, which represents the average number of bonded neighbors of a particle in the system. They also confirmed the pre-gelation and post-gelation processes through kinetic theory, considering single-particle thermal detachment. Images shown in Fig. 5.3(a)-(c) in their study illustrates the time evolution of gel formation, with the largest cluster highlighted in red that shows the emergence of percolating networks in the system.

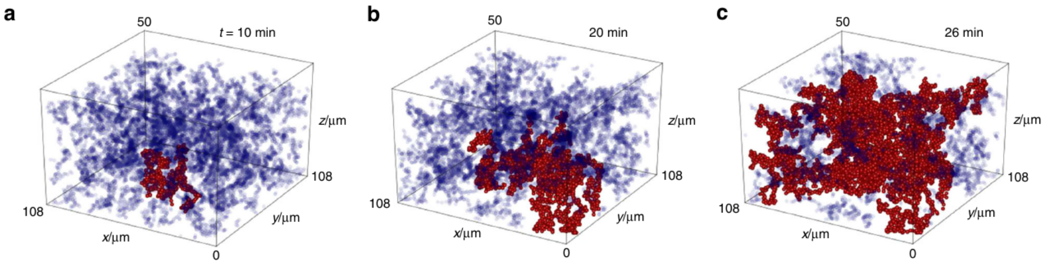

Figure 5.3: The time evolution of gel formation in experiment. The largest connected cluster is marked in red. Image taken from: [112].

In a study by M. Kohl et al., [169] gel formation is shown to be preceded by two distinct percolation processes: continuous percolation and directed percolation. Both transitions result in the formation of system-spanning networks, but only directed percolation is associated with significantly slower dynamics, aging effects, and gel shrinkage. Continuous percolation allows paths within the percolating cluster to include steps in all directions, including backward steps, whereas directed percolation strictly prohibits backward steps in any chosen direction, as illustrated in Fig. 5.4(a). The researchers adjusted the interaction strength between colloids by varying the salt concentration (Path A) to modify the range of repulsion and the polymer concentration (Path B) to change the attractive strength. They also analyzed the distribution $p(\phi)$ of angles between successive bonds ϕ, depicted in Fig. 5.4(b). At large potential depths, a peak at $\phi = \pi$ indicates the formation of straight strings of connected particles. The findings suggest that in colloid-polymer mixtures with both attractive and repulsive interactions, the transition to gel states is primarily governed by directed percolation rather than continuous percolation.

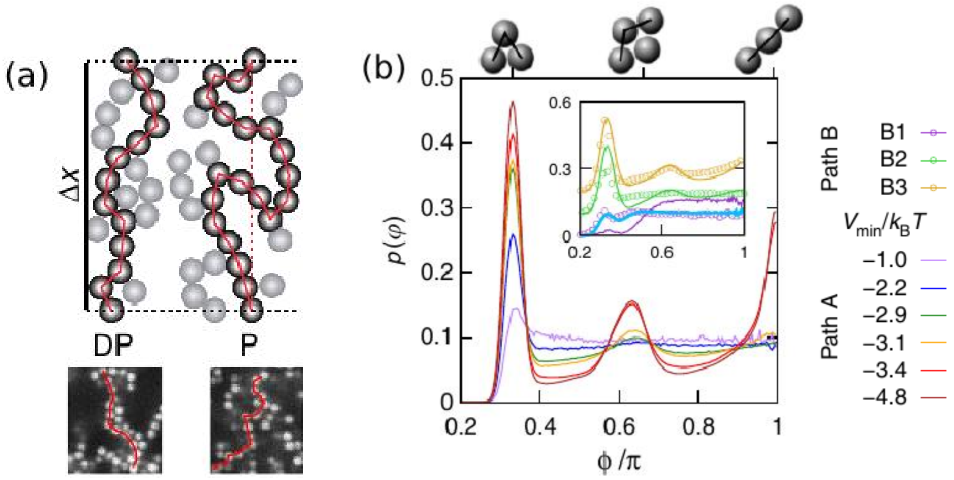

Figure 5.4: (a) A two-dimensional illustration alongside experimental images depicting clusters formed by directed percolation (DP) and continuous percolation (P), each with a length of Δx. (b) Simulation results showing the distribution of angles between successive bonds along Path A. The inset compares simulation data (lines) and experimental data (circles) for the angle distribution along Path B. Images has been taken from [169].

H. Tsurusawa et al. [168] investigated the factors contributing to mechanical stability during gelation. They found that mechanical stability is achieved only after isotropic percolation of isostatic particles, which directly correlates with the load-bearing capacity of gel. In this context, isostatic particles are those with at least six bonded neighbors in a

3-D space, and isotropic percolation refers to the formation of a system-spanning network that includes all particles. They suggest that the gelation pathway is not universal and varies based on the colloid volume fraction. In dilute systems, mechanical stability is reached when both directed percolation of all particles and isotropic percolation of isostatic particles occur simultaneously. While in dense systems, mechanical stability and isotropic percolation of isostatic particles coincide, but directed percolation of all particles happens well before mechanical stability. In dilute systems, isotropic percolation is delayed, starting with the formation of fractal clusters that eventually compact to form an isostatic structure, which then connects into a percolation network, as shown in Fig. 5.5(A). In dense systems, isostatic structures form after directed percolation, illustrated in Fig. 5.5(B). The study concludes that the fundamental mechanism behind mechanical solidity is the isotropic percolation of isostatic structures, rather than isotropic or directed percolation alone.

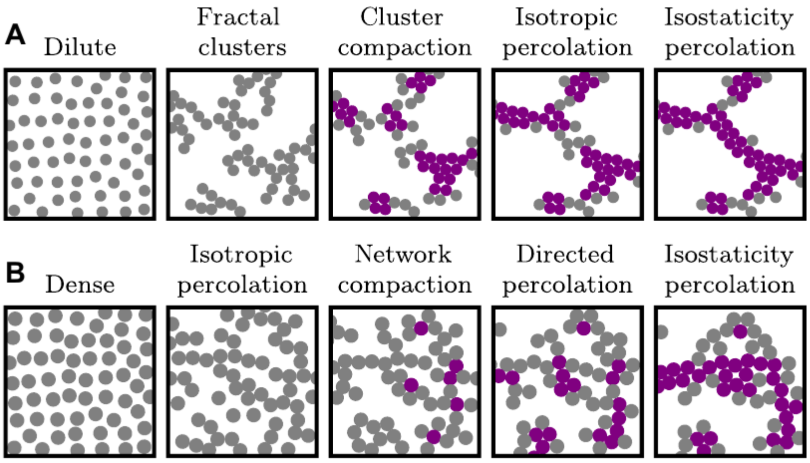

Figure 5.5: Diagram illustrating the two possible routes to achieving a mechanically stable gel. (A) The dilute path. (B) The dense path. Particles that are isostatic are depicted in purple, while non-isostatic particles are shown in gray. Image taken from: [168].

So far, we have explored the gelation process in systems with passive particles. However, introducing active agents into the system raises questions about the potential states and properties that may emerge. To address this, D. Grober et al. [159] investigated colloidal aggregation in a chiral bacterial bath, leading to the formation of unconventional clusters and gel states characterized by the persistent rotation of aggregates. They introduced sticky colloids, created through the irreversible binding of colloids with added polymer, into the chiral bacterial bath, resulting in more compact aggregates with cavities compared to their thermal counterparts, which showed ramified aggregates (see Fig. 5.6(a)). To investigate the mechanical properties of these active gels, the researchers conducted numerical measurements of stress and strain by mechanically probing passive gels infused with internal activity. Their findings revealed that gels formed in a thermal bath exhibited linear and symmetric responses, characteristic of elastic solids. However, gels formed via active aggregation showed markedly nonlinear elastic behavior when compressed and demonstrated increased stiffness during extension, as illustrated in Fig. 5.6(b).

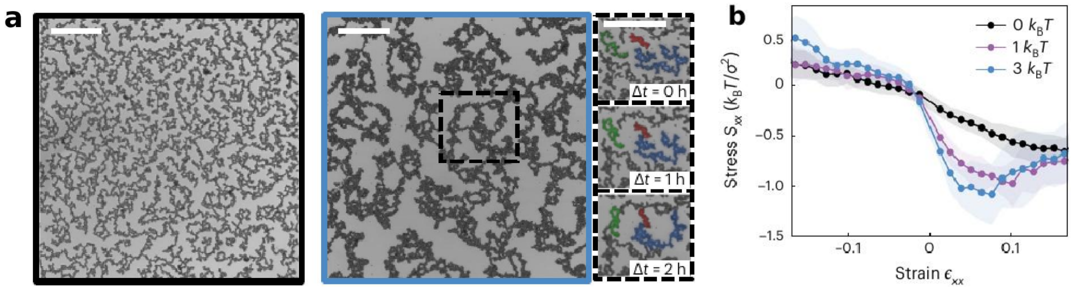

Figure 5.6: (a) Bright-field images of a 2D colloidal gel formed in a thermal bath and (b) in an active bath. The inset in (b) presents time-lapse micrographs capturing the formation of large heterogeneities due to the rotation and jamming of large aggregates. Scale bar: $200\mu m$. (c) Stress-strain curves comparing passive gels (black) and active gels, with the curve color indicating the internal torque amplitude: 1 k_BT (purple) and 3 k_BT (blue). Image adapted from [159].

5.4 Experimental set-up

In our study, the active-passive mixture is realized by dispersing polystyrene beads of size $15\mu m$ in active suspensions of E. coli. The procedure for preparing the active fluid is detailed in Section 2.3. Throughout our experiments, we maintained a constant bacterial density equivalent to $10b_0$, where $b_0 = 6 \times 10^9$ cells/ml, unless specified explicitly. To investigate the percolation transition, we systematically varied the colloidal area-fraction from $\phi = 0.1 - 0.6$. The colloidal beads used in our study are sufficiently large, which makes the

Brownian fluctuations negligible. The dynamic behavior of colloidal beads within the active fluid is exclusively driven by the inherent activity of the fluid medium and their hydrodynamic interactions [90, 114]. To facilitate our measurements, we constructed an observation chamber by affixing a circular cavity of 1 cm in diameter and 100 μm in depth to a coverslip coated with polyethylene glycol (PEG), using double-sided tape. A sketch of the sample chamber is shown in Fig. 2.4.

For experimentation, we thoroughly mixed the active fluid and colloidal particles before introducing them into the sample chamber, which was subsequently mounted on the microscope stage. Following the loading procedure, we allowed the system to sediment, evolve and, equilibrate for a duration of 1.5 hours before commencing our measurements. All the measurements were made in the stationary state, we captured snapshots of the sample at a speed of 10 FPS over a total duration of 500 seconds.

5.5 Results

5.5.1 Chiral active liquids and chiral colloidal assemblies

The experiments detailed in this article are conducted close to the lower boundary of the chamber, specifically at the solid-liquid interface. It is well-established that E. coli breaks its chiral symmetry while swimming near a boundary, resulting in curved trajectories displaying clockwise rotation [38, 181–183], also see the sec 1.3.2 and Fig. 5.7(a) showing the clockwise curved trajectories shown in yellow and instantaneous position of bacteria marked in red circles. The scale bar measures 20 μm. The colloidal particles employed in our investigation are $15\mu m$ in size and are about 5 times larger compared to the size of bacteria, so they experience a net torque due to interactions with bacteria, thereby breaking their chiral symmetry as well [159, 164, 165]. The individual particles and their cluster show persistent rotation in clockwise direction because they experience a net torque in the clockwise direction, which is due to the inherent chirality of the bacteria at the solid-liquid interface, where the bacteria themselves rotate clockwise. The clockwise rotation of individual colloidal particle can be

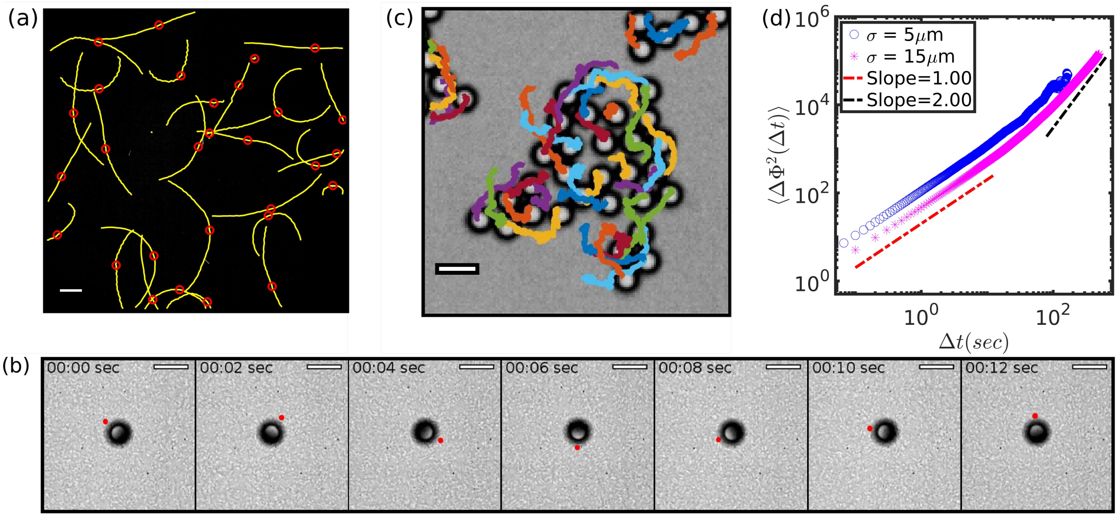

Figure 5.7: Broken chiral symmetry of colloidal clusters.(a) Clockwise circular trajectories of bacteria, highlighted in yellow curves, with the instantaneous position of bacteria marked in red circles. Scale bar: 20 μm. (b) Various time stamps depicting clockwise spinning Janus particle, with a red dot indicating the position over time. Scale bar: 30 μm.(c) Persistent rotation of colloidal clusters are shown by overlapping the particles and their trajectories using different colors. Scale bar: 20μm.(d) Mean square angular displacement $\langle\Delta\Phi^2(\Delta t)\rangle$ for 5μm, and 15μm particle size, red and black dashed lines with slope = 1 and 2, respectively, are shown for reference.

visualised by suspending a Janus or half coated particle in the chiral bath as shown in the various time stamps in Fig. 5.7(b). The red dot indicates the instantaneous directed location of rotated particle. Furthermore, the activity of swimmers and hydrodynamics facilitate interactions between colloidal particles, resulting in an attractive effective interaction. This interaction leads to the formation of dynamic clusters [63, 68], which show persistent rotations. To illustrate the rotational motion, we have plotted the trajectories of a few colloidal particles in Fig. 5.7(c), where the chiral motion is evident from the curved trajectories. We further compute their mean square angular displacement, which is an angular analogue of the mean square displacement. The unbounded mean square angular displacement is defined as [7]:

$$\langle\Delta\Phi^2(\Delta t)\rangle = \langle[\Phi(t+\Delta t) - \Phi(t)]^2\rangle, \tag{5.8}$$

where $\Phi(t) = (1/2\pi)\int_0^t \Delta\theta(t')dt'$ is the total angular displacement that is integrated over the instantaneous angular displacements $\Delta\theta(t)$. The results are depicted in Fig. 5.7(d) for different sizes of colloidal particles $\sigma = 5\ \mu m$ and $15\ \mu m$ at a bacterial density of $10b_0$. The observed angular motion of particles reveals diffusive characteristics with a slope approaching 1 at short time intervals. However, over larger time scales, the larger particles clearly exhibit a persistent angular rotation, characterized by a slope nearing 2. This effect is prominent for larger ($15\mu m$) particles, compared to the smaller ones ($5\mu m$) that show super-diffusive chiral motion on measurement time scales. This chiral motion of colloidal particles and bacteria leads to interesting features as the clusters grow and percolate at a critical area-fraction of colloids.

5.5.2 Clusters of colloidal particles

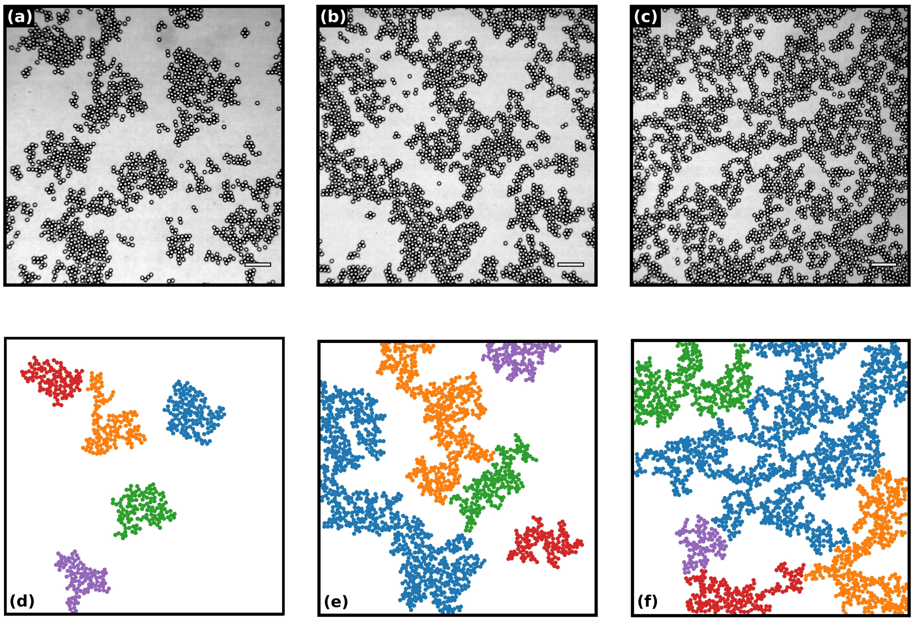

Figure 5.8: Percolation of colloidal clusters. Panels (a)-(c) : Bright field images of the colloids in active liquid of E. coli at (a) ϕ = 0.2, (b) ϕ = 0.3, and (c) ϕ = 0.4. The scale bar shown in the images is $100\mu m$. Panels (d) - (f) : First five largest clusters in the bright-field images shown in the panels (a) - (c). Blue, orange, green, red, and violet are the colors of first to fifth largest cluster, respectively.

We next display the bright-field images of colloidal assemblies in active liquids in Fig.

5.8. The panels Figs. 5.8(a)-(c) correspond to several area-fractions of colloids with $\phi = 0.2, 0.3$, and 0.4, respectively. The scale bar in these images measures 100 μm. This is reminiscent of the sol-gel transition in colloidal suspensions with attractive interactions [167]. The clusters at $\phi = 0.2$ in Fig. 5.8(a) appear to be compact and isolated. However, as ϕ increases, the clusters grow in size and become ramified, eventually spanning the entire field of view. To further illuminate these observations, we identified clusters from the particles' coordinates by adopting a fixed cutoff distance for connected particles. This threshold is set at 1.2σ, based on the first minima of the pair correlation function g(r). The results of this analysis are shown in Figs. 5.8(d)-(f), which depict the first five largest clusters of Figs. 5.8(a)-(c), respectively. In these images, the colors blue, orange, green, red, and violet correspond to the first to fifth largest clusters, respectively. The Figs. 5.8(d)-(f) provide better insights into the evolution of these clusters with changing ϕ. The first largest cluster, depicted in blue, gradually grows with increasing ϕ and becomes increasingly ramified with a fractal-like structure. Further, the second largest cluster, shown in orange, experiences growth initially but later diminishes in size as most particles are absorbed into the first largest cluster.

5.5.3 Spanning probability and percolation threshold

As evident from the results in Fig. 5.8, an increase in the area fraction ϕ leads to the growth of the first largest cluster, which eventually spans the entire field of view. In our pursuit of investigating percolation properties, we first determine the percolation threshold, denoted as ϕ_c. To ascertain this threshold, we employed the concept of spanning probability, denoted as Π. Spanning probability is the fraction of configurations in which the clusters span in both horizontal and vertical directions for a given ϕ. This procedure is repeated at several area-fractions ϕ of colloidal particles. The critical density or the percolation threshold ϕ_c is defined as the area-fraction where the spanning probability Π attains a value of 0.5 [184, 185]. Figure 5.9(a) shows the plot of spanning probability Π as a function of ϕ. The blue diamonds represent the experimental data points, while the solid black curve is guide to the eye. Additionally, the black dashed horizontal and vertical lines gives the intersection point

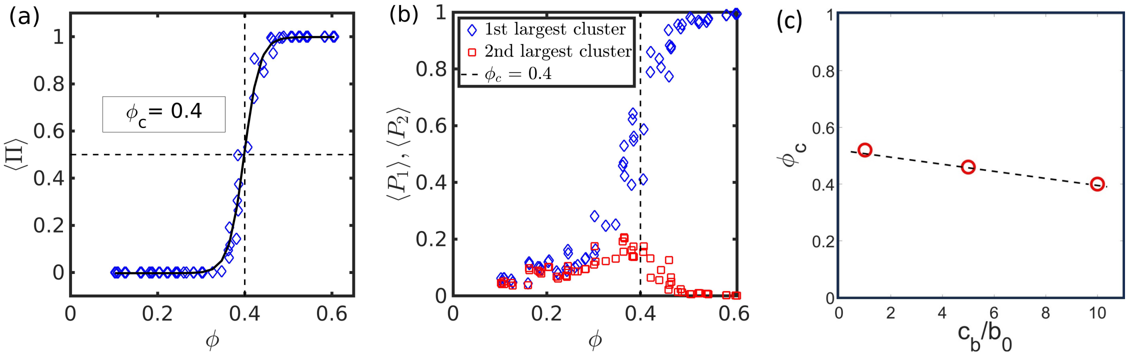

Figure 5.9: (a) The spanning probability of the clusters at area-fractions of colloidal particles ranging from $\phi = 0.1 - 0.6$ and a bacteria concentration of $10b_0$. The black curve is guide to the eye. Horizontal and vertical dashed line are drawn to indicate the percolation threshold ϕ_c=0.4 at $\Pi = 0.5$. (b) The fraction of particles in the first $\langle P_1 \rangle$ and second $\langle P_2 \rangle$ largest clusters at several area-fraction of colloids. The dashed line shows the percolation threshold $\phi_c = 0.4$. (c) Percolation density ϕ_c at varying normalised concentrations of bacteria (c_b/b_0), where $b_0 = 6 \times 10^9$cells/ml.

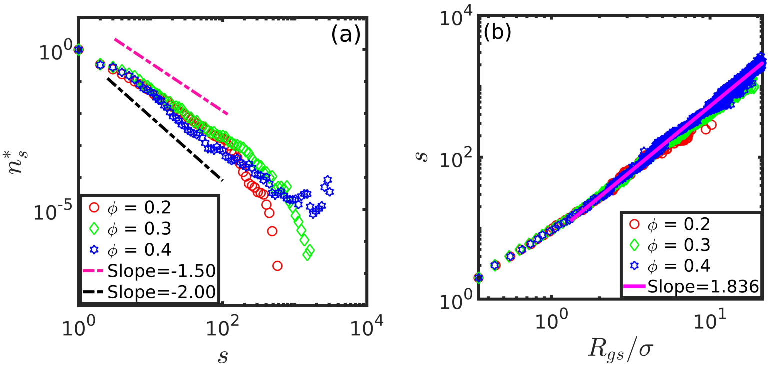

Figure 5.10: (a) Cluster size distribution n_s^* as a function of cluster size s. Magenta and black dashed line have slope -1.5 and -2, respectively. (b) The scaled radius of gyration R_{gs} of clusters of size s. The solid line is a linear fit to the curve corresponding to $\phi_c = 0.4$, which has a slope of $d_f = 1.836 \pm 0.040$ for $s > 10$.

between the spanning probability curve and the $\Pi = 0.5$ curve. From this intersection point, we determined the percolation threshold to be $\phi_c \approx 0.4$. Varying the concentration of the bacteria b_0 shifts the percolation threshold, it moves to the higher values of ϕ with decreasing concentration of swimmers. Figure 5.9(c) shows the effect of varying the concentration of swimmers on the percolation density ϕ_c. The density of bacteria used in all the measurements is $10b_0$. Here, we have varied the density of swimmers from $1b_0$ to $10b_0$. The percolation density decreases with increasing concentration of swimmers, suggesting that the clusters grow in size with increasing density of bacteria due to stronger effective interactions [68]. Moving to Fig. 5.9(b), we explore the fraction of particles in the first and second largest clusters, denoted as $\langle P_1 \rangle$ and $\langle P_2 \rangle$, respectively, as a function of ϕ. The experimental data points for $\langle P_1 \rangle$ and $\langle P_2 \rangle$ are represented by blue diamonds and red squares, respectively. The black dashed line is drawn at $\phi_c = 0.4$ to denote critical density. In Fig. 5.9(b), we observe that the fraction of particles in the first largest cluster $\langle P_1 \rangle$ increases and eventually saturates as ϕ increases. In contrast, the fraction of particles in the second largest cluster $\langle P_2 \rangle$ initially increases until ϕ_c and decreases beyond. This behavior is a signature of percolation transition, which has been used for defining ϕ_c in other studies. [112, 186].

5.5.4 Cluster size distribution and radius of gyration

The percolation transitions are associated with scale-free size distribution of clusters, with no characteristic cluster size at ϕ_c. To investigate these aspects of cluster formation in our experiments, we investigate their size distribution. The cluster size distribution denoted as n_s^* is defined as $n_s^* = n_s / \sum n_s$ where n_s is the frequency of clusters of size s.

The Fig. 5.10(a) shows the cluster size distribution n_s^* at colloidal densities of $\phi = 0.2, 0.3$, and 0.4, denoted by red circles, green diamonds, and blue hexagons, respectively. For the ease of comparison, n_s^* is scaled by n_1. The magenta and black dashed lines featuring slopes of -1.5 and -2, respectively, are included for reference. Previous studies [174, 180] and eqn. 5.1 have shown that cluster size distribution in the vicinity of percolation transition is given by the following expression:

$$n_s^* \propto s^{-\tau} \exp\left(-\frac{s}{s_\xi}\right), \text{ for } s \gg 1, \tag{5.9}$$

where s_ξ represents the cutoff length scale of cluster size, and τ denotes one of the critical exponents. The distribution n_s^* exhibits a power-law dependence with an exponential cutoff below ϕ_c, however, as ϕ approaches ϕ_c, it approaches a power-law indicating the absence of a characteristic length scale leading to $n_s^* \sim s^{-\tau}$. According to the continuum percolation theory of disks (CPT), the exponent $\tau = 2.0 \pm 0.1$ in two dimensions [175] . From Fig. 5.10(a) it is clear that for ϕ below ϕ_c, the n_s^* has nature of power law decay with exponential cutoff, as ϕ approaches to ϕ_c, it has only power-law dependence. The exponent determined from the best-fit procedure yields a value of $\tau = 1.74 \pm 0.12$ at $\phi_c \sim 0.4$, which deviates from the predictions of CPT. Interestingly, the nonequilibrium structure formation in conserved mass models with diffusion, aggregation and fragmentation displays phase transition beyond a critical density ρ_c [187]. The mean-field model predicts $n_s^*(s) \sim e^{s/s^*} s^{-3/2}$, where s is the cluster size, below ρ_c. However, at ρ_c, the cluster size distribution has a power-law form $n_s^*(s) \sim s^{-5/2}$. The inclusion of activity in such models could lead to insightful results.

We turn our attention to the morphology of the clusters. It appears from Fig. 5.8 that the clusters acquire a fractal-like structure on approach to percolation transition. This can be tested by calculating the radius of gyration R_{gs} and the associated fractal dimension d_f. The radius of gyration, R_{gs}, from the Eq. 5.5 is defined as [174]:

$$R_{gs}^2 = \frac{1}{2s^2} \sum_{ij} |\mathbf{r}_i - \mathbf{r}_j|^2, \tag{5.10}$$

where $\mathbf{r}_i$ and $\mathbf{r}_j$ represent position vectors of particles within a cluster of size s [174, 180]. Near the percolation threshold, the cluster size s is connected to the radius of gyration by the relation 5.6:

$$s \sim R_{gs}^{d_f}, \qquad (\text{for } \phi = \phi_c, s \gg 1), \tag{5.11}$$

where d_f is the fractal dimension. For a two-dimensional system, the $d_f = 1.894 \pm 0.003$ from the CPT [188]. The data in Fig. 5.10(b) shows the relation between the radius of gyration and cluster sizes. The red circles, green diamonds, and blue hexagons represent data points for $\phi = 0.2, 0.3$, and 0.4, respectively. The magenta solid line corresponds to the fitting of R_{gs} at $\phi_c = 0.4$ for $s > 10$, and the slope of the fitted curve gives $d_f = 1.836 \pm 0.040$, which appears to be in close agreement with the continuum percolation model [188].

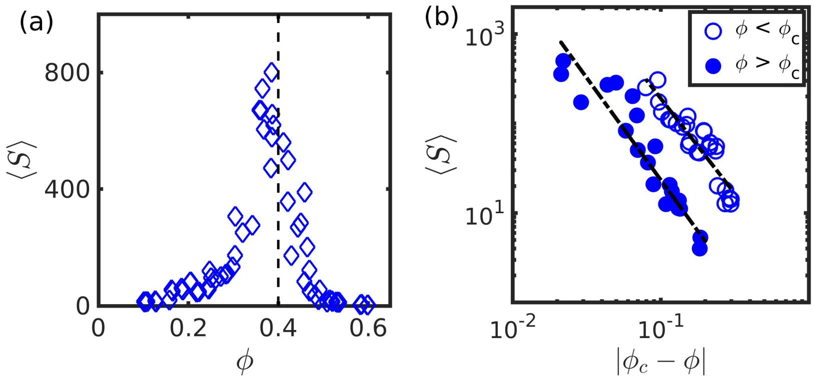

Figure 5.11: (a) The mean cluster size $\langle S \rangle$ of colloidal particles as a function of its area-fraction ϕ. Black dashed line indicate $\phi_c = 0.4$. (b) $\langle S \rangle$ as a function of $|\phi_c - \phi|$ for $\phi < \phi_c$ (open circles) and $\phi > \phi_c$ (filled circles). The slope of the best fit line for $\phi < \phi_c$ (open circles) is $\gamma = 2.13 \pm 0.16$ and for $\phi > \phi_c$ (filled circles) it is $\gamma = 2.28 \pm 0.23$.

5.5.5 Average cluster size $\langle S \rangle$ and correlation length $\langle \xi \rangle$ of clusters

We proceed further with the analysis of other quantities to establish the nature of percolation transition observed in our experiments. In equilibrium systems quantities like average cluster size $\langle S \rangle$ and correlation length $\langle \xi \rangle$ exhibit power-law scaling with the distance from the critical point. The average cluster size obeys the following relation, Eq. 5.2, in the the vicinity of the critical point [174]:

$$\langle S \rangle \propto |\phi - \phi_c|^{-\gamma}, \qquad \qquad \phi \to \phi_c \tag{5.12}$$

where γ is the critical exponent associated with $\langle S \rangle$. The CPT predicts $\gamma = 2.43 \pm 0.04$ for two-dimensional (2D) systems [175]. The $\langle S \rangle$ is defined as the second moment of cluster size distribution n_s^* and is give by the following equation [174]:

$$\langle S \rangle = \frac{\sum_s' s^2 n_s}{\sum_s' s n_s}. \tag{5.13}$$

In the above equation, s represents the size of individual clusters, and n_s denotes the frequency of clusters with size s. The notation $\sum'$ signifies that the summation excludes contributions from the spanning cluster. The variation of $\langle S \rangle$ with changing area-fraction of

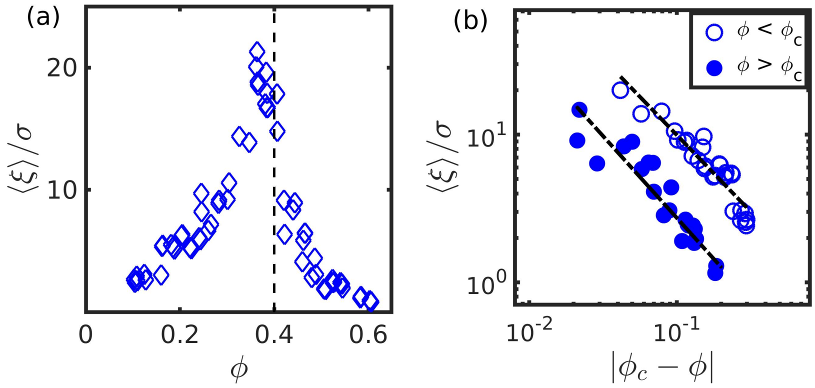

Figure 5.12: (a) Correlation length $\langle\xi\rangle$ of the clusters of colloidal particles as a function of its area-fraction ϕ. Black dashed line denotes the percolation threshold $\phi_c = 0.4$. (b) The plot of $\langle\xi\rangle$ as a function of $|\phi_c - \phi|$ for $\phi < \phi_c$ (open circles) and $\phi > \phi_c$ (filled circles). The slope of the best fit line for $\phi < \phi_c$ (open circles) is $\nu = 1.035 \pm 0.087$ and for $\phi > \phi_c$ (filled circles) it is $\nu = 1.108 \pm 0.123$.

colloids across ϕ_c is shown in Fig. 5.11(a). It is important to note that our calculations exclude contributions from spanning clusters, focusing on the behavior of finite-sized clusters. It illustrates a familiar trend close to the critical point. Initially, $\langle S\rangle$ increases as ϕ approaches the critical point ϕ_c and it decreases beyond ϕ_c. The Fig. 5.11(b) shows the variation of $\langle S\rangle$ as a distance from the critical point $|\phi - \phi_c|$ on a double logarithmic scale. The open circles correspond to $\phi < \phi_c$ and filled circles correspond to $\phi > \phi_c$. The slopes of best-fit lines to the data yields $\gamma = 2.13 \pm 0.16$ when $\phi < \phi_c$ and the slope is $\gamma = 2.28 \pm 0.23$ for $\phi > \phi_c$. In conclusion, our analysis reveals that the critical exponent γ associated with $\langle S\rangle$ show deviations from the standard percolation models [175].

Along with $\langle S\rangle$, the equilibrium correlation length $\langle\xi\rangle$ of the clusters is known to obey a scaling relation described by the following Eq. 5.3 [174]:

$$\langle\xi\rangle \propto |\phi - \phi_c|^{-\nu}, \qquad \phi \to \phi_c \tag{5.14}$$

where the critical exponent $\nu = 1.343 \pm 0.019$ for a two dimensional system [175]. The

Exponents	Lattice percolation	Continuum percolation	Experimental results
β	0.139	0.14 ± 0.02	-
γ	2.389	2.43 ± 0.04	2.28 ± 0.23
ν	1.333	1.343 ± 0.019	1.108 ± 0.103
τ	2.055	2.0 ± 0.1	1.74 ± 0.12
d_f	1.896	1.894 ± 0.003	1.836 ± 0.040

Table 5.1: The values of critical exponents for random lattice percolation and continuum percolation in 2-D. These values has been taken from [174, 175, 188].

correlation length $\langle \xi \rangle$ is calculated using the Eq. 5.4 [174]:

$$\xi^2 = \frac{2\sum_s' R_{gs}^2 s^2 n_s}{\sum_s' s^2 n_s} \tag{5.15}$$

where R_{gs} represents the radius of gyration of clusters containing s-particles, and n_s denotes the frequency of clusters with size s. Similar to previous definitions, the primed sum excludes contributions from the spanning cluster. The analysis of $\langle \xi \rangle$ in our experiments at various densities of colloids in Fig. 5.12(a) reveals a similar trend as $\langle S \rangle$, in the neighborhood of ϕ_c. We can gain a better understanding by presenting the data on a double logarithmic plots in Fig. 5.12(b). The data in Fig. 5.12(b) shows the variation of $\langle \xi \rangle$ as a function of distance from the critical point $|\phi_c - \phi|$. The open circles correspond to $\phi < \phi_c$ and filled circles correspond to $\phi > \phi_c$. The slopes of best-fit lines to the data yields $\nu = 1.035 \pm 0.087$ when $\phi < \phi_c$ and the slope is $\nu = 1.108 \pm 0.123$ for $\phi > \phi_c$. The exponents ν on both the sides of ϕ_c is far from the standard continuum model. The list of critical exponents of Random lattice model, continuum model, and our Experimental results are given below in the Table 5.1.

The results from our analysis of cluster sizes distribution n_s^*, average cluster size $\langle S \rangle$, and correlation length $\langle \xi \rangle$ reveal that their respective exponents τ, γ, and ν show deviations from the standard exponents predicted by continuum percolation theory for 2D equilibrium systems. The exponents reported here could have finite size effects and in addition it is difficult to accurately pinpoint the critical density in experiments. Our results motivate novel theoretical models and simulations to determine the true values of exponents. Our current

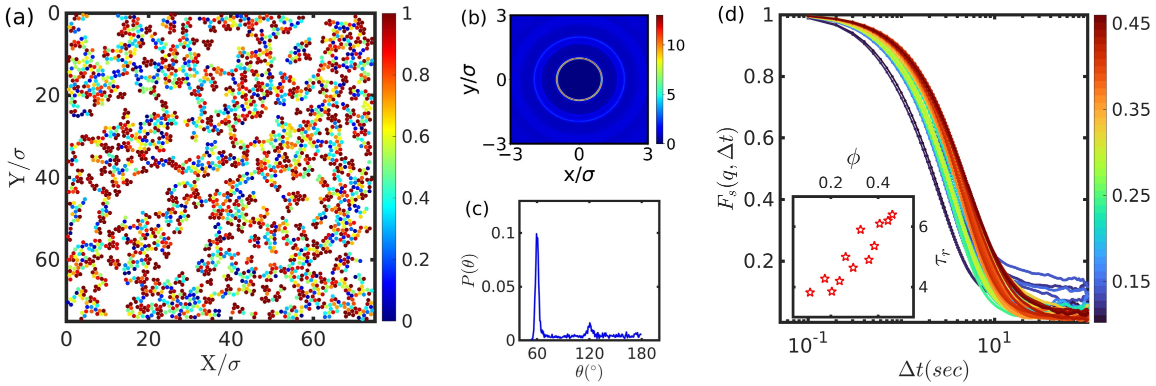

Figure 5.13: Structure of the clusters at the colloidal area-fraction of $\phi_c = 0.4$. (a) Local bond-orientational-order parameter ψ_6 of individual particles is color-coded based on its magnitudes. (b) The two dimensional pair-correlation function $g(x, y)$ of colloidal assemblies. The color indicates the magnitude of $g(x, y)$. (c)The distribution of angle $P(\theta)$ between two successive bonds. (d) The intermediate scattering function $F_s(q, \Delta t)$ of the system at several area-fractions of the system ranging from $\phi = 0.1 - 0.4$ is shown in the main panel. The color of the curve indicates the area-fraction of system. Inset : the relaxation time scales τ extracted from the decay of $F_s(q, \Delta t)$ in the main panel is presented as function of the area-fraction of colloids.

results appear to support recent numerical studies on percolation transition in purely active particle systems [171, 173] that have reported critical exponents deviating from standard percolation models, hinting at a new universality class of percolation model for active systems. Note that the one of simulation models [171] considers 3D systems and includes the effect of hydrodynamic interactions, whereas the other model [173] studies 2D dry systems. A confirmation of these observation needs further investigation into these aspects.

5.6 Effect of chiral swimmers on the structure of clusters

5.6.1 Structure of clusters in colloid-bacteria mixture

In this section, we discuss the influence of chirality on the organization of colloids within the clusters. To elucidate this effect, we analyze the microscopic structure of clusters using conventional structural measures such as the local bond orientational order parameter and the pair correlation function. The local bond orientational order parameter is defined as:

$$\psi_6 = \frac{1}{N_j}\sum_{j=1}^{N_j} \exp(6i\theta_{ij}), \tag{5.16}$$

where θ_{ij} is the orientation of the link connecting the two neighboring particles (i, j), and the sum runs over N_j nearest neighboring particles within a cutoff distance of 1.2σ. Figure 5.13(a) presents the local ψ_6 at the percolation threshold ϕ_c, where the color coding is based on the ψ_6 values of the particles. This plot reveals weak orientational ordering of particles in the clusters, further confirmed by the polar plot of the pair correlation function in Fig. 5.13(b). The two-dimensional pair correlation g(x,y) is defined as [113]

$$g(x, y) = \frac{1}{\rho}\left\langle \sum_{j\neq i} \delta\left[x\hat{x}_i + y\hat{y}_i - (\mathbf{r}_i - \mathbf{r}_j)\right] \right\rangle_i , \tag{5.17}$$

where δ is a Dirac delta function, $\rho = \frac{N_{\text{total}}}{A}$ is the area density, $\langle \ldots \rangle_i$ represents the average over all reference particles i. The plot of $g(x, y)$ demonstrates a liquid-like isotropic structure of the system. We next display the distribution of angles $P(\theta)$ between two successive bonds [169] in Fig. 5.13(c). The plot shows $P(\theta)$ with a prominent peak at $\theta = \frac{\pi}{3}$ and a small one at $\theta = \frac{2\pi}{3}$. These results are robust and persist over a range of densities ϕ and bacteria concentration. They are illuminating when interpreted in light of our understanding of equilibrium colloid-polymer mixtures [14, 166]. Figs. 5.14(a)-(c) depict the ordering of colloids within clusters of colloid-polymer mixture. The presence of prominent peaks in these plots points to strong directional ordering, which is reported to be responsible for directed percolation transition in colloid-polymer mixtures [169, 170, 189]. Apparently, the weak structural ordering in colloid-bacteria mixture is a result of activity and chirality of the swimmers, which alter the nature of the percolation transition. It also impacts the timescales of structural relaxation, which is measured using the intermediate scattering function, defined by the following equation:

$$F_s(q, \Delta t) = \frac{1}{N} \sum_{i=1}^{N} e^{(-j\mathbf{q}\cdot\Delta\mathbf{r}(t))}, \tag{5.18}$$

where $q = 2\pi/\sigma$. The results for colloid-bacteria mixture are shown in Fig. 5.13(d), where $F_s(q, \Delta t)$ is plotted at several area-fractions of colloids. The timescales τ extracted from the $1/e$ decay of the curves are shown in the inset of Fig. 5.13(d). It is evident from the plot that the increase in relaxation timescale on approaching the percolation threshold is nominal. The presence of activity and persistent rotations leads to constant restructuring of the network even in the vicinity of ϕ_c. This suggests that the lifetime of the bond between the particles is short, which interrupts the formation of gels. These results are reminiscent of thermal gels where the bond lifetimes are crucial for gelation. [167]. However, the persistent rotations lead to distinct percolation transition in colloid-bacteria mixtures. This raise interesting questions regarding structural arrest, emergence of rigidity, and the viscoelastic properties of active-passive mixtures.

5.6.2 Structure of clusters in colloid-polymer mixture

In this section, we investigate the structure of clusters in a colloid-polymer mixture, which was prepared utilizing silica beads of diameter of 3.34 μm and sodium polystyrene sulfonate (NaPSS) polymer of molecular weight 10^6 Da. The preparation involved two distinct polymer concentrations, namely $c_p = 0.1\%$ and 0.01%, both suspended in deionized (DI) water. The particles sediment to the bottom to form a monolayer of particles, which is evidenced from their gravitational length l. For our silica beads, it turns out to be $l \sim 0.02\mu m$, which is much smaller than the size of the particle [190].

The Fig. 5.14(a) depicts the local bond orientational order parameter (ψ_6) for a polymer concentration of $c_p = 0.01\%$ and a colloidal area-fraction of $\phi = 0.40$, where the colors illustrates the magnitude of ψ_6. Additionally, the Fig. 5.14(b) presents the two-dimensional pair correlation with the color indicating the magnitude of g(x,y) at same c_p and ϕ. The local

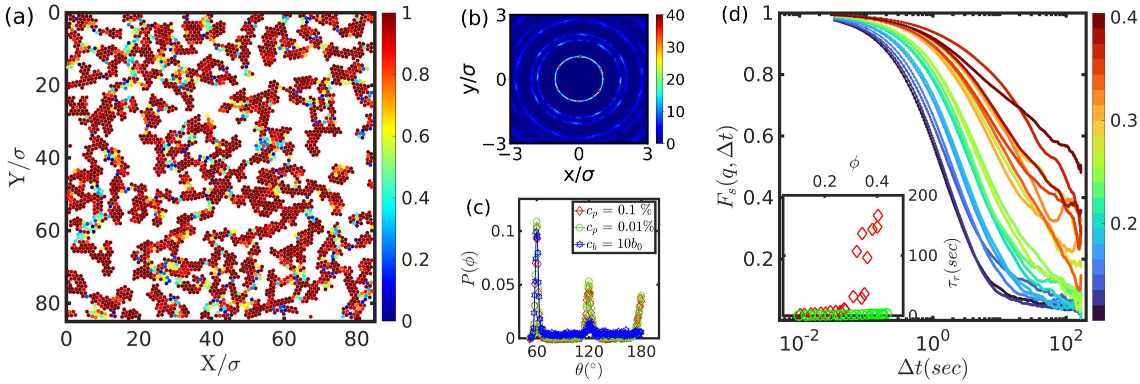

Figure 5.14: Structure of clusters in colloid-polymer mixture at a colloid area-fraction of $\phi = 0.40$. (a) The particles are color coded based on the magnitude of their local bond-orientational-order parameter (ψ_6). (b) Polar representation of pair-correlation function g(x,y) of colloid-polymer mixture. The color represents the magnitude of g(x,y). The polymer concentration in (a) and (b) is $c_p = 0.01\%$. (c)The distribution of angle $P(\theta)$ for two different polymer concentrations, $c_p = 0.1\%$ and 0.01%, for colloid-polymer mixture, and $c_b = 10b_0$ for colloid-bacteria system at $\phi_c = 0.4$. (d) The intermediate scattering fraction for $c_p = 0.1\%$ across various area fractions, with the color bar denoting the area fraction range from 0.1 to 0.4. Inset: The relaxation time of colloids for the colloid-polymer system (red dimonds) and colloid-bacteria system(green circles).

ordering of colloidal particles is evident from the results in these two figures. There is a strong hexatic ordering in Fig. 5.14(a), while Fig. 5.14(b) shows distinct peaks in the first two inner rings corresponding to hexagonal symmetry. Fig. 5.14(c) shows the distribution of angles $P(\theta)$ between two successive bonds [169] for two different polymer concentrations, $c_p = 0.1\%$ and 0.01%, at $\phi = 0.4$, respectively. This analysis also includes the colloid-bacteria mixture at a cell concentration of $c_b = 10b_0$ and a colloidal area-fraction of $\phi = 0.4$. The $P(\theta)$ curve displays a prominent peak at $\frac{\pi}{3}$, along with enhanced peaks at $\frac{2\pi}{3}$ and π. Apparently, such directional ordering is absent in the clusters of colloidal-bacteria system. In Fig. 5.14(d), In the main panel, the intermediate scattering function $F_s(q, \Delta t)$ is presented for $c_p = 0.1\%$ across various area-fractions, with the color bar denoting the area-fraction ranging from $\phi = 0.1$ to 0.4. Inset displays the relaxation time of colloids as a function of area-fraction for the colloid-polymer system at $c_p = 0.1\%$ and $c_b = 10b_0$ for colloid-bacteria system. The relaxation times were obtained from the (1/e) decay of $F_s(q, \Delta t)$. The colloid-polymer system at $c_p = 0.1\%$ displays a strong nonlinear increase in relaxation time. The timescales derived from $F_s(q, \Delta t)$ can also be considered as representative of the bond life times. The ordering observed in colloid-polymer mixtures appears to be a persistent feature, which is absent in colloid-bacteria mixtures.

5.6.3 The relaxation time-scale of the largest cluster

The relaxation time calculated from ISF gives the relaxation time of individual particles. To quantify the time scale of long lived clusters, we estimate the relaxation time of the largest cluster. This is done by calculating the time needed for the largest cluster to lose 50% of the original particles. Denoting the number of particles in the largest cluster at time $t = 0$ as $N_l(0)$ and the number of original particles that persist in the largest cluster after a time interval t as $N_l(t)$ as shown for three different ϕ in Fig. 5.15(a). The variation of the ratio $N_l(t)/N_l(0)$ with time is illustrated above in Fig. 5.15(b) at several densities of colloidal particles. The dashed line is drawn at $N_l(t)/N_l(0) = 0.5$. The crossing of this line by the curves is considered relaxation time of the largest cluster. The Fig.S2(b) shows the relaxation timescale at varying densities of colloids ϕ. The dotted line shows an exponential fit to the data.

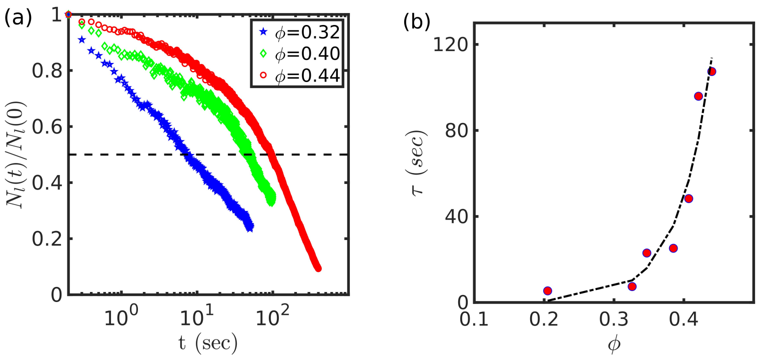

Figure 5.15: The relaxation time-scale of the largest cluster. (a) The number of original particles in the largest cluster after a time interval t. $N_l(0)$ is number of particles in the largest cluster at $t = 0$ and $N_l(t)$ is the number of original particles that persist in the largest cluster after a time interval t. (b) The relaxation time-scale of the largest cluster is shown at several densities of colloidal particles. The dotted curve is exponential fit.

5.7 Conclusions

In summary, we have studied the non-equilibrium percolation of colloidal assemblies in active liquids of chiral swimmers. The colloids form dynamic clusters due to effective interactions mediated by the active bath. The chirality of swimmers strongly influences the dynamics of individual particles and their aggregates, and it leads to persistent clockwise rotations of individual particles and their clusters. It also hinders the local orientational ordering of colloids, which is observed in equilibrium colloid-polymer mixtures. With the increasing density of colloids, the size of the clusters grows and eventually span the entire system at a critical density $\phi_c = 0.4$, which was determined from the spanning probability. Further analysis of various parameters, including cluster size distribution n_s^*, radius of gyration R_{gs}, average cluster size $\langle S \rangle$, and correlation length $\langle \xi \rangle$, along with their associated exponents τ, d_f, γ, and ν, suggests that colloid-bacteria mixtures displays several hallmark features of percolation transition. However, the exponents show marked deviations from the exponents of standard continuum percolation model. These are consistent with simulation results of percolation transition in purely active systems where the percolation exponents were reported to deviate from standard models [171, 173]. The exponent values found in our experiments need confirmation from finite system size analysis, which is possible with particle simulation methods [98, 171, 172]. Our experiments reveal rich features of colloidal assemblies in non-equilibrium baths, which should inspire further investigations to unveil novel rheological properties of colloidal assemblies in active liquids.

The other interesting aspect of our experiments is the dynamics of bacteria. Recent experiments [145] have shown interesting hydrodynamic effects on the motility of bacteria in the presence of colloidal particles. In addition, the way the presence of colloidal beads influence bacterial turbulence [153, 191] remains unknown. These aspects should motivate further investigations.

Chapter 6

Behavior of Individual Colloids and Cluster Formation in Active Liquids

Colloidal particles undergoing Brownian motion exhibit two key properties: their mean squared displacement (MSD) increases linearly over time, also known as Fickian diffusion, and their displacement distribution follows a Gaussian distribution. However, when colloids are suspended in an active medium, their MSD displays superdiffusive behavior at short time scales and normal diffusive behavior at longer time scales. At short times, the displacement distribution deviates from Gaussian, presenting a Gaussian core with an exponential tail, but it eventually turns to Gaussian distribution over longer time scales. Interestingly, when we examine larger colloids, where thermal fluctuations are negligible and only the activity of the surrounding medium influences their behavior, the displacement distribution does not display Gaussian even on longer times-scale. Furthermore, analysis of cluster statistics for these larger particles at steady state reveals the formation of dynamic clusters that continuously break and reform. The transition matrix of cluster aggregation and fragmentation highlights a clear trend toward the monomer approximation, which corresponds to a solvable kinetic equation under the condition of detailed balance.

6.1 Introduction

Brownian motion, thermally driven phenomenon, describes the movement of colloidal particles in a liquid due to constant bombardment by liquid molecules. Initially, on the timescale of molecular collisions (picoseconds), the particle exhibits ballistic motion. However, after numerous random collisions, the particle's direction changes, and over longer timescales (milliseconds), its mean squared displacement (MSD) becomes diffusive, scaling linearly with time. And the probability distribution function (PDF) of displacement follows Gaussian statistics. In certain nonequilibrium cases involving self-propelled particles like bacteria, amoebae, or Janus particles, these particles can sustain directed motion over experimentally observable timescales with finite-time correlations in their movement.

Below this correlation time, these particles exhibit ballistic behavior with non-Gaussian displacement PDFs. However, after times much longer than the correlation period, the direction of particle motion becomes randomized, resulting in the displacement PDF transitioning to a Gaussian distribution. In this regime, the particles display diffusive behavior, which is characterized by a linear MSD over time with an effective diffusion coefficient. Nevertheless, deviations from the linear MSD and Gaussian displacement profiles can occur even beyond the correlation time [192]. Instances of non-Gaussian displacement distributions, despite a linear MSD (known as Fickian behavior), have also been reported [193]. These deviations may arise from spatial and energetic disorder, viscoelastic effects, heterogeneous environments, or varying instantaneous particle diffusivity. To address these cases, supersatistical approaches [194] and diffusing diffusivity models [195] have been proposed. Superstatistics describes a system where diffusion is not homogeneous but governed by an ensemble of local environments, each characterized by different diffusivities that follow a distribution of diffusion constants. This distribution can vary across time or space, reflecting the heterogeneity of the system. Depending on the physical context, the distribution of diffusion constants can take different forms, such as Gaussian, Gamma, Laplace, or other relevant statistical distributions, capturing the fluctuating nature of the diffusive process in complex environments.

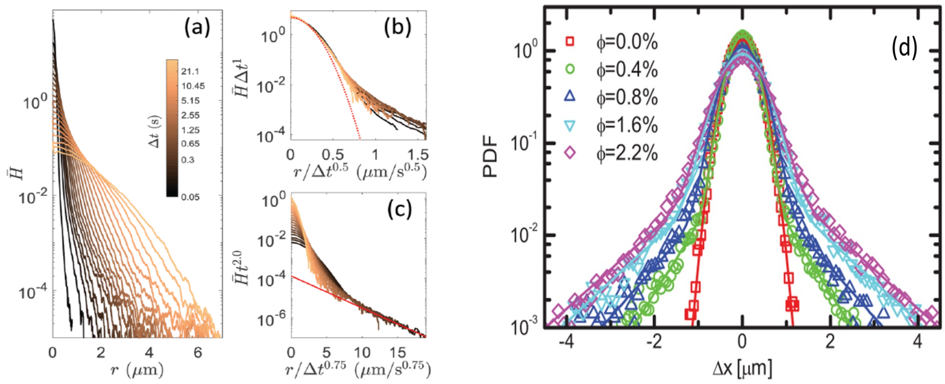

Figure 6.1: (a) Scaling of the radial probability distribution function $\bar{H}$ for a colloid in a bacterial bath at different lag times Δt. (b) $\bar{H}$ with r scaled by $\Delta t^{0.5}$. (c) $\bar{H}$ with r scaled by $\Delta t^{0.75}$. Image adapted from [42]. (d) Probability distribution functions for tracer displacements at a fixed time interval of $t = 0.12$ sec, for various swimmer volume fractions, illustrating the broadening of the Gaussian core and the emergence of exponential tails. Image adapted from [76].

We are interested in the non-Gaussian diffusion of passive particles in an active liquid containing bacteria, specifically after the transition from superdiffusive to diffusive dynamics, which is characterized by a linear MSD with an effective diffusion coefficient over long times. For short timescales, Antoine et al. [42] observed anomalous diffusion with a non-Gaussian displacement PDF and enhanced diffusion with Gaussian displacement PDF at long times for single colloids in a bacterial bath. To further elucidate the anomalous diffusion at short times, they analyzed the radial PDF of displacements, $H(x, y) = \bar{H}(r = \sqrt{x^2 + y^2})$, of colloids for various lag times Δt, as shown in Fig. 6.1(a). The function $\bar{H}$ displays a Gaussian core with exponential tails, which are more prominent at short times. At lower concentrations of bacteria, collisions are rare events, and the Gaussian centers can be attributed to thermal noise. Its standard deviation is given by $\sigma^2 \approx 4D_0\Delta t$, where D_0 is the thermal diffusion constant. Figure 6.1(b) shows the PDF with the horizontal axis rescaled by $\Delta t^{0.5}$ to illustrate the effect of thermal diffusion and the PDF fits a Gaussian distribution, as indicated by the red curve. At long times, after many collisions have occurred, the entire distribution becomes Gaussian as a consequence of the central limit theorem, with the distri-

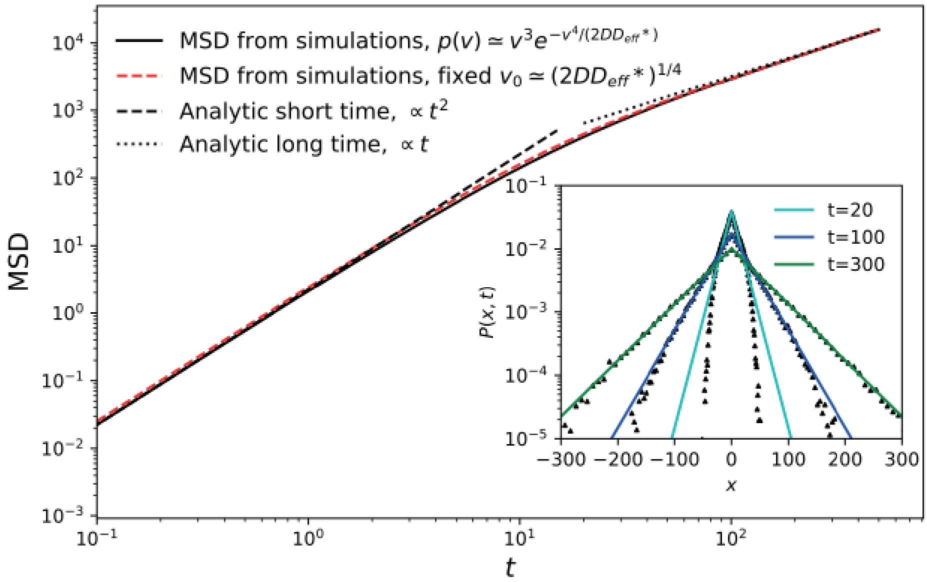

Figure 6.2: MSD and PDFs for the active particles with passive noise model. Inset: The blue, cyan, and green solid lines indicate Laplace PDFs. Image adapted from: [196].

bution width $\sigma^2 \approx 4D_{eff}\Delta t$. Fig. 6.1(c) presents the PDF with the horizontal axis rescaled by $\Delta t^{0.75}$ to highlight the effect of anomalous short-time diffusion, where $\langle \Delta r^2(t) \rangle \propto \Delta t^{1.5}$, and the PDF exhibits an exponential tail.

Another system where the time-dependent PDF of tracer displacements, suspended in the sea of alga, shows the clear systematic deviations from Gaussianity [76]. There are two changes in the distribution, first is the appearance of an exponential tail whose amplitude grows with swimmer concentration. And the second is the significant broadening of the Gaussian core. The PDF of tracer displacements fitted well to the weighted sum of Gaussian and exponential distribution as shown in the Fig. 6.1(d). As the concentration of swimmer increases the greater chance of encounter of the suspended particle with the swimmer lead to enhanced transport of the particles.

Elisabeth et al. [196] thoroughly investigated the effects of randomly distributed diffusivities and speeds for active particles with active and passive fluctuations and reported the emergence of non-Gaussian displacement PDF including exponential tails even in the long time limits. Figure 6.2 shows the MSD of active particles with passive fluctuations: the dashed red curve represents particles with fixed speed, while the solid black curve shows particles with a Weibull-distributed speed PDF. Both cases display identical MSD behaviors: ballistic motion at short times and linear scaling at long times. The inset shows the PDFs for different times gradually approach a Laplace-like shape as time progresses. These results clearly illustrate the effect of having non-uniform velocities.

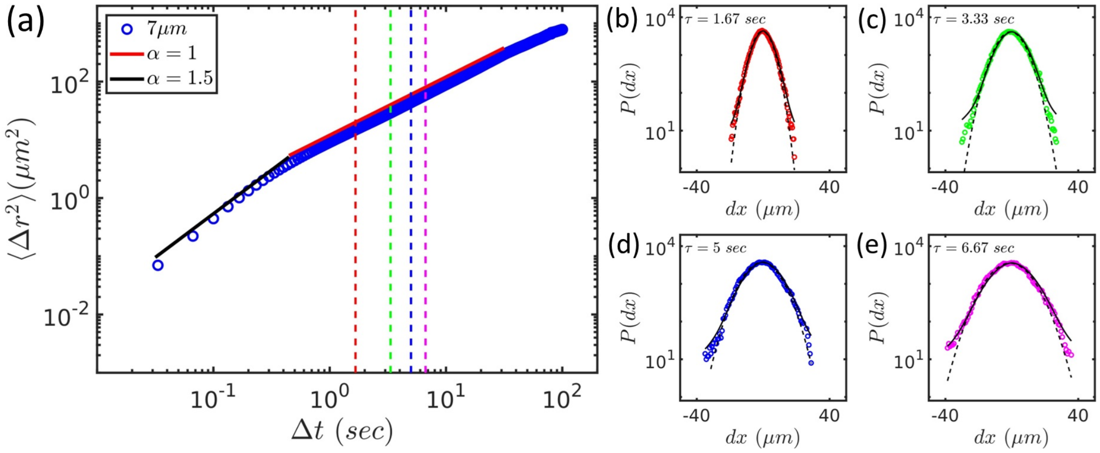

Figure 6.3: Mean square displacement (MSD) and Probability distribution function (PDF) of displacement for $7\mu m$ particles at bacteria density $c_b = 5b_0$, (a) black and red solid lines are showing the slope of 1.5 and 1 respectively to indicate the crossover from super-diffusive to normal diffusive regime, vertical dashed lines are showing the various lag-times for PDF: (b) for $\tau = 1.67\ sec$, (c) for $\tau = 3.33\ sec$, (d) for $\tau = 5\ sec$, (e) for $\tau = 6.67\ sec$, the dashed black curve is Gaussian fitting and black solid curve represents the Gaussian +exponential fitting.

6.2 Results on displacement PDF of isolated colloids suspended in active liquid

To investigate the PDF of displacement of a single particle suspended in the active liquid, we followed the same experimental procedure detailed in Section 2.3. We used colloids of two sizes, $7\mu m$ and $31\mu m$, with a fixed density of bacteria $c_b = 5b_0$. The area fraction of colloids was maintained at $\phi \sim 0.005$ to ensure they remained isolated, minimizing interactions between them. Figure 6.3(a)-(e) shows the MSD and PDF for $7\mu m$ particles at various lag-times, which are well beyond the crossover time from superdiffusive to linear in MSD,

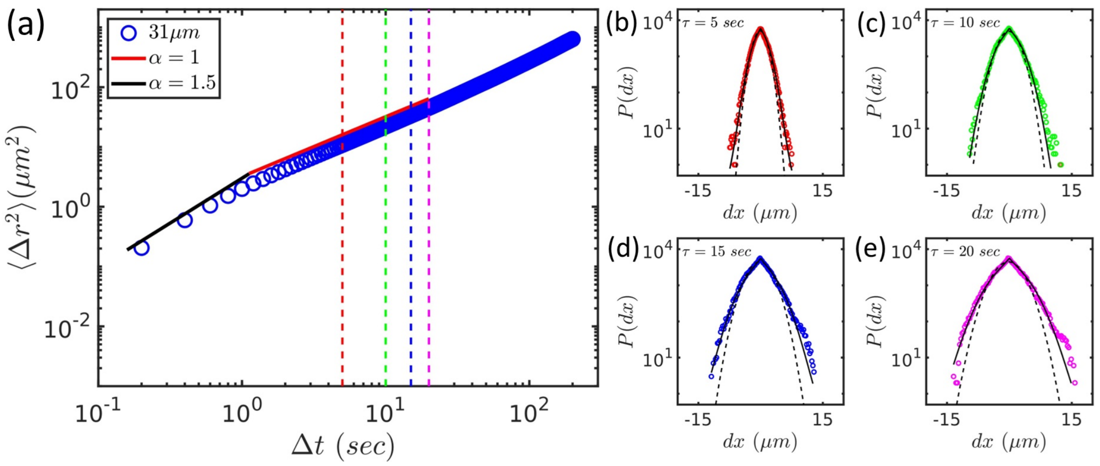

Figure 6.4: Mean square displacement (MSD) and Probability distribution function (PDF) of displacement for $31\mu m$ particles at bacteria density $c_b = 5b_0$, (a) black and red solid lines are showing the slope of 1.5 and 1 respectively to indicate the crossover from super-diffusive to normal diffusive regime, vertical dashed lines are showing the various lag-times for PDF: (b) for $\tau = 5\ sec$, (c) for $\tau = 10\ sec$, (d) for $\tau = 15\ sec$, (e) for $\tau = 20\ sec$, the dashed black curve is Gaussian fitting and black solid curve represents the Gaussian + exponential fitting.

indicated by dashed lines in the colors as corresponding PDF, shown in the Fig 6.3(a). Figure 6.4(a)-(e) presents the MSD and PDF for $31\mu m$ particles. The dashed black curve represent the Gaussian fitting, while the solid black curves show the Gaussian + exponential fitting as described in the Eq. 6.1.

$$P(dx) = \frac{a}{b}\exp\left(-\frac{dx^2}{2b^2}\right) + \frac{c}{d}\exp\left(-\frac{|dx|}{d}\right) \tag{6.1}$$

The $31\mu m$ particles are large enough to have negligible Brownian motion compared to the $7\mu m$ particles. As shown in Fig. 6.3(a), the smaller particles fit well with the Gaussian distribution, whereas the larger particles fit the Gaussian and exponential distribution, as shown in Fig. 6.4(a). The non-Gaussian exponential core observed in the larger particles as presented in Fig. 6.4(b)-(e) may be attributed to their widely varying diffusivities over different time intervals along their trajectory. These aspects requires further investigations that are in progress. This work is ongoing, and these findings are the initial results.

6.3 Aggregation and fragmentation kinetic model

The ability of active matter to self-organize and exhibit various emergent behaviors is a well-established phenomenon. However, understanding how passive and thermal systems organize in the presence of active particles remains an fascinating area of study. In all living matter, there is a mix of active and passive components. While the self-organization of passive components in passive environments is well understood and follows equilibrium statistics, their behavior in active environments is less explored. In this study, we present an experimental analysis of the cluster dynamics of non-Brownian passive colloids in an active liquid, revealing their continuous formation and disintegration by kinetic theory. F. Ginot et al. [197] investigated the cluster phase of Janus active particles by analyzing the size-dependent fragmentation and aggregation rates. Their study rationalized the cluster size distribution and lifetimes using a simple kinetic approach with a monomer approximation. They employed an additional time constraint along with the distance criterion to define clusters. Figure 6.5(a) shows the cluster size distribution, which aligns well with the kinetic model, accounting for errors in the aggregation and fragmentation rates. Figure 6.5(b) represents the probability of a cluster of size N_0 transitioning to size N_1 over a time interval ΔT. This result supports the monomer approximation, meaning that only single colloids take part in the aggregation and fragmentation events, as most transitions occur along the diagonal. The

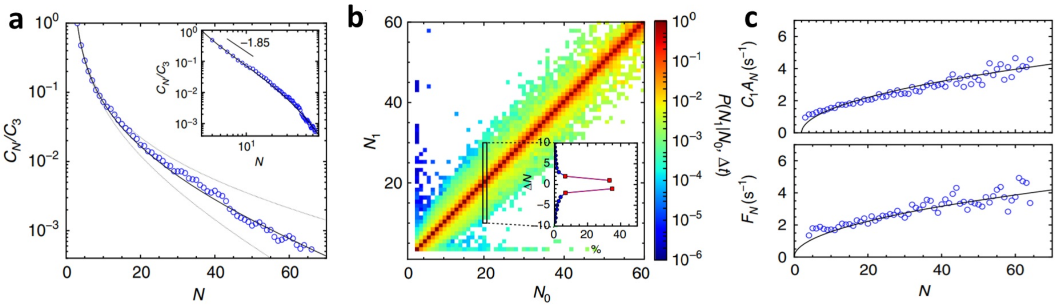

Figure 6.5: (a) Cluster size distribution C_N/C_3 vs N, decaying as power law with slope -1.85, (b) Transition matrix showing the probability of cluster size $P(N_0|N_1, \Delta t)$ transitioning from N_0 to N_1 in time Δt, (c) Aggregation rate and fragmentation rate as a function of cluster size N, Image taken from: [197].

aggregation and fragmentation rates shown in Figure 6.5(c) reflect the perimeter approximation, indicating that particles associate and dissociate primarily around the perimeter of clusters.

The aggregation-fragmentation kinetic model is a fundamental concept in the study of systems where various particles or clusters combine to form larger aggregates and break apart into smaller fragments. The elementary binary event can be represented as:

$$[\mathrm{i}] + [\mathrm{j}] \underset{\mathrm{F_{ij}}C_{i+j}}{\overset{\mathrm{A_{ij}}\,C_iC_j}{\rightleftharpoons}} [\mathrm{i}+\mathrm{j}] \tag{6.2}$$

where, a cluster of size i and size j merges to form a cluster of size $i+j$ with aggregation rate $A_{ij}C_iC_j$. And the reverse process occurs with the fragmentation rate $F_{ij}C_{i+j}$. The general form of the time evolution of the cluster size distribution, $\dot{C}_n(t)$, is governed by the master equation:

$$\dot{C}_n(t) = \frac{1}{2}\sum_{i+j=n} A_{ij}C_iC_j - C_n\sum_{j\geq 1} A_{nj}C_j + \sum_{j\geq 1} F_{nj}C_{j+n} - \frac{1}{2}C_n\sum_{i+j=n} F_{i+j} \tag{6.3}$$

The kernels are time-independent, meaning the rates depend only on cluster concentrations and time-independent geometrical factors. This is a mean field theory, implying no spatial correlations between clusters. Therefore, the system must be sufficiently dilute for clusters to aggregate by diffusion.

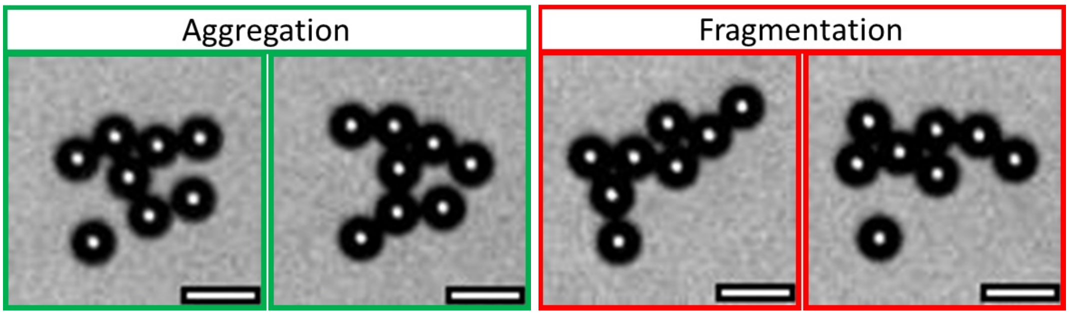

Figure 6.6: The bright field image showing the aggregation event: left, fragmentation event: right.

The model consists of an infinite set of coupled non-linear first-order differential equations, making it impossible to solve analytically in general. However, solutions exist for specific systems under certain assumptions. To solve the rate equations, various analytical and numerical methods are employed. Analytical solutions are typically available only for simplified cases. Numerical methods, such as Monte Carlo simulations or discretized versions of the rate equations, are often used to study more complex systems. The above equation get simplified with the monomer assumption. The binary event with monomer approximation can be represented as:

$$[\mathrm{n}] + [1] \xrightleftharpoons[\mathrm{F}_{n+1}\mathrm{C}_{n+1}]{\mathrm{A}_n\,\mathrm{C}_1\mathrm{C}_n} [\mathrm{n}+1] \tag{6.4}$$

The kinetic equation becomes:

$$\dot{C}_n(t) = A_{n-1}C_1C_{n-1} - A_nC_1C_n + F_{n+1}C_{n+1} - F_nC_n \tag{6.5}$$

By imposing the condition of detailed balance, with forward and backward rates in the Eq. 6.5, $F_{n+1}C_{n+1} = A_nC_1C_n$, are equivalent. We can get the steady state solution

$$C_n = \left[\prod_{m=1}^{n} \frac{A_{m-1}}{F_m} C_1^n\right] \tag{6.6}$$

with C_1 if fixed by normalization. Eq. 6.6 applies whenever A_n and F_n depends on the cluster size. For the particular case mentioned in [198, 199] where the exchange rates have a power law dependency with size: $A_n \sim n^{\alpha}$ and $F_n \sim n^{\alpha'}$, the cluster size distribution simplifies:

$$C_n \sim \frac{[(n-1)!]^{\alpha-\alpha'}}{n^{\alpha'}} C1^n \tag{6.7}$$

In particular case, with $\alpha = \alpha'$ it further simplifies,

$$C_n \sim \frac{e^{-n/n_c}}{n^{\alpha}} \tag{6.8}$$

with $n_c = -1/\ln(c_1)$. The assumption $\alpha = \alpha'$ recovers the well appreciated cluster size distribution behaviour with power law and exponential cutoff at large n.

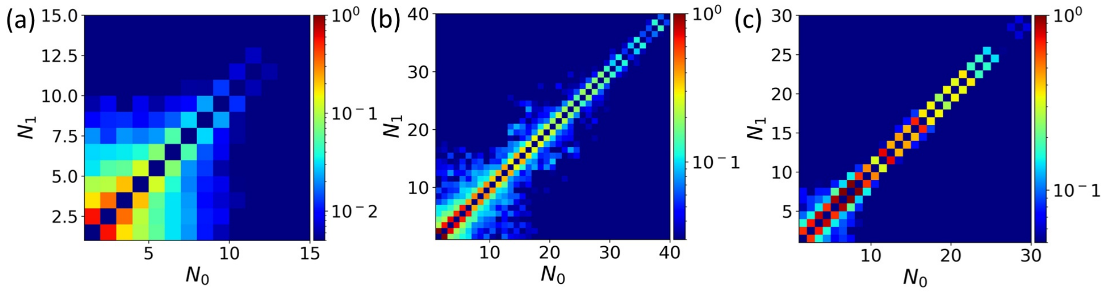

Figure 6.7: Transition matrix for the aggregation and fragmentation events (a) For particle size $10\mu m$ (b) For particle size $15\mu m$ (c) For particle size $31\mu m$ at the bacterial density $c_b = 10b_0$ with area fraction $\phi \sim 0.15$. The color bar is showing the logarithmic value of probability $P(N_0|N_1, \tau)$.

6.4 Results on cluster aggregation and fragmentation

In our system of bacteria and colloid mixture, colloids form dynamic clusters that continuously break and reform. We identified the clusters using a cutoff of 1.2σ. The bright field image of aggregation event and fragmentation event is shown in Fig. 6.6.

We calculated the transition matrix for cluster aggregation and fragmentation over a lag time of $\tau = 0.2$ sec, where N_0 represents the cluster size at time t_0 and N_1 represents the cluster size at time $t_0 + \tau$. The values in the transition matrix indicate the probability of a cluster transitioning from size N_0 to N_1, denoted as $P(N_0|N_1, \tau)$, is shown in the Fig. 6.7. We have shown the transition matrix for various particle sizes 10 μm, 15 μm and 31 μm at bacterial density $c_b = 10b_0$ with area fraction of colloids $\phi \sim 0.15$. The figure clearly shows that as the relative size of the colloids increases, the probability of single-particle aggregation and fragmentation events, which lie near the diagonal of the matrix, also increases. This observation strongly supports the monomer approximation, for which the master equation is exactly solvable. Although the transition matrix clearly indicates the presence of monomer approximation, it's important to note that our clusters are not solid structures; they are continuously restructuring and changing shape while rotating. The aggregation process does not occur with single particles merging directly into large clusters. Instead, due to the rotation of the clusters, particles are aggregating and detaching from the periphery, contributing to

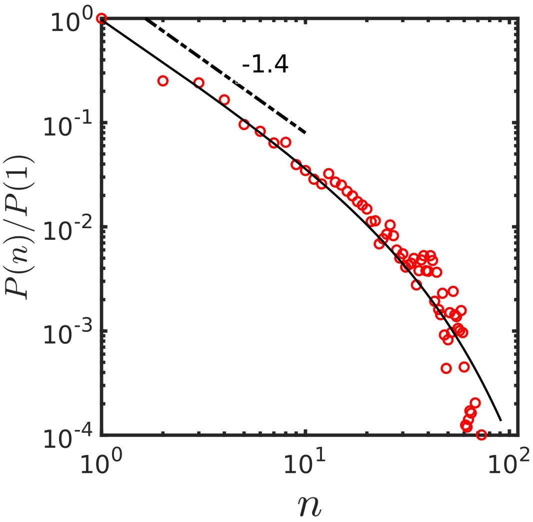

Figure 6.8: The cluster size distribution $P(n)/P(1)$ vs n the black curve is fitted with Eq. 6.8 with slope $\alpha \sim 1.4$.

the dynamic nature of the system. Given that these results are preliminary, we have not yet calculated the aggregation and fragmentation rates. This work is still ongoing. However, we have determined the cluster size distribution and fitted it to Eq. 6.8. In Fig. 6.8, the cluster size distribution for particles with a size of 31 μm is shown. The black curve represents the fit to Eq. 6.8, with a slope of $\alpha = 1.4$.

6.5 Conclusion

In summary, we investigated the dynamics of single particles suspended in an active bath, focusing on the mean squared displacement (MSD) and displacement distribution of colloids. Our findings reveal that the diffusive behavior of colloids is strongly influenced by their size. For relatively smaller particles, the displacement distribution indicates Fickian diffusion, with Gaussian displacement statistics observed over longer time scales. Whereas, for larger particles where thermal effects are negligible, the dynamics are predominantly driven by the activity of the surrounding liquid. These particles still exhibit Fickian diffusion over the long duration, but their displacement distribution becomes non-Gaussian, characterized by a Laplacian core, especially at lower bacterial densities and with larger colloids. This phenomenon can be interpreted through the concept of superstatistics. Additionally, we analyzed the cluster dynamics of colloids in the steady state within the active bath using an aggregation and fragmentation kinetic model. The transition matrix provides clear evidence of monomer approximation in our system, allowing the kinetic equations to be exactly solvable under the detailed balance condition.

Chapter 7

Summary and Future Outlook

7.1 Summary and conclusions

In this thesis, we have presented a detailed exploration of the complex behavior of passive colloids in active media, uncovering several novel insights into their effective interactions, phase behavior including dynamics clustering, percolation transition, coarsening aspects, and single particle dynamics.

We first present the investigation of the phase behavior of colloidal particles by focusing on the effective interactions between colloids in active liquids. This was accomplished by a combination of experiments and simulations. A key finding was that the size ratio between passive and active particles acts as a tunable parameter for modulating the strength and range of this effective potential. When the size ratio is large, the effective potential becomes strong enough to induce macroscopic phase separation among passive particles. Simulations revealed that density fluctuations of active particles play a crucial role in enhancing the effective potential as the size ratio increases, leading to more stable clusters of larger colloidal particles. These findings provide a fresh perspective on the nonequilibrium assembly of passive particles.

One of the interesting aspect of phase separation is the ordering kinetics. This aspect of the problem is well understood in the context of equilibrium phase separation. This thesis explores the novel features of coarsening dynamics of colloidal clusters in active liquids. Our studies revealed that the mixtures of colloids and swimmers are inherently unstable, leading to spontaneous phase separation through dynamic clustering. While our experiments captured the early stages of coarsening, late-stage dynamics remain beyond the current experimental timescales. The correlation functions of the scalar order parameter displayed dynamic scaling, with the characteristic length scale growing as $L(t) \sim t^{1/4}$, which is slower than the predictions of Lifshitz-Slyozov theory. The correlation function at short distances is characterized by a cusp singularity indicative of rough interfaces between colloid-rich and colloid-poor phases, and fractal nature of the colloidal clusters. These findings suggest that activity reduces interfacial tension, leading to diffuse and rough interfaces characteristic of fluctuation-dominated phase ordering.

We next explored the nonequilibrium percolation transition of colloidal assemblies in active liquids of chiral swimmers. The colloids formed dynamic clusters due to effective interactions mediated by the active bath. The chirality of the swimmers was found to significantly influence the dynamics, causing persistent rotations and hindering local orientational ordering among the colloids. As the density of colloids increased, the clusters grew in size, eventually spanning the entire system at a critical density. Our analysis suggested that the colloid-bacteria mixtures exhibit several hallmark features of a percolation transition, although with exponents deviating from those predicted by standard continuum percolation models. These deviations align with recent simulations in purely active systems, underscoring the unique nature of percolation transitions in nonequilibrium environments.

Finally, we characterise the dynamics of single colloids suspended in a chiral active bath, focusing on their mean squared displacement (MSD) and displacement distribution. Our results showed that the diffusive behavior of colloids is significantly dependent on their size. For smaller particles, the displacement distribution indicated Fickian diffusion with Gaussian statistics over long timescales. However, for larger particles, where thermal effects are negligible, the dynamics were dominated by the activity of the surrounding liquid, leading to a non-Gaussian displacement distribution with a Laplacian core. This phenomenon, more pronounced at lower bacterial densities and with larger colloids, can be interpreted through the concept of superstatistics. Additionally, we analyzed the cluster dynamics within the active bath using an aggregation and fragmentation kinetic model, which confirmed the monomer approximation in our system, allowing for the exact solvability of the kinetic equations under detailed balance conditions.

In conclusion, our comprehensive study has shed new light on the dynamics nonequilibrium assembly of colloids in active media, providing a foundation for future research into building dissipative colloidal superstructures. By exploring various aspects such as phase behavior, percolation transitions, coarsening dynamics, and single-particle diffusion, this work opens new avenues for understanding the emergent properties of passive-active mixtures and their potential applications in soft matter physics.

7.2 Future outlook

The behavior of passive colloids in thermal baths is well understood, and recent studies has extensively explored the emergent phenomena of active particles, both living and synthetic, through experimental and numerical studies. However, the interactions of particles suspended in a non-equilibrium active environment remain relatively less explored, both experimentally and in simulations. This is largely due to the increased complexity arising from multi-particle interactions, such as those between colloids and bacteria, as well as hydrodynamic interactions with the surrounding fluid. There is significant potential in this system to address key questions about how an active environment influences a collection of passive entities, which depends not only on the size of the passive particles but also on their shape.

In this thesis, we emphasized our whole attention on spherical colloids. A natural extension of this work would involve investigating how an active environment impacts asymmetric particles, such as ellipsoids. With their additional degrees of freedom as orientation along with the position, the phase behavior of ellipsoidal particles in an active liquid could differ significantly. Key questions include how the aspect ratio of the ellipsoids influences the phase diagram, whether particle shape affects fluctuation-dominated phase ordering, and what role the chirality of the active liquid plays in phase ordering. Additionally, the single particle characterization would also open the unexplored area to explore such as Fickian diffusion with non-Gaussian distribution of displacement in transnational as well as rotational degree of freedom.

Our study examined the low- and intermediate-density limits of colloids in an active environment. Future work could explore the behavior of colloids at higher densities. Important questions in this regime include whether the system exhibits active jamming, active glass transitions, or dynamic heterogeneity. Given that colloids in a chiral liquid themselves become chiral, it would also be worth investigating whether this chirality alters phase behavior in the dense limit.

As we observed, increasing the size of colloids enhances the effective interaction potential, with the interaction range becoming comparable to the size of the passive particles. For larger colloids, the effective attractive interaction is quite strong. This raises the question whether the system could exhibit gelation with mechanical stability or if it would form only a physical gel. Another intriguing question is whether the percolation transition aligns with the mechanical stability.

The bacteria density in all our investigation were well below the threshold for the onset of collective behavior. However, there is much to explore in the turbulent regime of bacterial motion.

Bibliography

[1] R. Brown, "A brief account of microscopical observations made in the months of june, july and august, 1827, on the particles contained in the pollen of plants; and on the general existence of active molecules in organic and inorganic bodies", *Philosophical Magazine* **4**(21), 161 (1828).

[2] A. Einstein. *Investigations on the Theory of the Brownian Movement* (Courier Corporation, 1956).

[3] R. Newburgh, J. Peidle, and W. Rueckner, "Einstein, perrin, and the reality of atoms: 1905 revisited", *American journal of physics* **74**(6), 478 (2006).

[4] P. N. Pusey and W. Van Megen, "Phase behaviour of concentrated suspensions of nearly hard colloidal spheres", *Nature* **320**(6060), 340 (1986).

[5] W. Van Megen and S. M. Underwood, "Glass transition in colloidal hard spheres: Measurement and mode-coupling-theory analysis of the coherent intermediate scattering function", *Phys. Rev. E* **49**, 4206 (1994).

[6] E. R. Weeks, J. C. Crocker, A. C. Levitt, A. Schofield, and D. A. Weitz, "Three-dimensional direct imaging of structural relaxation near the colloidal glass transition", *Science* **287**, 627 (2000).

[7] G. L. Hunter and E. R. Weeks, “The physics of the colloidal glass transition”, *Rep. Prog. Phys.* **75**, 066501 (2012).

[8] E. Zaccarelli, “Colloidal gels: Equilibrium and non-equilibrium routes”, *Journal of Physics: Condensed Matter* **19**(32), 323101 (2007).

[9] P. J. Lu, E. Zaccarelli, F. Ciulla, A. B. Schofield, F. Sciortino, and D. A. Weitz, “Gelation of particles with short-range attraction”, *Nature* **453**, 499 (2008).

[10] U. Gasser, E. R. Weeks, A. Schofield, P. Pusey, and D. Weitz, “Real-space imaging of nucleation and growth in colloidal crystallization”, *Science* **292**(5515), 258 (2001).

[11] D. G. A. L. Aarts, M. Schmidt, and H. N. W. Lekkerkerker, “Direct visual observation of thermal capillary waves”, *Science* **304**(5672), 847 (2004).

[12] C. P. Royall, S. R. Williams, T. Ohtsuka, and H. Tanaka, “Direct observation of a local structural mechanism for dynamic arrest”, *Nature Materials* **7**(7), 556 (2008).

[13] A. Yethiraj and A. van Blaaderen, “A colloidal model system with an interaction tunable from hard sphere to soft and dipolar”, *nature* **421**(6922), 513 (2003).

[14] R. Tuinier and H. N. Lekkerkerker. *Colloids and the depletion interaction* (Springer Netherlands, 2011).

[15] D. J. Kraft, R. Ni, F. Smallenburg, M. Hermes, K. Yoon, D. A. Weitz, A. van Blaaderen, J. Groenewold, M. Dijkstra, and W. K. Kegel, “Surface roughness directed self-assembly of patchy particles into colloidal micelles”, *Proceedings of the National Academy of Sciences* **109**(27), 10787 (2012).

[16] T. Hueckel, G. M. Hocky, and S. Sacanna, “Total synthesis of colloidal matter”, *Nature Reviews Materials* **6**(11), 1053 (2021).

[17] S. Carroll. In a flight of starlings by giorgio parisi â book review. The TLS (2023). Accessed: 2024-07-08, URL `https:`

//www.the-tls.co.uk/science-technology/sciences/in-a-flight-of-starlings-giorgio-parisi-book-review-sean-carroll/

[18] A. Mostaani. Wisdom of fishes: Can they be a source of inspiration for humans? LinkedIn (2023). Accessed: 2024-07-08, URL https://www.linkedin.com/pulse/wisdom-fishes-can-source-inspiration-humans-arsham-mostaani/.

[19] M. C. Marchetti, J.-F. Joanny, S. Ramaswamy, T. B. Liverpool, J. Prost, M. Rao, and R. A. Simha, "Hydrodynamics of soft active matter", *Reviews of modern physics* **85**(3), 1143 (2013).

[20] V. Narayan, S. Ramaswamy, and N. Menon, "Long-lived giant number fluctuations in a swarming granular nematic", *Science* **317**(5834), 105 (2007).

[21] M. N. Van Der Linden, L. C. Alexander, D. G. Aarts, and O. Dauchot, "Interrupted motility induced phase separation in aligning active colloids", *Physical review letters* **123**(9), 098001 (2019).

[22] L. Giomi, "Geometry and topology of turbulence in active nematics", *Physical Review X* **5**(3), 031003 (2015).

[23] C. Bechinger, R. Di Leonardo, H. Löwen, C. Reichhardt, G. Volpe, and G. Volpe, "Active particles in complex and crowded environments", *Reviews of Modern Physics* **88**(4), 045006 (2016).

[24] D. A. Fletcher and P. L. Geissler, "Active biological materials", *Annual review of physical chemistry* **60**, 469 (2009).

[25] D. Needleman and Z. Dogic, "Active matter at the interface between materials science and cell biology", *Nature reviews materials* **2**(9), 1 (2017).

[26] S. Ramaswamy, "Active matter", *Journal of Statistical Mechanics: Theory and Experiment* **2017**(5), 054002 (2017).

[27] P. Romanczuk, M. Bär, W. Ebeling, B. Lindner, and L. Schimansky-Geier, “Active brownian particles: From individual to collective stochastic dynamics”, *The European Physical Journal Special Topics* **202**, 1 (2012).

[28] C. Dombrowski, L. Cisneros, S. Chatkaew, R. E. Goldstein, and J. O. Kessler, “Self-concentration and large-scale coherence in bacterial dynamics”, *Physical review letters* **93**(9), 098103 (2004).

[29] H. Wioland, F. G. Woodhouse, J. Dunkel, J. O. Kessler, and R. E. Goldstein, “Confinement stabilizes a bacterial suspension into a spiral vortex”, *Physical review letters* **110**(26), 268102 (2013).

[30] H. M. López, J. Gachelin, C. Douarche, H. Auradou, and E. Clément, “Turning bacteria suspensions into superfluids”, *Physical review letters* **115**(2), 028301 (2015).

[31] E. M. Purcell, “Life at low reynolds number”, *American journal of physics* **45**(1), 3 (1977).

[32] E. Lauga, “Bacterial hydrodynamics”, *Annual Review of Fluid Mechanics* **48**, 105 (2016).

[33] M. Demir and H. Salman, “Bacterial thermotaxis by speed modulation”, *Biophysical journal* **103**(8), 1683 (2012).

[34] G. Miño, J. Dunstan, A. Rousselet, E. Clément, and R. Soto, “Induced diffusion of tracers in a bacterial suspension: theory and experiments”, *Journal of Fluid Mechanics* **729**, 423 (2013).

[35] H. C. Berg, “Motile behavior of bacteria”, *Physics today* **53**(1), 24 (2000).

[36] V. Sourjik and N. S. Wingreen, “Responding to chemical gradients: bacterial chemotaxis”, *Current opinion in cell biology* **24**(2), 262 (2012).

[37] A. P. Berke, L. Turner, H. C. Berg, and E. Lauga, “Hydrodynamic attraction of swimming microorganisms by surfaces”, *Physical Review Letters* **101**(3), 038102 (2008).

[38] E. Lauga, W. R. DiLuzio, G. M. Whitesides, and H. A. Stone, “Swimming in circles: motion of bacteria near solid boundaries”, *Biophysical journal* **90**(2), 400 (2006).

[39] A. Zöttl, “Hydrodynamics of microswimmers in confinement and in poiseuille flow” (2014).

[40] K. Drescher, J. Dunkel, L. H. Cisneros, S. Ganguly, and R. E. Goldstein, “Fluid dynamics and noise in bacterial cell–cell and cell–surface scattering”, *Proceedings of the National Academy of Sciences* **108**(27), 10940 (2011).

[41] X.-L. Wu and A. Libchaber, “Particle diffusion in a quasi-two-dimensional bacterial bath”, *Physical review letters* **84**(13), 3017 (2000).

[42] A. Lagarde, N. Dagès, T. Nemoto, V. Démery, D. Bartolo, and T. Gibaud, “Colloidal transport in bacteria suspensions: from bacteria collision to anomalous and enhanced diffusion”, *Soft Matter* **16**(32), 7503 (2020).

[43] A. E. Patteson, A. Gopinath, P. K. Purohit, and P. E. Arratia, “Particle diffusion in active fluids is non-monotonic in size”, *Soft matter* **12**(8), 2365 (2016).

[44] I. Theurkauff, C. Cottin-Bizonne, J. Palacci, C. Ybert, and L. Bocquet, “Dynamic clustering in active colloidal suspensions with chemical signaling”, *Physical review letters* **108**(26), 268303 (2012).

[45] J. Palacci, S. Sacanna, A. P. Steinberg, D. J. Pine, and P. M. Chaikin, “Living crystals of light-activated colloidal surfers”, *Science* **339**(6122), 936 (2013).

[46] M. E. Cates and J. Tailleur, “Motility-induced phase separation”, *Annu. Rev. Condens. Matter Phys.* **6**(1), 219 (2015).

[47] Y. Fily and M. C. Marchetti, “Athermal phase separation of self-propelled particles with no alignment”, *Physical review letters* **108**(23), 235702 (2012).

[48] G. S. Redner, M. F. Hagan, and A. Baskaran, “Structure and dynamics of a phase-separating active colloidal fluid”, *Physical Review Letters* **110**(5), 055701 (2013).

[49] J. Stenhammar, A. Tiribocchi, R. J. Allen, D. Marenduzzo, and M. E. Cates, “Continuum theory of phase separation kinetics for active brownian particles”, *Physical Review Letters* **111**(14), 145702 (2013).

[50] M. E. Cates and J. Tailleur, “When are active brownian particles and run-and-tumble particles equivalent? consequences for motility-induced phase separation”, *EPL (Europhysics Letters)* **101**(2), 20010 (2013).

[51] L. Alexander. *Motility induced phase separation: numerical and experimental approaches towards the high Péclet regime*. Ph.D. thesis, University of Oxford (2022).

[52] J. Adler and B. Templeton, “The effect of environmental conditions on the motility of escherichia coli”, *Microbiology* **46**(2), 175 (1967).

[53] H. M. López, J. Gachelin, C. Douarche, H. Auradou, and E. Clément, “Turning bacteria suspensions into superfluids”, *Physical review letters* **115**(2), 028301 (2015).

[54] J. Adler, “Effect of amino acids and oxygen on chemotaxis in escherichia coli”, *Journal of bacteriology* **92**(1), 121 (1966).

[55] S. Dar, S. C. Kamerkar, and T. J. Pucadyil, “Use of the supported membrane tube assay system for real-time analysis of membrane fission reactions”, *nature protocols* **12**(2), 390 (2017).

[56] J. C. Crocker and D. G. Grier, “Methods of digital video microscopy for colloidal studies”, *Journal of colloid and interface science* **179**(1), 298 (1996).

[57] K. J. Cutler, C. Stringer, T. W. Lo, L. Rappez, N. Stroustrup, S. Brook Peterson, P. A. Wiggins, and J. D. Mougous, "Omnipose: a high-precision morphology-independent solution for bacterial cell segmentation", *Nature methods* **19**(11), 1438 (2022).

[58] Y. T. Fukai and K. Kawaguchi, "Laptrack: linear assignment particle tracking with tunable metrics", *Bioinformatics* **39**(1), btac799 (2023).

[59] E. Stamhuis and W. Thielicke, "Pivlab–towards user-friendly, affordable and accurate digital particle image velocimetry in matlab", *Journal of open research software* **2**(1), 30 (2014).

[60] D. Nishiguchi, I. S. Aranson, A. Snezhko, and A. Sokolov, "Engineering bacterial vortex lattice via direct laser lithography", *Nature communications* **9**(1), 4486 (2018).

[61] H. Reinken, D. Nishiguchi, S. Heidenreich, A. Sokolov, M. Bär, S. H. Klapp, and I. S. Aranson, "Organizing bacterial vortex lattices by periodic obstacle arrays", *Communications Physics* **3**(1), 76 (2020).

[62] E. M. Furst and T. M. Squires. *Microrheology* (Oxford University Press, 2017).

[63] P. Kushwaha, V. Semwal, S. Maity, S. Mishra, and V. Chikkadi, "Phase separation of passive particles in active liquids", *Physical Review E* **108**(3), 034603 (2023).

[64] S. Sacanna, M. Korpics, K. Rodriguez, L. Colón-Meléndez, S.-H. Kim, D. J. Pine, and G.-R. Yi, "Shaping colloids for self-assembly", *Nature communications* **4**(1), 1688 (2013).

[65] S. C. Glotzer and M. J. Solomon, "Anisotropy of building blocks and their assembly into complex structures", *Nature materials* **6**(8), 557 (2007).

[66] W. Götze, J. Hansen, D. Levesque, and J. Zinn-Justin. Liquids, freezing and the glass transition (1991).

[67] E. M. Terentjev and D. A. Weitz. *The Oxford handbook of soft condensed matter* (Oxford Handbooks, 2015).

[68] S. Gokhale, J. Li, A. Solon, J. Gore, and N. Fakhri, "Dynamic clustering of passive colloids in dense suspensions of motile bacteria", *Physical Review E* **105**(5), 054605 (2022).

[69] F. Kümmel, P. Shabestari, C. Lozano, G. Volpe, and C. Bechinger, "Formation, compression and surface melting of colloidal clusters by active particles", *Soft matter* **11**(31), 6187 (2015).

[70] T. Vicsek, A. Czirók, E. Ben-Jacob, I. Cohen, and O. Shochet, "Novel type of phase transition in a system of self-driven particles", *Physical review letters* **75**(6), 1226 (1995).

[71] A. Bricard, J.-B. Caussin, N. Desreumaux, O. Dauchot, and D. Bartolo, "Emergence of macroscopic directed motion in populations of motile colloids", *Nature* **503**(7474), 95 (2013).

[72] M. E. Cates and J. Tailleur, "Motility-induced phase separation", *Annu. Rev. Condens. Matter Phys.* **6**(1), 219 (2015).

[73] I. Buttinoni, J. Bialké, F. Kümmel, H. Löwen, C. Bechinger, and T. Speck, "Dynamical clustering and phase separation in suspensions of self-propelled colloidal particles", *Physical review letters* **110**(23), 238301 (2013).

[74] J. Palacci, S. Sacanna, A. P. Steinberg, D. J. Pine, and P. M. Chaikin, "Living crystals of light-activated colloidal surfers", *Science* **339**(6122), 936 (2013).

[75] H. H. Wensink, J. Dunkel, S. Heidenreich, K. Drescher, R. E. Goldstein, H. Löwen, and J. M. Yeomans, "Meso-scale turbulence in living fluids", *Proceedings of the national academy of sciences* **109**(36), 14308 (2012).

[76] K. C. Leptos, J. S. Guasto, J. P. Gollub, A. I. Pesci, and R. E. Goldstein, “Dynamics of enhanced tracer diffusion in suspensions of swimming eukaryotic microorganisms”, *Physical Review Letters* **103**(19), 198103 (2009).

[77] C. Valeriani, M. Li, J. Novosel, J. Arlt, and D. Marenduzzo, “Colloids in a bacterial bath: simulations and experiments”, *Soft Matter* **7**(11), 5228 (2011).

[78] J.-L. Thiffeault, “Distribution of particle displacements due to swimming microorganisms”, *Physical Review E* **92**(2), 023023 (2015).

[79] R. Jeanneret, D. O. Pushkin, V. Kantsler, and M. Polin, “Entrainment dominates the interaction of microalgae with micron-sized objects”, *Nature communications* **7**(1), 12518 (2016).

[80] A. J. Mathijssen, R. Jeanneret, and M. Polin, “Universal entrainment mechanism controls contact times with motile cells”, *Physical Review Fluids* **3**(3), 033103 (2018).

[81] H. Shum and J. M. Yeomans, “Entrainment and scattering in microswimmer-colloid interactions”, *Physical Review Fluids* **2**(11), 113101 (2017).

[82] L. Ortlieb, S. Rafaï, P. Peyla, C. Wagner, and T. John, “Statistics of colloidal suspensions stirred by microswimmers”, *Physical review letters* **122**(14), 148101 (2019).

[83] L. Angelani, C. Maggi, M. Bernardini, A. Rizzo, and R. Di Leonardo, “Effective interactions between colloidal particles suspended in a bath of swimming cells”, *Physical review letters* **107**(13), 138302 (2011).

[84] D. Ray, C. Reichhardt, and C. O. Reichhardt, “Casimir effect in active matter systems”, *Physical Review E* **90**(1), 013019 (2014).

[85] R. Ni, M. A. C. Stuart, and P. G. Bolhuis, “Tunable long range forces mediated by self-propelled colloidal hard spheres”, *Physical review letters* **114**(1), 018302 (2015).

[86] M. Zaeifi Yamchi and A. Naji, “Effective interactions between inclusions in an active bath”, *The Journal of chemical physics* **147**(19) (2017).

[87] F. Feng, T. Lei, and N. Zhao, “Tunable depletion force in active and crowded environments”, *Physical Review E* **103**(2), 022604 (2021).

[88] F. Smallenburg and H. Löwen, “Swim pressure on walls with curves and corners”, *Physical Review E* **92**(3), 032304 (2015).

[89] J. Harder, S. Mallory, C. Tung, C. Valeriani, and A. Cacciuto, “The role of particle shape in active depletion”, *The Journal of chemical physics* **141**(19) (2014).

[90] P. Liu, S. Ye, F. Ye, K. Chen, and M. Yang, “Constraint dependence of active depletion forces on passive particles”, *Physical review letters* **124**(15), 158001 (2020).

[91] Y. Baek, A. P. Solon, X. Xu, N. Nikola, and Y. Kafri, “Generic long-range interactions between passive bodies in an active fluid”, *Physical review letters* **120**(5), 058002 (2018).

[92] A. K. Omar, Y. Wu, Z.-G. Wang, and J. F. Brady, “Swimming to stability: structural and dynamical control via active doping”, *ACS nano* **13**(1), 560 (2018).

[93] S. R. McCandlish, A. Baskaran, and M. F. Hagan, “Spontaneous segregation of self-propelled particles with different motilities”, *Soft Matter* **8**(8), 2527 (2012).

[94] S. C. Takatori and J. F. Brady, “A theory for the phase behavior of mixtures of active particles”, *Soft Matter* **11**(40), 7920 (2015).

[95] J. Stenhammar, R. Wittkowski, D. Marenduzzo, and M. E. Cates, “Activity-induced phase separation and self-assembly in mixtures of active and passive particles”, *Physical review letters* **114**(1), 018301 (2015).

[96] S. N. Weber, C. A. Weber, and E. Frey, “Binary mixtures of particles with different diffusivities demix”, *Physical review letters* **116**(5), 058301 (2016).

[97] A. Wysocki, R. G. Winkler, and G. Gompper, “Propagating interfaces in mixtures of active and passive brownian particles”, *New journal of physics* **18**(12), 123030 (2016).

[98] P. Dolai, A. Simha, and S. Mishra, “Phase separation in binary mixtures of active and passive particles”, *Soft Matter* **14**(29), 6137 (2018).

[99] E. Ilker and J.-F. Joanny, “Phase separation and nucleation in mixtures of particles with different temperatures”, *Physical Review Research* **2**(2), 023200 (2020).

[100] F. Hauke, H. Löwen, and B. Liebchen, “Clustering-induced velocity-reversals of active colloids mixed with passive particles”, *The Journal of Chemical Physics* **152**(1) (2020).

[101] A. Y. Grosberg and J.-F. Joanny, “Nonequilibrium statistical mechanics of mixtures of particles in contact with different thermostats”, *Physical Review E* **92**(3), 032118 (2015).

[102] S. Asakura and F. Oosawa, “On interaction between two bodies immersed in a solution of macromolecules”, *The Journal of chemical physics* **22**(7), 1255 (1954).

[103] H. N. Lekkerkerker, W.-K. Poon, P. N. Pusey, A. Stroobants, and P. . Warren, “Phase behaviour of colloid+ polymer mixtures”, *Europhysics Letters* **20**(6), 559 (1992).

[104] S. M. Ilett, A. Orrock, W. Poon, and P. Pusey, “Phase behavior of a model colloid-polymer mixture”, *Physical Review E* **51**(2), 1344 (1995).

[105] S. Griffiths, “Effect of attractive forces on active-passive interactions” (2021).

[106] P. Pusey, W. C. Poon, S. Ilett, and P. Bartlett, “Phase behaviour and structure of colloidal suspensions”, *Journal of Physics: Condensed Matter* **6**(23A), A29 (1994).

[107] H. B. Casimir. On the attraction between two perfectly conducting plates. In *Proc. Kon. Ned. Akad. Wet.*, vol. 51, p. 793 (1948).

[108] A. Gambassi. The casimir effect: From quantum to critical fluctuations. In *Journal of Physics: Conference Series*, vol. 161, p. 012037 (IOP Publishing, 2009).

[109] V. Nguyen, M. T. Dang, T. A. Nguyen, and P. Schall, "Critical casimir forces for colloidal assembly", *Journal of Physics: Condensed Matter* **28**(4), 043001 (2016).

[110] V. D. Nguyen, S. Faber, Z. Hu, G. H. Wegdam, and P. Schall, "Controlling colloidal phase transitions with critical casimir forces", *Nature communications* **4**(1), 1584 (2013).

[111] D. Bonn, J. Otwinowski, S. Sacanna, H. Guo, G. Wegdam, and P. Schall, "Direct observation of colloidal aggregation by critical casimir forces", *Physical review letters* **103**(15), 156101 (2009).

[112] J. Rouwhorst, C. Ness, S. Stoyanov, A. Zaccone, and P. Schall, "Nonequilibrium continuous phase transition in colloidal gelation with short-range attraction", *Nature communications* **11**(1), 3558 (2020).

[113] H.-P. Zhang, A. Beâer, E.-L. Florin, and H. L. Swinney, "Collective motion and density fluctuations in bacterial colonies", *Proceedings of the National Academy of Sciences* **107**(31), 13626 (2010).

[114] L. Ning, X. Lou, Q. Ma, Y. Yang, N. Luo, K. Chen, F. Meng, X. Zhou, M. Yang, and Y. Peng, "Hydrodynamics-induced long-range attraction between plates in bacterial suspensions", *Physical Review Letters* **131**(15), 158301 (2023).

[115] R. L. Schilling and L. Partzsch. *Brownian motion: an introduction to stochastic processes* (Walter de Gruyter GmbH & Co KG, 2014).

[116] Z. Schuss. *Brownian dynamics at boundaries and interfaces* (Springer, 2015).

[117] A. Tiribocchi, R. Wittkowski, D. Marenduzzo, and M. E. Cates, "Active model h: scalar active matter in a momentum-conserving fluid", *Physical review letters* **115**(18), 188302 (2015).

[118] F. Peruani and M. Baer, “A kinetic model and scaling properties of non-equilibrium clustering of self-propelled particles”, *New Journal of Physics* **15**(6), 065009 (2013).

[119] J. P. Singh, S. Pattanayak, S. Mishra, and J. Chakrabarti, “Effective single component description of steady state structures of passive particles in an active bath”, *The Journal of Chemical Physics* **156**(21) (2022).

[120] J. Dzubiella, J. Chakrabarti, and H. Löwen, “Tuning colloidal interactions in subcritical solvents by solvophobicity: Explicit versus implicit modeling”, *The Journal of chemical physics* **131**(4) (2009).

[121] J. Chakrabarti, S. Chakrabarti, and H. Löwen, “Short ranged attraction and long ranged repulsion between two solute particles in a subcritical liquid solvent”, *Journal of Physics: Condensed Matter* **18**(6), L81 (2006).

[122] P.-G. De Gennes. *Simple views on condensed matter*, vol. 8 (World scientific, 1998).

[123] P. Kushwaha, V. Semwal, S. Maity, S. Mishra, and V. Chikkadi. Supplementary information for ”phase separation of passive particles in active liquids”. Available at `https://journals.aps.org/pre/supplemental/10.1103/PhysRevE.108.034603` (2023).

[124] A. S. Vishen, J. Prost, and M. Rao, “Breakdown of effective temperature, power law interactions, and self-propulsion in a momentum-conserving active fluid”, *Physical Review E* **100**(6), 062602 (2019).

[125] R. C. Krafnick and A. E. García, “Impact of hydrodynamics on effective interactions in suspensions of active and passive matter”, *Physical Review E* **91**(2), 022308 (2015).

[126] A. J. Bray, “Theory of phase-ordering kinetics”, *Advances in Physics* **43**(3), 357 (1994).

[127] S. Puri. Kinetics of phase transitions. In *Kinetics of phase transitions*, pp. 13–74 (CRC press, 2009).

[128] J. W. Cahn and J. E. Hilliard, "Free energy of a nonuniform system. i. interfacial free energy", *The Journal of chemical physics* **28**(2), 258 (1958).

[129] J. W. Cahn, "On spinodal decomposition", *Acta metallurgica* **9**(9), 795 (1961).

[130] C. P. Brangwynne, C. R. Eckmann, D. S. Courson, A. Rybarska, C. Hoege, J. Gharakhani, F. Jülicher, and A. A. Hyman, "Germline p granules are liquid droplets that localize by controlled dissolution/condensation", *Science* **324**(5935), 1729 (2009).

[131] C. P. Brangwynne, P. Tompa, and R. V. Pappu, "Polymer physics of intracellular phase transitions", *Nature Physics* **11**(11), 899 (2015).

[132] I. Buttinoni, J. Bialké, F. Kümmel, H. Löwen, C. Bechinger, and T. Speck, "Dynamical clustering and phase separation in suspensions of self-propelled colloidal particles", *Physical review letters* **110**(23), 238301 (2013).

[133] R. Wittkowski, A. Tiribocchi, J. Stenhammar, R. J. Allen, D. Marenduzzo, and M. E. Cates, "Scalar φ 4 field theory for active-particle phase separation", *Nature communications* **5**(1), 4351 (2014).

[134] G. Fausti. *Phase separation in active systems: non-equilibrium fingerprints*. Ph.D. thesis, Université Paris sud (2021).

[135] A. Bray, "Coarsening dynamics of phase-separating systems", *Philosophical Transactions of the Royal Society of London. Series A: Mathematical, Physical and Engineering Sciences* **361**(1805), 781 (2003).

[136] J. Berry, C. P. Brangwynne, and M. Haataja, "Physical principles of intracellular organization via active and passive phase transitions", *Reports on Progress in Physics* **81**(4), 046601 (2018).

[137] S. Pattanayak, S. Mishra, and S. Puri, "Ordering kinetics in the active model b", *Physical Review E* **104**(1), 014606 (2021).

[138] S. Van Gemmert, G. Barkema, and S. Puri, "Phase separation driven by surface diffusion: A monte carlo study", *Physical Review E* **72**(4), 046131 (2005).

[139] D. Das and M. Barma, "Particles sliding on a fluctuating surface: phase separation and power laws", *Physical review letters* **85**(8), 1602 (2000).

[140] D. Das, M. Barma, and S. N. Majumdar, "Fluctuation-dominated phase ordering driven by stochastically evolving surfaces: Depth models and sliding particles", *Physical Review E* **64**(4), 046126 (2001).

[141] A. Das, A. Polley, and M. Rao, "Phase segregation of passive advective particles in an active medium", *Physical Review Letters* **116**(6), 068306 (2016).

[142] M. Shinde, D. Das, and R. Rajesh, "Violation of the porod law in a freely cooling granular gas in one dimension", *Physical review letters* **99**(23), 234505 (2007).

[143] M. Barma, "Fluctuation-dominated phase ordering", *arXiv preprint arXiv:2307.10770* (2023).

[144] S. N. Majumdar, C. Sire, A. J. Bray, and S. J. Cornell, "Nontrivial exponent for simple diffusion", *Physical review letters* **77**(14), 2867 (1996).

[145] Z. Liu, W. Zeng, X. Ma, and X. Cheng, "Density fluctuations and energy spectra of 3d bacterial suspensions", *Soft Matter* **17**(48), 10806 (2021).

[146] S. Dey, D. Das, and R. Rajesh, "Spatial structures and giant number fluctuations in models of active matter", *Physical review letters* **108**(23), 238001 (2012).

[147] J. Zhang, R. Alert, J. Yan, N. S. Wingreen, and S. Granick, "Active phase separation by turning towards regions of higher density", *Nature Physics* **17**(8), 961 (2021).

[148] J. Bouvard, F. Moisy, and H. Auradou, "Ostwald-like ripening in the two-dimensional clustering of passive particles induced by swimming bacteria", *Physical Review E* **107**(4), 044607 (2023).

[149] P. Kushwaha, S. Maity, A. Menon, R. Chelakkot, and V. Chikkadi, "Percolation of nonequilibrium assemblies of colloidal particles in active chiral liquids", *Soft Matter* (2024).

[150] F. Ndlec, T. Surrey, A. C. Maggs, and S. Leibler, "Self-organization of microtubules and motors", *Nature* **389**(6648), 305 (1997).

[151] J. Palacci, C. Cottin-Bizonne, C. Ybert, and L. Bocquet, "Sedimentation and effective temperature of active colloidal suspensions", *Physical Review Letters* **105**(8), 088304 (2010).

[152] A. Bricard, J.-B. Caussin, D. Das, C. Savoie, V. Chikkadi, K. Shitara, O. Chepizhko, F. Peruani, D. Saintillan, and D. Bartolo, "Emergent vortices in populations of colloidal rollers", *Nature communications* **6**(1), 7470 (2015).

[153] H. H. Wensink, J. Dunkel, S. Heidenreich, K. Drescher, R. E. Goldstein, H. Löwen, and J. M. Yeomans, "Meso-scale turbulence in living fluids", *Proceedings of the national academy of sciences* **109**(36), 14308 (2012).

[154] S. Krishnamurthy, S. Ghosh, D. Chatterji, R. Ganapathy, and A. Sood, "A micrometre-sized heat engine operating between bacterial reservoirs", *Nature Physics* **12**(12), 1134 (2016).

[155] T. Sanchez, D. T. Chen, S. J. DeCamp, M. Heymann, and Z. Dogic, "Spontaneous motion in hierarchically assembled active matter", *Nature* **491**(7424), 431 (2012).

[156] G. H. Koenderink, Z. Dogic, F. Nakamura, P. M. Bendix, F. C. MacKintosh, J. H. Hartwig, T. P. Stossel, and D. A. Weitz, "An active biopolymer network controlled by molecular motors", *Proceedings of the National Academy of Sciences* **106**(36), 15192 (2009).

[157] S. Köhler, V. Schaller, and A. R. Bausch, "Structure formation in active networks", *Nature materials* **10**(6), 462 (2011).

[158] J. Alvarado, M. Sheinman, A. Sharma, F. C. MacKintosh, and G. H. Koenderink, “Molecular motors robustly drive active gels to a critically connected state”, *Nature physics* **9**(9), 591 (2013).

[159] D. Grober, I. Palaia, M. C. Uçar, E. Hannezo, A. Šarić, and J. Palacci, “Unconventional colloidal aggregation in chiral bacterial baths”, *Nature Physics* pp. 1–9 (2023).

[160] A. Jepson, V. A. Martinez, J. Schwarz-Linek, A. Morozov, and W. C. Poon, “Enhanced diffusion of nonswimmers in a three-dimensional bath of motile bacteria”, *Physical Review E* **88**(4), 041002 (2013).

[161] G. Mino, T. E. Mallouk, T. Darnige, M. Hoyos, J. Dauchet, J. Dunstan, R. Soto, Y. Wang, A. Rousselet, and E. Clement, “Enhanced diffusion due to active swimmers at a solid surface”, *Physical review letters* **106**(4), 048102 (2011).

[162] A. Morozov and D. Marenduzzo, “Enhanced diffusion of tracer particles in dilute bacterial suspensions”, *Soft Matter* **10**(16), 2748 (2014).

[163] W. R. DiLuzio, L. Turner, M. Mayer, P. Garstecki, D. B. Weibel, H. C. Berg, and G. M. Whitesides, “Escherichia coli swim on the right-hand side”, *Nature* **435**(7046), 1271 (2005).

[164] R. Di Leonardo, L. Angelani, D. DellâArciprete, G. Ruocco, V. Iebba, S. Schippa, M. P. Conte, F. Mecarini, F. De Angelis, and E. Di Fabrizio, “Bacterial ratchet motors”, *Proceedings of the National Academy of Sciences* **107**(21), 9541 (2010).

[165] A. Sokolov, M. M. Apodaca, B. A. Grzybowski, and I. S. Aranson, “Swimming bacteria power microscopic gears”, *Proceedings of the National Academy of Sciences* **107**(3), 969 (2010).

[166] W. C. Poon, “The physics of a model colloid–polymer mixture”, *Journal of Physics: Condensed Matter* **14**(33), R859 (2002).

[167] E. Zaccarelli, “Colloidal gels: Equilibrium and non-equilibrium routes”, *Journal of Physics: Condensed Matter* **19**(32), 323101 (2007).

[168] H. Tsurusawa, M. Leocmach, J. Russo, and H. Tanaka, “Direct link between mechanical stability in gels and percolation of isostatic particles”, *Science advances* **5**(5), eaav6090 (2019).

[169] M. Kohl, R. Capellmann, M. Laurati, S. Egelhaaf, and M. Schmiedeberg, “Directed percolation identified as equilibrium pre-transition towards non-equilibrium arrested gel states”, *Nature Communications* **7**(1), 11817 (2016).

[170] H. Tsurusawa, S. Arai, and H. Tanaka, “A unique route of colloidal phase separation yields stress-free gels”, *Science Advances* **6**(41), eabb8107 (2020).

[171] F. J. Schwarzendahl and M. G. Mazza, “Active percolation in pusher-type microswimmers”, *Europhysics Letters* **140**(4), 47001 (2022).

[172] M. Sanoria, R. Chelakkot, and A. Nandi, “Percolation transition in phase-separating active fluid”, *Physical Review E* **106**(3), 034605 (2022).

[173] D. Levis and L. Berthier, “Clustering and heterogeneous dynamics in a kinetic monte carlo model of self-propelled hard disks”, *Phys. Rev. E* **89**, 062301 (2014). URL `https://link.aps.org/doi/10.1103/PhysRevE.89.062301`.

[174] D. Stauffer and A. Aharony. *Introduction to percolation theory* (CRC press, 2018).

[175] E. T. Gawlinski and H. E. Stanley, “Continuum percolation in two dimensions: Monte carlo tests of scaling and universality for non-interacting discs”, *Journal of Physics A: Mathematical and General* **14**(8), L291 (1981).

[176] S. Safran, I. Webman, and G. S. Grest, “Percolation in interacting colloids”, *Physical Review A* **32**(1), 506 (1985).

[177] A. A. Saberi, “Recent advances in percolation theory and its applications”, *Physics Reports* **578**, 1 (2015).

[178] A. Bunde and W. Dieterich, “Percolation in composites”, *Journal of electroceramics* **5**, 81 (2000).

[179] S. Mertens and C. Moore, “Continuum percolation thresholds in two dimensions”, *Physical Review E* **86**(6), 061109 (2012).

[180] K. Christensen, “Percolation theory”, *Imperial College London* **1** (2002).

[181] H. C. Berg and L. Turner, “Chemotaxis of bacteria in glass capillary arrays. escherichia coli, motility, microchannel plate, and light scattering”, *Biophysical Journal* **58**(4), 919 (1990).

[182] P. D. Frymier, R. M. Ford, H. C. Berg, and P. T. Cummings, “Three-dimensional tracking of motile bacteria near a solid planar surface.”, *Proceedings of the National Academy of Sciences* **92**(13), 6195 (1995).

[183] D. Lopez and E. Lauga, “Dynamics of swimming bacteria at complex interfaces”, *Physics of Fluids* **26**(7) (2014).

[184] R. M. Ziff, “Spanning probability in 2d percolation”, *Physical review letters* **69**(18), 2670 (1992).

[185] S. B. Lee and S. Torquato, “Monte carlo study of correlated continuum percolation: Universality and percolation thresholds”, *Physical Review A* **41**(10), 5338 (1990).

[186] A. Ghosh, Z. Budrikis, V. Chikkadi, A. L. Sellerio, S. Zapperi, and P. Schall, “Direct observation of percolation in the yielding transition of colloidal glasses”, *Physical review letters* **118**(14), 148001 (2017).

[187] S. N. Majumdar, S. Krishnamurthy, and M. Barma, "Nonequilibrium phase transitions in models of aggregation, adsorption, and dissociation", *Physical review letters* **81**(17), 3691 (1998).

[188] B. Lorenz, I. Orgzall, and H.-O. Heuer, "Universality and cluster structures in continuum models of percolation with two different radius distributions", *Journal of Physics A: Mathematical and General* **26**(18), 4711 (1993).

[189] H. Tanaka, "Viscoelastic phase separation in biological cells", *Communications Physics* **5**(1), 167 (2022).

[190] R. Hunter. *Foundations of Colloid Science* (Oxford University Press, 2001). URL `https://books.google.co.in/books?id=-UVCAQAAIAAJ`.

[191] S. Kamdar, S. Shin, P. Leishangthem, L. F. Francis, X. Xu, and X. Cheng, "The colloidal nature of complex fluids enhances bacterial motility", *Nature* **603**(7903), 819 (2022).

[192] B. Wang, S. M. Anthony, S. C. Bae, and S. Granick, "Anomalous yet brownian", *Proceedings of the National Academy of Sciences* **106**(36), 15160 (2009).

[193] B. Wang, J. Kuo, S. C. Bae, and S. Granick, "When brownian diffusion is not gaussian", *Nature materials* **11**(6), 481 (2012).

[194] J. Ślezak, R. Metzler, and M. Magdziarz, "Superstatistical generalised langevin equation: non-gaussian viscoelastic anomalous diffusion", *New Journal of Physics* **20**(2), 023026 (2018).

[195] R. Metzler, "Superstatistics and non-gaussian diffusion", *The European Physical Journal Special Topics* **229**(5), 711 (2020).

[196] E. Lemaitre, I. M. Sokolov, R. Metzler, and A. V. Chechkin, "Non-gaussian displacement distributions in models of heterogeneous active particle dynamics", *New Journal of Physics* **25**(1), 013010 (2023).

[197] F. Ginot, I. Theurkauff, F. Detcheverry, C. Ybert, and C. Cottin-Bizonne, “Aggregation-fragmentation and individual dynamics of active clusters”, *Nature communications* **9**(1), 696 (2018).

[198] J. Blackman and A. Marshall, “Coagulation and fragmentation in cluster-monomer reaction models”, *Journal of Physics A: Mathematical and General* **27**(3), 725 (1994).

[199] F. Ginot. *Dynamical aspects of active colloids: from dilute to dense systems*. Ph.D. thesis, Université de Lyon (2016).